

# Investigation of the Dynamic Response of a FOWT to Periodic Surge Motion

Vadim Uritsky





# Investigation of the Dynamic Response of a FOWT to Periodic Surge Motion

by

Vadim Uritsky

Student number: 5012422

to obtain the degree of Master of Science  
at the Delft University of Technology,  
to be defended publicly on Friday November 26, 2021 at 9:00 AM.

Student number:	5012422
Project duration:	February 1, 2021 – November 26, 2021
Thesis committee:	Prof. Dr. ir. C. J. Simao Ferreira, TU Delft, supervisor
	Dr. ir. H. Ozdemir, TNO, supervisor
	Dr. ir. A.H. van Zuijlen, TU Delft
	Dr. ir. T. Sinnige, TU Delft

An electronic version of this thesis is available at <http://repository.tudelft.nl/>.



# Abstract

Due to the increasing interest in modelling floating offshore wind turbines, simulation tools need to be adapted from fixed-base applications to surge applications. In this study, an open-source inviscid 3D panel method named Vortexje was adapted for surge motion and its ability to capture the physics of severe surge motion (when the rotor velocity approaches or exceeds the incoming wind velocity) was investigated. A simple test case first found instabilities with direct surface translation, likely a result of attached wake panel placement, justifying the use of equivalent dynamic inflow conditions for subsequent simulations.

It was then found that despite validation for a fixed-base rotor, inaccuracies and numerical instabilities remain when integrating the panel method pressure values directly. Estimating the thrust through the bound circulation provided a more accurate solution, comparable to existing viscous CFD results. It was found that the rotor could, in severe surge cases, briefly operate in propeller mode. Inflow angles were also estimated using existing CFD-related techniques, which provided reasonable results for fixed-base applications but inconsistencies with moderate and severe surge. It was found that the variations in induction factor did not approach those required to induce vortex ring state.



# Acknowledgements

My journey at TU Delft has been an incredible experience for me, full of incredible educational values and wonderful people. They have all pushed me to strive for excellence, and for that I am grateful.

I would especially like to thank Dr. Carlos Ferreira for his guidance through this study, even under pandemic circumstances. He has given me a lot of support, both technical and as mentor, and I would not have gotten to this point without him.

I would also like to express my gratitude to Dr. Huseyin Ozdemir at TNO for being an excellent supervisor throughout both my internship and thesis, and for giving me the consistent feedback and support I needed to complete this program.

Finally, I would not have succeeded in this program without the support of my family and friends, and their incredible moral and financial support.



# Contents

<b>Abstract</b>	<b>iii</b>
<b>Acknowledgements</b>	<b>v</b>
<b>List of Figures</b>	<b>ix</b>
<b>List of Tables</b>	<b>xi</b>
<b>Nomenclature</b>	<b>xiii</b>
<b>1 Introduction and Literature Review</b>	<b>1</b>
1.1 Introduction . . . . .	1
1.2 Modelling FOWT Systems . . . . .	1
1.2.1 Characterization of unsteady FOWT aerodynamics . . . . .	1
1.2.2 BEM Models . . . . .	6
1.2.3 Computational Fluid Dynamics Models . . . . .	17
1.2.4 Free Vortex Methods . . . . .	22
1.3 Research Question, Aim/Objectives and Sub-Goals . . . . .	32
1.3.1 Research Question . . . . .	32
<b>2 Simulation Setup &amp; Methodology</b>	<b>33</b>
2.1 Simulation Set-up. . . . .	33
2.2 Methodology . . . . .	33
2.3 Loading Calculation . . . . .	34
2.4 Velocity Field Calculation. . . . .	35
2.5 Implementation of Surge Motion. . . . .	37
2.6 Investigation of Research Questions . . . . .	38
<b>3 Results</b>	<b>39</b>
3.1 Steady Validation: MEXICO Test Campaign . . . . .	39
3.1.1 Pressure Profiles . . . . .	39
3.1.2 High Tip Speed Ratio. . . . .	39
3.1.3 Design Tip Speed Ratio . . . . .	41
3.1.4 Low Tip Speed Ratio . . . . .	42
3.2 Test Case: Lifting Surface Oscillation . . . . .	43
3.3 Test Case: UNAFLOW . . . . .	46
3.3.1 Experimental Results. . . . .	46
3.4 Analysis: Severe Surge with the NREL 5MW Reference Turbine . . . . .	50
3.4.1 Surge through Dynamic Inflow. . . . .	50
<b>4 Conclusions and Recommendations</b>	<b>63</b>
4.1 Conclusions. . . . .	63
4.2 Recommendations . . . . .	65
<b>A Appendix</b>	<b>67</b>
A.1 MEXICO Test Campaign . . . . .	67
A.1.1 Background to the MEXICO Test Campaign . . . . .	67
A.1.2 MEXICO Rotor and Experiment Details . . . . .	67
A.2 UNAFLOW Campaign . . . . .	68
A.2.1 Background to the UNAFLOW test campaign. . . . .	68
A.2.2 UNAFLOW Rotor and Experiment Details . . . . .	68
A.2.3 Numerical Models used in Simulating UNAFLOW Experiments . . . . .	69
A.3 NREL 5MW Rotor . . . . .	69

**Bibliography**

**71**

# List of Figures

1.1	Sources of unsteady aerodynamic phenomena present on a wind turbine blade. Taken from [26]. . . . .	1
1.2	Degrees of freedom of motion attributable to the floating platform. Taken from [45]. . . . .	2
1.3	Illustration of Barge, TLP, and Spar FOWT Platform Types. Taken from [19]. . . . .	3
1.4	(a) Angles of attack experienced by blades in propeller state, and (b) lift-drag polars of airfoils used in NREL 5MW reference turbine. Taken from [24]. . . . .	5
1.5	Diagrams illustrating the actuator disc concept. Taken from [5]. . . . .	6
1.6	Diagrams of an element of a rotor blade, with (a) the velocities it experiences and (b) the loads that act upon it. Taken from [5]. . . . .	7
1.7	Diagrams illustrating rotor wake modelled (a) by Prandtl as discs, and (b) as a helix. Taken from [5]. . . . .	9
1.8	Prandtl correction factor $F_{Bu}$ given in Equation 1.36 given $B = 3$ , $\lambda = 6$ , and $r_{root}/R = 0.2$ . Taken from [5]. . . . .	11
1.9	Relative Difference in AEP between selected tip-loss functions existing in literature. Taken from [4]. . . . .	11
1.10	Comparison of tip loss factor suggested by Branlard et al. to that suggested by Glauert, as well as the lifting-line method. Adapted from [4]. . . . .	12
1.11	Wind turbine thrust coefficient ( $C_T$ ) against induction factor $a$ . Taken from [47]. . . . .	12
1.12	The lift/drag/moment hysteresis effects of dynamic stall on an oscillating 2D airfoil (left), along with a schematic of the associated flow morphology. Taken from [26]. . . . .	14
1.13	Relative position of the rotor used by Tran et al. for $A_s = 8m$ , $\omega_s = 0.5rad/s$ . Taken from [52]. . . . .	17
1.14	Vorticity contours due to platform surge motion for $A_s = 16m$ , $\omega_s = 0.5rad/s$ . Taken from [52]. . . . .	18
1.15	Pressure coefficients at selected span-wise locations for $A_s = 4, 8, 16m$ , $\omega_s = 0.5rad/s$ , at selected points in the surge cycle. Taken from [52]. . . . .	19
1.16	Thrust coefficient acting on the total rotor and individual blades for (a) the BF case and (b) the BS case. Taken from [24]. . . . .	20
1.17	Vorticity iso-volumes for the BS case for (a) $t = 11.5s$ , (b) $t = 12.0s$ , (c) $t = 12.5s$ , and (d) $t = 13.0s$ . Taken from [24]. . . . .	21
1.18	Sketch of the streamlines of (a) source and (b) doublet distributions. Taken from [21]. . . . .	23
1.19	Panel discretization of a 3D wing with a source-doublet distribution. Taken from [10]. . . . .	24
1.20	Mean power coefficient against (a) tip-speed ratio and (b) reduced frequency. Taken from [57]. . . . .	28
1.21	Mean thrust coefficient against (a) tip-speed ratio and (b) reduced frequency. Taken from [57]. . . . .	28
1.22	Rotor power, thrust and platform moment over time given surge displacement profile of NREL 5MW rotor [46] . . . . .	29
1.23	Rotor position throughout pitching motion. Taken from [17]. . . . .	30
1.24	Normal vorticity fields and streamlines at location 7. Taken from [17]. Note that the orientation of the rotor is the same as the reference sketch in Figure 1.23 . . . . .	30
2.1	Sampling schematics of the (a) AAT and (b) 3-Point methods, which are used to estimate the angle of attack and induction factor at the rotor. Taken from [37]. . . . .	37
3.1	Experimentally and numerically obtained pressure coefficients of the MEXICO rotor in a free-stream velocity of $10.0m/s$ and tip speed ratio $\lambda = 10.0$ . Taken from [55]. . . . .	40
3.2	Experimentally and numerically obtained pressure coefficients of the MEXICO rotor in a free-stream velocity of $14.7m/s$ and tip speed ratio $\lambda = 6.7$ . Taken from [55]. . . . .	41

3.3	Experimentally and numerically obtained pressure coefficients of the MEXICO rotor in a free-stream velocity of $24.1\text{m/s}$ and tip speed ratio $\lambda = 4.2$ . Taken from [55]. . . . .	42
3.4	Wake characteristics of a lifting surface with horizontal surge motion imposed through (a) direct displacement and (b) dynamic inflow conditions . . . . .	43
3.5	Wake disturbance generation at the maximum upstream position of a lifting surface with horizontal surge motion imposed . . . . .	44
3.6	Wake characteristics of a lifting surface with vertical surge motion imposed through (a) direct displacement and (b) dynamic inflow conditions . . . . .	45
3.7	Numerical (a) axial and (b) tangential force distributions of the steady UNAFLOW experiment, as calculated by Aero-Module (BEM & AWSM), FLOWer, and Vortexje . . . . .	46
3.8	Reduced amplitude $\frac{A_s}{D}$ against reduced frequency $k$ . . . . .	47
3.9	Thrust coefficient amplitude $\Delta C_T$ against reduced maximum surge velocity $v_{max}$ . . . . .	48
3.10	Review of thrust coefficient amplitude $\Delta C_T$ (from literature) against reduced maximum surge velocity $v_{max}$ . Taken from [13]. . . . .	49
3.11	Thrust coefficient amplitude $\Delta C_T$ against mean thrust coefficient $k$ . . . . .	49
3.12	Surge displacement and velocity conditions for moderate and severe surge, according to Kyle et al. [24]. . . . .	50
3.13	Axial loading distribution for (a) moderate and (b) severe surge conditions . . . . .	51
3.14	Thrust coefficient for (a) moderate and (b) severe surge conditions . . . . .	51
3.15	Tangential loading distribution for (a) moderate and (b) severe surge conditions . . . . .	52
3.16	Power coefficient for (a) moderate and (b) severe surge conditions . . . . .	53
3.17	Pressure coefficient at $r/R = 0.3$ for (a) moderate and (b) severe surge conditions . . . . .	54
3.18	Pressure coefficient at $r/R = 0.5$ for (a) moderate and (b) severe surge conditions . . . . .	54
3.19	Pressure coefficient at $r/R = 0.9$ for (a) moderate and (b) severe surge conditions . . . . .	55
3.20	Circulation distribution for (a) moderate and (b) severe surge conditions . . . . .	56
3.21	Circulation distribution for (a) moderate and (b) severe surge conditions, at $r/R = 0.8$ . . . . .	57
3.22	Lift distribution for (a) moderate and (b) severe surge conditions . . . . .	58
3.23	Thrust coefficient distribution for (a) moderate and (b) severe surge conditions, assuming $F'_{axial} \approx L' \cos \phi$ . . . . .	58
3.24	Angle of attack distribution for (a) moderate and (b) severe surge conditions . . . . .	59
3.25	Inflow angle distribution for (a) moderate and (b) severe surge conditions . . . . .	60
3.26	Induction factor distribution for (a) moderate and (b) severe surge conditions . . . . .	61
A.1	The MEXICO rotor set up for experimental testing. Taken from [40]. . . . .	68
A.2	The MEXICO blade showing locations at which sectional pressure measurements were taken. . . . .	68

# List of Tables

1	Abbreviations . . . . .	xiii
2	Symbols . . . . .	xiv
1.1	Typical unsteadiness values experienced by a HAWT, given by reduced frequency $k$ . Taken from [33]. . . . .	2
1.2	Dominant platform modes at below-rated, rated, and above-rated conditions. Taken from [45]. . . . .	3
1.3	Unsteady energy in the $\alpha$ PSD, normalized by unsteady energy for the NREL 5MW monopile case, of platform types at below-rated, rated, and above-rated conditions. Taken from [45]. . . . .	3
1.4	CFD studies on FOWT systems in surge . . . . .	17
1.5	Load cases investigated by Kyle et al. [24] . . . . .	20
1.6	Conditions of CFD studies on FOWT surge motion . . . . .	21
1.7	Conditions of FVM studies on FOWT surge motion . . . . .	31
2.1	MEXICO Test Conditions . . . . .	33
2.2	UNAFLOW Cases - Experimental . . . . .	34
2.3	UNAFLOW Cases - Constant Frequency . . . . .	34
2.4	UNAFLOW Cases - Constant Amplitude . . . . .	34
2.5	Load cases investigated by Kyle et al. [24] . . . . .	34
2.6	Geometric and simulation conditions of the surge-implemented lifting surface test cases	38
A.1	Airfoil sections at various span-wise locations on the MEXICO rotor . . . . .	67
A.2	MEXICO Test Conditions . . . . .	68
A.3	NREL 5MW baseline turbine properties . . . . .	69
A.4	NREL 5MW baseline turbine blade aerodynamic properties . . . . .	70



# Nomenclature

## Abbreviations

Average Energy Production	AEP
AAT	Azimuthally Average Technique
AWSM	Aerodynamic Wind turbine Simulation Module
BEM	Blade Element Momentum
BET	Blade Element Theory
CFD	Computational Fluid Dynamics
DOF	Degree of Freedom
FOWT	Floating Offshore Wind Turbine
FVM	Free Vortex Method
HAWT	Horizontal Axis Wind Turbine
LLM	Lifting Line Method
MEXICO	Model Rotor Experiments under Controlled conditions
NREL	National Renewable Energy Laboratory
PSD	Power Spectral Density
RANS	Reynolds-Averaged Navier Stokes
RL	Ramasamy Leishman
SPIV	Stereo Particle Image Velocimetry
TLP	Tension-Leg Platform
UNAFLOW	UNsteady Aerodynamics for Floating Wind
VRS	Vortex Ring State
WInDS	Wake Induced Dynamic Simulator

Table 1: Abbreviations

## Symbols

$a$	Axial induction factor
$a'$	Tangential induction factor
$A_s$	Rotor surge amplitude
$A_D$	Rotor area
$B$	Number of blades
$c$	Blade chord
$C_d$	Sectional drag coefficient
$C_D$	Drag coefficient
$C_l$	Sectional lift coefficient
$C_L$	Lift coefficient
$C_T$	Thrust coefficient
$C_p$	Pressure coefficient
$C_P$	Power coefficient
$D$	Drag force
$F$	Force acting on blade
$k$	Non-dimensional reduced frequency
$L$	Lift force
$L_c$	Characteristic length
$Ma$	Mach number
$p$	Pressure
$p_{ref}$	Reference pressure
$P$	Power
$Q$	Torque
$r$	Span-wise location
$R$	Blade length
$t$	Time
$T$	Thrust
$U$	Characteristic flow velocity
$U_\infty$	Free-stream flow velocity
$U_D$	Rotor flow velocity
$v_{ref}$	Reference velocity
$v_{max}$	Maximum surge velocity
$V_{eff}$	Effective wind speed
$V_s$	Rotor surge velocity
$V_{s,max}$	Maximum rotor surge velocity
$W$	Resultant velocity on airfoil
$X_s$	Rotor surge position
$\alpha$	Angle of attack
$\beta$	Pitch angle
$\Gamma$	Circulation
$\lambda$	Tip speed ratio
$\mu$	Doublet strength
$\phi$	Inflow angle
$\phi_s$	Rotor surge phase
$\Phi$	Velocity potential
$\rho$	Free-stream air density
$\sigma$	Source strength
$\theta$	Twist angle
$\omega$	Characteristic flow frequency
$\omega_s$	Rotor surge frequency
$\Omega$	Turbine rotational speed

Table 2: Symbols

# Introduction and Literature Review

## 1.1. Introduction

To properly transition away from a fossil-fuel based society, the cost of renewable energies such as wind energy needs to be lowered. This has led to a gradual increase of wind turbine size and power rating over recent decades, but it has also led to a search for higher quality wind. Offshore wind has been shown to be of better quality than onshore, and the quality improves the farther offshore one is. However, ballooning costs in the support structure required to anchor the turbine to the seafloor sparked a growing interest in floating offshore wind turbine systems, which are moored to the seabed through cables. These are inherently subject to the motion induced by the wind and waves, meaning they experience additional dynamic changes in loading as they translate according to the motion of the platform. To properly understand the effect of this motion on the rotor's aerodynamic performance, experimental and numerical methods need to be adapted from their fixed-base counterparts, and properly tested. This study intends to investigate the effects of surge (axial) motion on a rotor, and investigate the ability of an open-source inviscid 3D panel method in capturing those effects.

## 1.2. Modelling FOWT Systems

### 1.2.1. Characterization of unsteady FOWT aerodynamics

Accurately predicting the loads acting upon fixed-base Horizontal Axis Wind Turbine (HAWT) systems is a difficult task, as wind turbines are subject to a variety of unsteady phenomena. These sources of unsteadiness can be broadly categorized as steady or unsteady, with Figure 1.1 presenting a schematic of the classification.

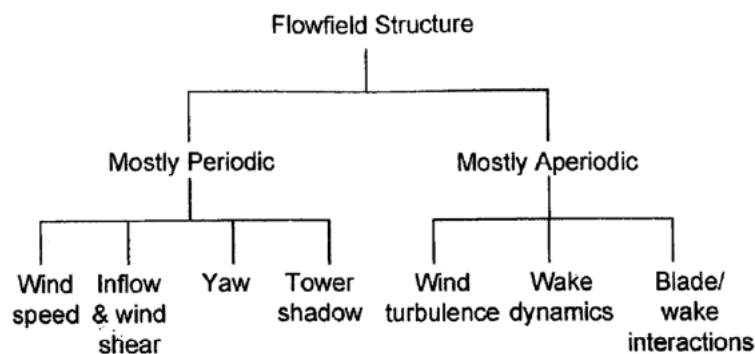


Figure 1.1: Sources of unsteady aerodynamic phenomena present on a wind turbine blade. Taken from [26].

The full effects of these sources are not fully understood [27], although investigations that seek to uncover them first look at the degree of unsteadiness, given by the non-dimensional reduced frequency:

$$k = \frac{\omega L_c}{U} \quad (1.1)$$

where  $\omega$  is the characteristic flow frequency,  $L$  is the chord length, and  $U$  is the characteristic flow velocity. In the case of periodic unsteadiness, these parameters are given as follows:  $\omega$  is the turbine rotational speed  $\Omega$ ,  $L$  is the semi-chord  $c/2$  of the blade element, and  $U$  is the effective wind speed  $V_{eff} = \sqrt{(\Omega r(1 + a'))^2 + ((1 - a)U_\infty)^2}$  at the blade element. Leishman [26] defines unsteady flow as any flow with  $k > 0.05$ , although Pereira et al. [33] note that with wind turbines, flow with  $k > 0.02$  already exhibit unsteady behaviour. Typical 1P wind turbine unsteadiness values are shown in Table 1.1, where it can be seen that wind turbines typically experience a high level of unsteadiness, even towards the end of the blade.

$r/R$	$k(1P)$
0.30	0.120
0.50	0.075
0.75	0.035

Table 1.1: Typical unsteadiness values experienced by a HAWT, given by reduced frequency  $k$ . Taken from [33].

In addition to the above sources of unsteadiness, floating offshore wind turbine (FOWT) systems present additional sources of unsteady loading through the coupling of the rotor motion with that of the platform upon which they rest. The extra six degrees of freedom (DOFs) are shown in Figure 1.2, and each increase the level of unsteadiness and aerodynamic complexity, especially in relation to simulation limitations. Sebastian and Lackner [45] recognized the additional challenges laid by the following FOWT-specific characteristics:

1. Angled flow due to platform-induced yaw, sway, heave, and roll motions
2. An effective shear along the height of the rotor due to pitching motion
3. Harmonically changing blade-vortex interactions rising from the downwind motion of the rotor due to pitch and surge motion, especially when the downwind rotor velocity approaches (or passes) the free-stream wind speed.

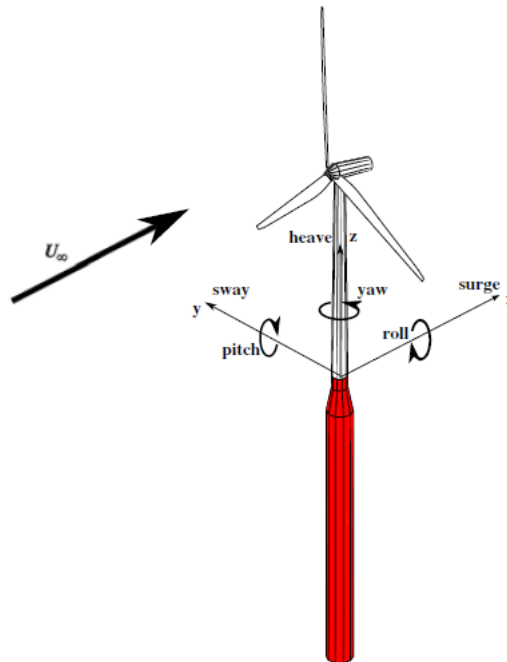


Figure 1.2: Degrees of freedom of motion attributable to the floating platform. Taken from [45].

**Differences in Loading between Platform Types**

A preliminary analysis on the load differences was conducted by Jonkman et al. [19] between three platform types: the barge, the tension-leg platform (TLP), and the spar (illustrated in Figure 1.3). Differences in ultimate and fatigue platform-induced loading were credited to differing dynamic responses at the rotor, with the barge-type platform having the highest loads.

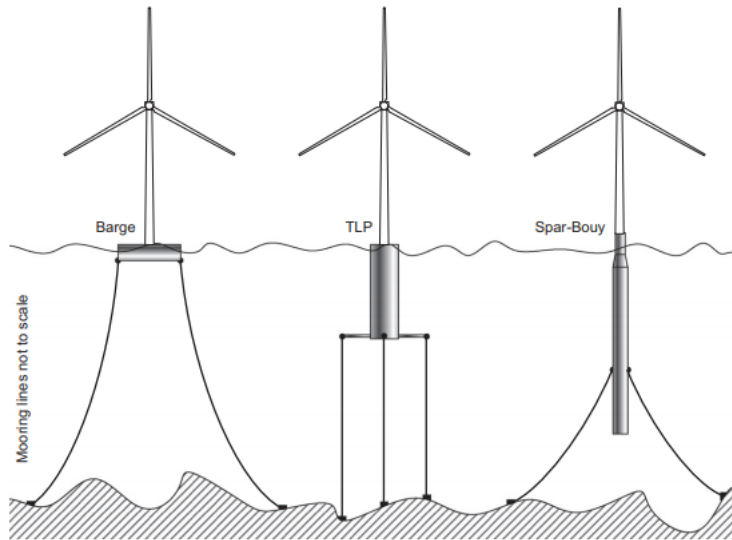


Figure 1.3: Illustration of Barge, TLP, and Spar FOWT Platform Types. Taken from [19].

In an attempt to identify the potential of these platform types, Sebastian and Lackner [45] expanded this study and characterized the unsteady aerodynamics of a FOWT system with each of the three platform types. Power spectral density (PSD) plots of the angle of attack  $\alpha$  of the blade along the span were generated to determine which types of motion are most significant. After analyzing the frequency response against the unsteadiness criterion of  $k > 0.05$  in below-rated ( $\lambda = 9.63$ ), rated ( $\lambda = 7.00$ ), and above-rated ( $\lambda = 4.43$ ) conditions, the aerodynamically dominant DOFs were identified for each of the platform types. These are given in Table 1.2. Pitch, surge, and yaw motions are seen to be the aerodynamically dominant platform motion modes, and are thus considered to be important for FOWT systems. The overall unsteady energy in the  $\alpha$  PSD, normalized by the unsteady energy for the NREL 5MW monopile case, is also given in Table 1.3, to further understand the extent to which these modes induce unsteady aerodynamic effects.

Conditions	Barge	Spar	TLP
Below-rated	Pitch	Pitch/Yaw	Pitch/Surge
Rated	Pitch	Pitch/Surge/Yaw	Surge
Above-Rated	Pitch	Yaw	Surge

Table 1.2: Dominant platform modes at below-rated, rated, and above-rated conditions. Taken from [45].

Conditions	Barge	Spar	TLP
Below-rated	14.1	2.1	1.1
Rated	4.1	3.7	1.1
Above-Rated	3.2	6.3	1.0

Table 1.3: Unsteady energy in the  $\alpha$  PSD, normalized by unsteady energy for the NREL 5MW monopile case, of platform types at below-rated, rated, and above-rated conditions. Taken from [45].

Table 1.2 makes it clear that pitch, surge, and yaw motions are the most prevalent platform motions for FOWT systems, highlighting the need to investigate these further. While yawed flow has been studied in depth for stationary wind turbines (as a result of misaligned wind), unsteady acceleration in

the yawed direction is still a relatively unexplored field, but will not be investigated further in this study. Pitch and surge motions are related in that the motion is broadly (for small-amplitude pitch) parallel to the incoming wind velocity. They differ in the vertical shear-like effect induced by the top of the rotor moving faster than the bottom in pitch motion; in surge motion there is no such vertical effect. Surge motion is thus a simpler platform motion to which the dynamic response of a wind turbine can be studied, and is thus more commonly explored.

### Characterizing Surge Parameters

Surge motion can be explained as the motion of the rotor, induced by the motion of the floating platform, parallel to the wind direction. The majority of literature describes surge motion harmonically, by prescribing the position  $X_s$  of the rotor to a sinusoidal function

$$X_s = A_s \sin(\omega_s t + \phi_s) \quad (1.2)$$

where  $A_s$ ,  $\omega_s$ , and  $\phi_s$  are the amplitude, frequency, and phase of the oscillating rotor. The surge velocity of the rotor in the inertial reference frame  $V_s$  is thus

$$V_s = \frac{dX_s}{dt} = A_s \omega_s \cos(\omega_s t + \phi_s) \quad (1.3)$$

with the maximum surge velocity  $V_{s,max}$  simply calculated to be

$$V_{s,max} = A_s \omega_s \quad (1.4)$$

To easily compare results from literature, a reduced maximum velocity  $v_{max}$  can be defined as

$$v_{max} = \frac{V_{s,max}}{U_\infty} = \frac{A_s \omega_s}{U_\infty} \quad (1.5)$$

Similarly, a reduced frequency  $k$  can be defined through the surge amplitude and frequency as

$$k = \frac{\omega_s (2R)}{U_\infty} \quad (1.6)$$

where  $R$  is the radius of the rotor. A reduced maximum velocity  $v_{max}$  close to 1 implies the possibility of flow reversal at the rotor - a simple conclusion given that rotor moves at the same speed as the wind speed. This condition could arise from a high amplitude or frequency platform surge, or a sudden drop in wind speeds, and will be referred to hereafter as 'severe' surge motion. In contrast, 'mild' surge will be used to describe operating states of  $v_{max}$  significantly lower than 1. It is important to note that the definition of reduced maximum velocity  $v_{max}$  is based on the incoming flow velocity upstream, and that the velocity experienced at the rotor will be lower - meaning that these conditions are potentially applicable at values of  $v_{max}$  close to but not yet 1.

In several works, the possibility of vortex ring state (VRS), an operational state characterized by heavy loading and prominent root/tip vortices, was identified as the subsequent flow re-circulation around the edge of the rotor. Propeller state was also identified as an overall negative thrust cause by sufficiently low incidence angles at the blade. Kyle et al. [24] explain this phenomena through the use of Figure 1.4. The black line in Figure 1.4a shows the negative of the local blade twist, and the yellow line shows the angles of attack at which the polar of the given airfoil produces zero lift. The latter of these are the result of interpolating the lift-drag polars in Figure 1.4b. At the moment the effective wind speed (the wind speed experienced from the point of view of the rotor) becomes zero, the only velocity experienced by the rotor is angular, meaning that the angle of attack reduces to the negative of the pitch. This condition is thus depicted by the black line in Figure 1.4a, and shown through comparison with the yellow line to result in negative lift for inboard airfoils. For increasingly negative experienced wind speeds, this effect increases, with the aggregate effect of an overall negative lift, which characterizes propeller state. The cycling between propeller state and regular rotor operation has the potential to pose large problems in relation to fatigue loading, and is thus an important condition to investigate further.

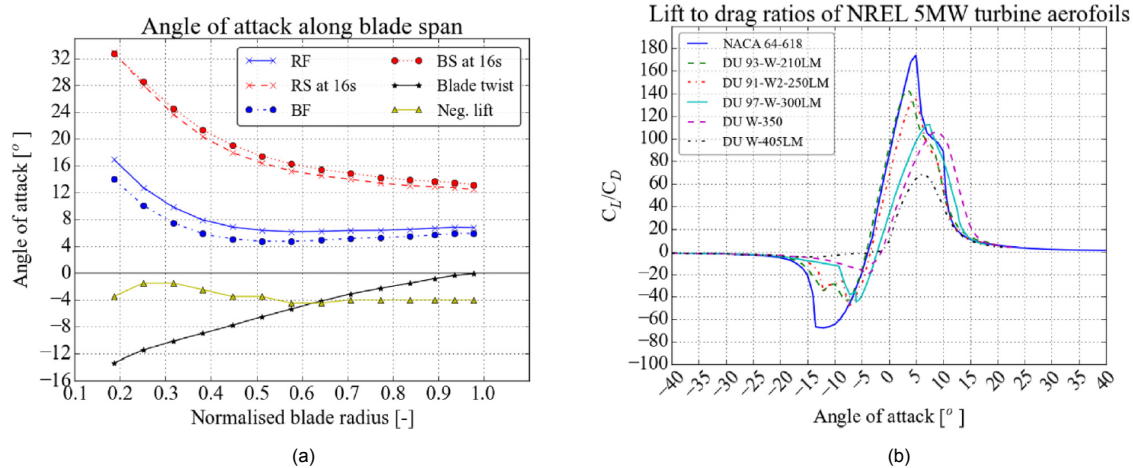


Figure 1.4: (a) Angles of attack experienced by blades in propeller state, and (b) lift-drag polars of airfoils used in NREL 5MW reference turbine. Taken from [24].

### NREL 5MW reference turbine

The techniques used for modelling FOWT systems are adapted from those used to model fixed-base wind turbines, which vary in fidelity. In order of increasing fidelity (and computational cost), the three most common modelling techniques are Blade Element Momentum (BEM) techniques, Free Vortex Method (FVM) techniques, and Computation Fluid Dynamics (CFD) techniques. There do also exist generalized dynamic wake models used commonly in helicopter design, although these are limited to the highly loaded operating conditions that helicopters are subject to. In the next section, an in-depth discussion on the theoretical background, applicability, and use in literature of these models on FOWT systems will be explored.

## 1.2.2. BEM Models

### Theoretical Background

Actuator disc theory assumes the existence of a permeable circular disc that exerts a force upon the flow that passes through it, accelerating or decelerating it. This force field is shown in Figure 1.5a as the simplification of the finite-bladed rotor. This force field is shown to act against the direction of the wind, decelerating the flow and increasing the size of the stream-tube by the principle of mass conservation. This change in velocity is shown in Figure 1.5b as a gradual decrease beginning significantly upstream from the rotor disc. This decrease in velocity is complemented by an increase of pressure as per the principle of energy conservation, until it reaches the rotor. At that point, the rotor acts on the flow and the static pressure drops across the interface of the actuator disc. The continued decrease in velocity is once again absorbed by the increase of static pressure, up until the static pressure reaches the equilibrium value.

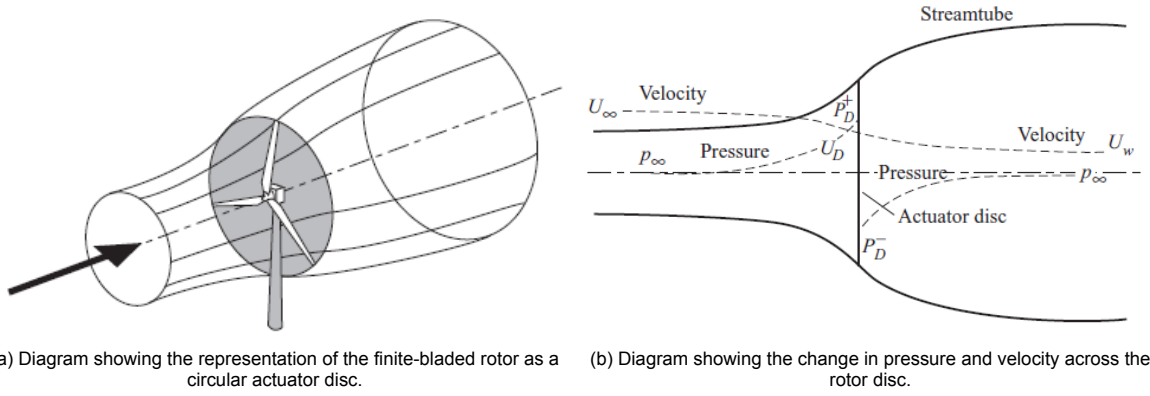


Figure 1.5: Diagrams illustrating the actuator disc concept. Taken from [5].

This model assumes a boundary between the air that is affected by the rotor, shown as the stream-tube in Figure 1.5a, and the air outside the stream-tube. Within this stream-tube, the principle of mass conservation applies (as no air crosses the boundary), and thus the following equality holds:

$$\rho A_{\infty} U_{\infty} = \rho A_D U_D = \rho A_W U_W \quad (1.7)$$

Where the subscripts  $\infty$ ,  $D$ , and  $W$  refer to conditions far upstream, at the rotor disc, and far downstream. The axial velocity at the disc is given in actuator disc theory by the axial induction factor  $a$ :

$$U_D = U_{\infty}(1 - a) \quad (1.8)$$

The rate of change of momentum from the upstream position to the downstream can be given by the pressure differential across the disc (as no external force acts on the boundary of the stream-tube, and the flow is assumed to be inviscid), as well as the change in velocity multiplied by the mass flow rate:

$$(p_D^+ - p_D^-)A_D = (U_{\infty} - U_W)\rho A_D U_{\infty}(1 - a) \quad (1.9)$$

Where the pressure differential across the disc ( $p_D^+ - p_D^-$ ) can be determined through applying Bernoulli's equation for the flow upstream and downstream from the disc, individually. The assumptions of incompressible flow ( $\rho_{\infty} = \rho_D = \rho_W = \rho$ ) and horizontal flow ( $h_{\infty} = h_D = h_W = h$ ) are applied at this stage.

$$\text{Upstream: } \frac{1}{2}\rho U_{\infty}^2 + p_{\infty} + \rho gh = \frac{1}{2}\rho U_D^2 + p_D^+ + \rho gh \quad (1.10)$$

$$\frac{1}{2}\rho U_{\infty}^2 + p_{\infty} = \frac{1}{2}\rho U_D^2 + p_D^+ \quad (1.11)$$

$$\text{Downstream: } \frac{1}{2}\rho U_W^2 + p_W = \frac{1}{2}\rho U_D^2 + p_D^- \quad (1.12)$$

$$\text{Pressure Differential: } (p_D^+ - p_D^-) = \frac{1}{2}\rho(U_{\infty}^2 - U_W^2) \quad (1.13)$$

The momentum rate of change equations can be re-written as

$$\frac{1}{2}\rho(U_\infty^2 - U_W^2)A_D = (U_\infty - U_W)\rho A_D U_\infty(1 - a) \quad (1.14)$$

$$\rightarrow U_W = (1 - 2a)U_\infty \quad (1.15)$$

From which the conclusion follows that loss in velocity upstream of the disc is equal to that of the loss downstream of the rotor. The thrust on the rotor  $T$  is given by the momentum balance equation:

$$T = (p_D^+ - p_D^-)A_D = (U_\infty - U_W)\rho A_D U_\infty(1 - a) = 2\rho A_D U_\infty^2 a(1 - a) \quad (1.16)$$

And the corresponding thrust coefficient is given as:

$$C_T = \frac{T}{\frac{1}{2}\rho U_\infty^2 A_D} = \frac{2\rho A_D U_\infty^2 a(1 - a)}{\frac{1}{2}\rho U_\infty^2 A_D} = 4a(1 - a) \quad (1.17)$$

The power done by the rotor, which is the force at the rotor multiplied by the disc velocity, and the corresponding power coefficient, can be given as

$$P = T U_D = 2\rho A_D U_\infty^3 a(1 - a)^2 \quad (1.18)$$

$$C_P = \frac{P}{\frac{1}{2}\rho U_\infty^3 A_D} = 4a(1 - a)^2 \quad (1.19)$$

In addition to exerting a force upon the rotor, wind turbines are subject to torque from the flow which must be balanced by an equal and opposite torque on the flow. This torque can be expressed, similarly as to the thrust, as a change in angular momentum. This change in angular momentum induces a tangential (to the rotor disc) velocity of the flow, which is expressed through the tangential induction factor  $a'$ . This tangential velocity varies across the span of the rotor, with the overall torque depending on the distribution of torque at individual annular rings:

$$\delta Q = \rho \delta A_D U_\infty(1 - a)2\Omega a' r^2 = \rho U_\infty(1 - a)2\pi r 2a' r^2 \Omega \delta r \quad (1.20)$$

Where  $\delta Q$  and  $\delta A_D$  are the annular torque and annular area of the ring at the radial location  $r$ . The corresponding angular thrust  $\delta T$  at an angular ring can similarly be given as

$$\delta T = 2\pi r \delta r \rho U_\infty(1 - a)2a U_\infty \quad (1.21)$$

Blade Element Theory (BET) attempts to define the thrust and torque forces acting on an element of a blade that sweeps out an annular ring. This element, along with (a) the velocities and (b) the forces, are shown in Figure 1.6. Figure 1.6a shows how the inflow angle  $\phi$  can be determined from the magnitudes of the axial and tangential velocity vectors:

$$\tan \phi = \frac{U_\infty(1 - a)}{r\Omega(1 + a')} \quad (1.22)$$

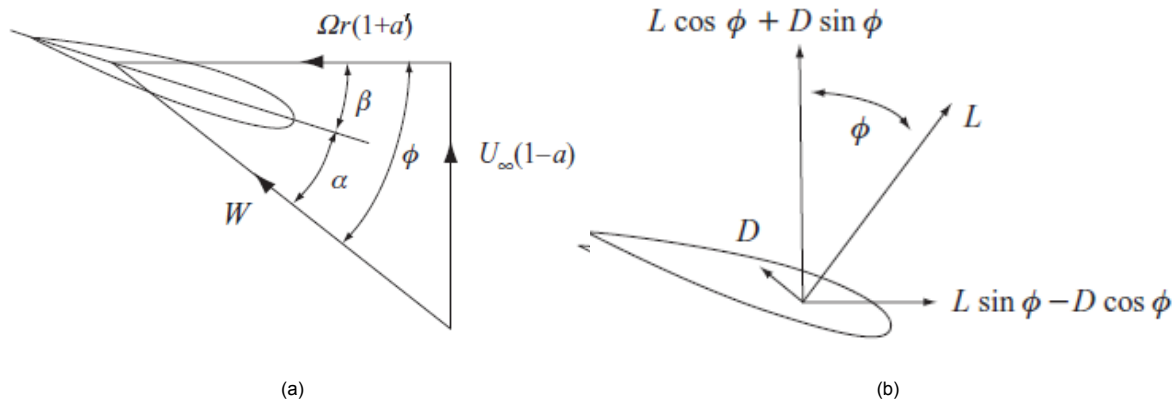


Figure 1.6: Diagrams of an element of a rotor blade, with (a) the velocities it experiences and (b) the loads that act upon it. Taken from [5].

The angle of attack experienced by the blade can then be deduced as the subtraction of the blade pitch angle  $\beta$  (a structural property of the rotor) from the inflow angle:

$$\alpha = \phi - \beta \quad (1.23)$$

The lift and drag forces are then calculated through the use of lift and drag coefficients, which in turn are extracted from experimentally available data relating to the airfoil in question:

$$\delta L = \frac{1}{2} \rho W^2 c C_l \delta r \quad (1.24)$$

$$\delta D = \frac{1}{2} \rho W^2 c C_d \delta r \quad (1.25)$$

Where  $W = \sqrt{(U_\infty(1-a))^2 + (r\Omega(1+a'))^2}$  is the resultant velocity acting on the airfoil. The projection of these forces into axial and tangential directions then provide a basis for the calculation of thrust, torque, and power:

$$\delta T = \delta L \cos \phi + \delta D \sin \phi = \frac{1}{2} \rho W^2 B c (C_l \cos \phi + C_d \sin \phi) \delta r \quad (1.26)$$

$$\delta Q = (\delta L \sin \phi - \delta D \cos \phi) r = \frac{1}{2} \rho W^2 B c r (C_l \sin \phi - C_d \cos \phi) \delta r \quad (1.27)$$

$$\delta P = \delta Q \Omega \quad (1.28)$$

To summarize, actuator disc theory and BET are both capable of relating the axial and tangential velocities at an annular ring (expressed through  $a$  and  $a'$ ) to the axial and tangential loading acting upon that ring (expressed through  $\delta T$  and  $\delta Q$ ). Blade Element Momentum (BEM) theory thus provides a framework to solve for these parameters, by equating the actuator-disc-theory-derived induction factors with the BET-derived induction factors, and likewise with the loads. An iterative procedure is thus followed; in the following example from Burton et al. [5], the right hand sides of the equations are evaluated to yield the next iteration of induction factors, which are in turn used as per BET to calculate the next iteration of loads values.

$$\frac{a}{1-a} = \frac{\sigma_r}{4 \sin^2 \phi} (C_l \cos \phi + C_d \sin \phi) \quad (1.29)$$

$$\frac{a'}{1+a'} = \frac{\sigma_r}{4 \sin \phi \cos \phi} (C_l \sin \phi - C_d \cos \phi) \quad (1.30)$$

Where  $\sigma_r$  is the chord solidity, defined as the total blade chord length at location  $r$  divided by the circumferential length at that radius.

BEM theory holds the following assumptions, which, depending on their validity, must be corrected for:

- **Incompressible flow** is not necessary to correct, as compressibility effects are insignificant for flows with  $Ma < 0.3$ . In typical wind turbine operation, this is satisfied.
- **Inviscid flow** is accounted for when the loading is calculated from lift-drag polars in BET.
- The assumption of **independent annular rings** implies a lack of radial momentum transfer; assuming instead the flow is purely axial and azimuthal. In reality, wind turbines have high radial effects, especially at the tips [31]. Yawed flow also plays a large role in challenging this assumption, as skewed wake features heavy inter-stream-tube interactions [31]. FOWT systems that encounter heavy blade-vortex interactions from negative effective wind speeds also have modelling difficulties with BEM, as the re-circulation at the root and tips is a radial effect.
- The **axial induction factors** used in actuator disc theory and in BET are **equal**. In reality, at a given radial location, the momentum loss at the blade is higher than between the blades and a finite-blade correction factor is necessary to account for that.
- The flow does not **reverse** at any point in the stream-tube. This means that for  $a \geq 0.5$ , the BEM model breaks down as the far wake wind velocity would otherwise be predicted to become negative. In reality, rotors operating in the turbulent wake state experience high induction factors, and higher loads than predicted by the momentum model for  $a \gtrsim 0.3$ . This has been accounted for with empirical correction models. This is especially important for FOWT systems that experience propeller state, which is characterized by a complete reversal in flow direction at the disc.

- The flow is assumed to be **steady** or **quasi-steady**. This assumption arises from the use of BET in determining the lift forces present on the blade elements, and does not allow for the accounting of dynamic inflow or dynamic stall effects. Dynamic inflow correction models calculate the time lag present on the induced velocity when the inflow conditions change, a result of the flow acceleration/deceleration. Dynamic stall correction models incorporate unsteady viscous-based airfoil aerodynamics into the BEM model.

### Finite Blade Correction Factor

The actuator disc model assumes an infinite number of blades upon which the loading acts, leading to an azimuthally constant axial momentum loss. For rotors with finite blades, flow that doesn't encounter the presence of a blade upon passing through the rotor loses less axial momentum compared to flow that encounters the blade. The difference leads to higher local values of induction factor at the location of the blade, especially in the tip region where tip vortices occur. These higher induction factors lead to reduced power and are thus labelled "tip losses". The Prandtl correction factor attempts to deal with this problem by modelling the wake as a series of impenetrable discs (see Figure 1.7a), which the surrounding fluid can flow into depending on the disc spacing. This is a representation of the actual wake, which takes a helical shape after being emitted from the trailing edge of the blades (see Figure 1.7b). Using this model, Prandtl derived a multiplicative factor between the azimuth-averaged induction factor and the induction factor present at the blade (which is used for blade element load calculations). This correction is commonly used due to its simplicity in modelling as a closed-form solution. This factor, for a three-bladed turbine at a tip-speed ratio of 6 (and a blade root at  $r = 0.2R$ ) is shown in Figure 1.8.

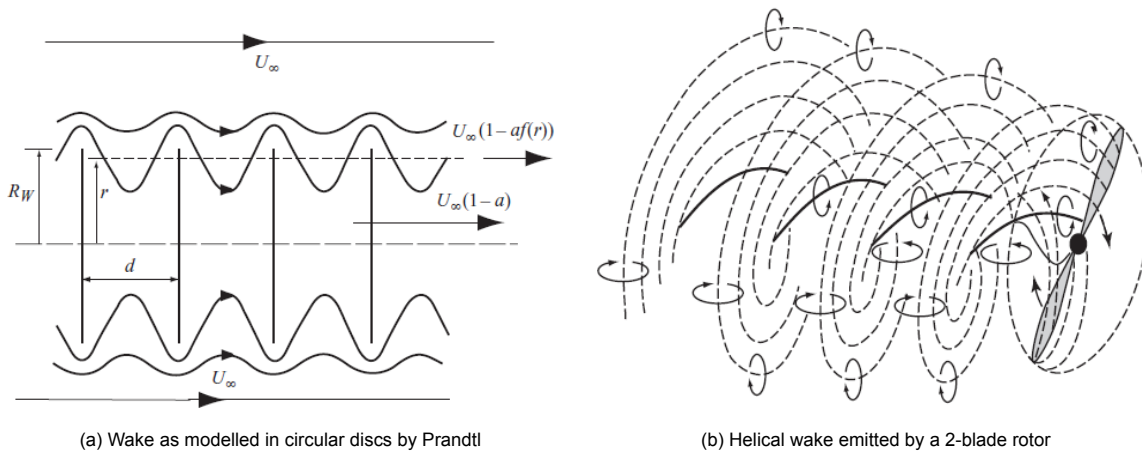


Figure 1.7: Diagrams illustrating rotor wake modelled (a) by Prandtl as discs, and (b) as a helix. Taken from [5].

Prandtl's approximation for the tip loss correction  $f$  physically represents the ratio between the azimuth-averaged induction factor, and the induction factor present at the blade (where the loading is actually present). In the classic BEM formulation, this induction is the one calculated by actuator disc theory, and thus the Prandtl factor serves as a correction to the actuator-disc-derived induction factor at a given span-wise location  $r$ . This can be expressed in closed form:

$$F_{tip}(r) = \frac{2}{\pi} \cos^{-1} \left( \exp \left[ -\frac{B}{2} \left( 1 - \frac{\lambda_r}{\lambda} \right) \sqrt{1 + \frac{V_t^2}{V_n^2}} \right] \right) \quad (1.31)$$

$$(1.32)$$

where  $B$  is the number of blades,  $\lambda$  and  $\lambda_r$  are the global and local tip-speed ratios, and  $a$  is the axial induction factor.  $V_t$  and  $V_n$  are the normal and tangential velocities defining the helical far-downstream wake pitch. Branlard et al. [4] summarize variations in Prandtl's tip-loss factor according to the assumption of  $V_t$  and  $V_n$ , in terms of the corresponding velocities at the rotor  $U_t$  and  $U_n$ :

- $V_n = U_n, V_t = U_t$ :

$$F_{Pr,1}(r) = \frac{2}{\pi} \cos^{-1} \left( \exp \left[ -\frac{B}{2} \left( 1 - \frac{\lambda_r}{\lambda} \right) \frac{1}{\sin(\phi(R))} \right] \right) \quad (1.33)$$

Where  $\phi$  is the inflow angle at the blade.

- $V_n = U_n = U_0, V_t = U_t = \Omega r$ :

$$F_{Pr,0}(r) = \frac{2}{\pi} \cos^{-1} \left( \exp \left[ -\frac{B}{2} \left( 1 - \frac{\lambda_r}{\lambda} \right) \sqrt{1 + \lambda^2} \right] \right) \quad (1.34)$$

This form is the one originally found by Prandtl (cited by Branlard et al. [4]).

- $V_n = U_n, V_t = U_t, R \sin(\phi(R)) \approx r \sin(\phi(r))$ :

$$F_{Gl}(r) = \frac{2}{\pi} \cos^{-1} \left( \exp \left[ -\frac{B}{2} \left( \frac{\lambda}{\lambda_r} - 1 \right) \frac{1}{\sin(\phi)} \right] \right) \quad (1.35)$$

This form was given by Glauert (cited by Branlard et al. [4]), and is the most common form of factor used in BEM codes.

- $V_n = U_n = U_0(1 - a), V_t = U_t, R/\sqrt{U_n(R)^2 + U_t(R)^2} \approx r/\sqrt{U_n(r)^2 + U_t(r)^2}, U_t = \Omega r$ :

$$F_{Bu} = \frac{2}{\pi} \cos^{-1} \left( \exp \left[ -\frac{B}{2} \left( \frac{\lambda}{\lambda_r} - 1 \right) \sqrt{1 + \left( \frac{\lambda_r}{1 - a} \right)^2} \right] \right) \quad (1.36)$$

This form was suggested by Burton [5], and can be visualized in Figure 1.8.

- $V_n = U_0(1 - a), V_t = \Omega r(1 + a')$ :

$$F_{Pr,2} = \frac{2}{\pi} \cos^{-1} \left( \exp \left[ -\frac{B}{2} \left( 1 - \frac{\lambda_r}{\lambda} \right) \sqrt{1 + \lambda^2 \left( \frac{1 + a'(R)}{1 - a(R)} \right)^2} \right] \right) \quad (1.37)$$

This form was suggested by Betz and Prandtl (cited by Branlard et al. [4]) as an 'exact' correction.

- $V_n = U_0(1 - a), V_t = \Omega r$ :

$$F_{Pr,3} = \frac{2}{\pi} \cos^{-1} \left( \exp \left[ -\frac{B}{2} \left( 1 - \frac{\lambda_r}{\lambda} \right) \sqrt{1 + \left( \frac{\lambda}{1 - a(R)} \right)^2} \right] \right) \quad (1.38)$$

This form was suggested by Betz and Prandtl (cited by Branlard et al. [4]) as an 'approximate' correction.

- $V_n = U_0 \left( 1 - \sqrt{F} \frac{a}{2} \right), V_t = \Omega r \left( 1 + 2\sqrt{F} \frac{a'}{2} \right)$ :

$$F_{Li} = \frac{2}{\pi} \cos^{-1} \left( \exp \left[ -\frac{B}{2} \left( 1 - \frac{\lambda_r}{\lambda} \right) \sqrt{1 + \lambda_r^2 \left( \frac{1 + 2\sqrt{F_{Li}} a'/2}{1 - \sqrt{F_{Li}} a/2} \right)^2} \right] \right) \quad (1.39)$$

This is a semi-empirical form given by Lindenburg [28].

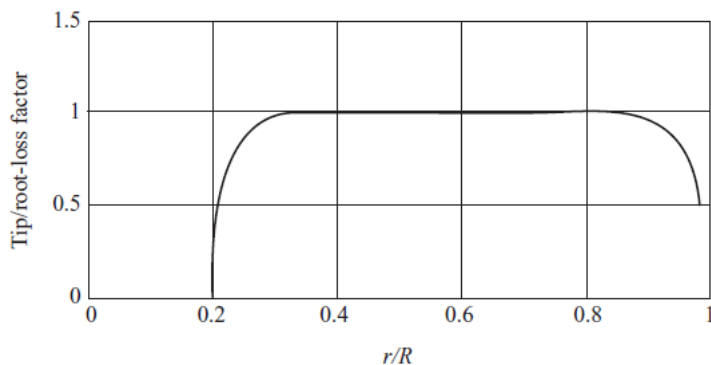


Figure 1.8: Prandtl correction factor  $F_{Bu}$  given in Equation 1.36 given  $B = 3$ ,  $\lambda = 6$ , and  $r_{root}/R = 0.2$ . Taken from [5].

Tip loss correction factors that do not follow the general Prandtl form include the factor given by Goldstein, Branlard, Shen et al., Xu and Sankar, and Sankar, all of which are cited by [4]. Figure 1.9 illustrates the variability in AEP given by these tip loss factors for two wind profiles, relative from their average.

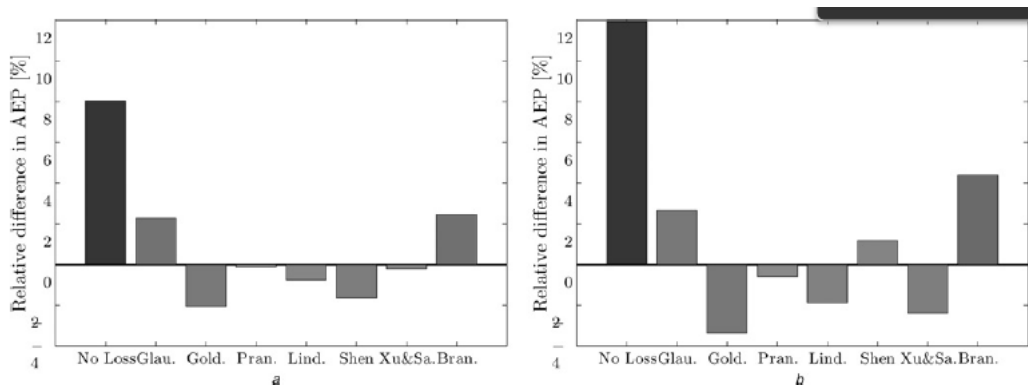


Figure 1.9: Relative Difference in AEP between selected tip-loss functions existing in literature. Taken from [4].

The difference in computed Average Energy Production (AEP) motivated the work of Branlard et al. [4] to produce a tip loss correction factor through means of a lifting-line model. The lifting-line model in question was run with a prescribed circulation distribution, which was parametrized to find tip-loss factor sensitivity to turbine operating conditions. A database was thus created, from which the factor is drawn upon depending on the closest match to circulation distribution. Figure 1.10 shows an example of this new tip-loss correction model compared to the Glauert-suggested tip correction factor (Equation 1.35) and the lifting-line code results.

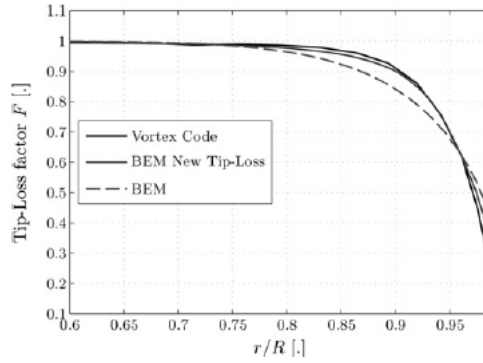


Figure 1.10: Comparison of tip loss factor suggested by Branlard et al. to that suggested by Glauert, as well as the lifting-line method. Adapted from [4].

### Glauert Correction for Heavily Loaded Turbines

Heavily loaded rotors are characterized by higher induction factors (usually in the induction factor regime of  $0.5 \leq a \leq 1$ ), wherein momentum theory calculates a reversal of flow direction far downstream. As the induction factor increases in this regime, the flow far downstream is predicted to become increasingly negative, leading to downstream turbulent wake re-circulation. An increasing induction factor leads to the movement of this wake re-circulation region closer and closer to the rotor itself, until the operating position  $a = 1$  where the flow is effectively blocked at the rotor and the rotor enters Vortex Ring State (VRS). This violates the basic stream-tube principle of momentum theory and thus the Glauert correction is often used to correct this inconsistency, wherein the momentum-predicted thrust force is replaced by a straight line fit to empirical results, shown in Figure 1.11. This correction is applied for  $a > 0.326$ , in accordance with where experimental results deviate from momentum-predicted values. Increasing the induction factor past this point places the rotor in propeller brake state, and reverses the direction of the flow at the rotor. Power is injected into the flow, and this state is called the propeller brake state. Typical wind turbine operation does not reach this point; induction factors are usually below 0.5.

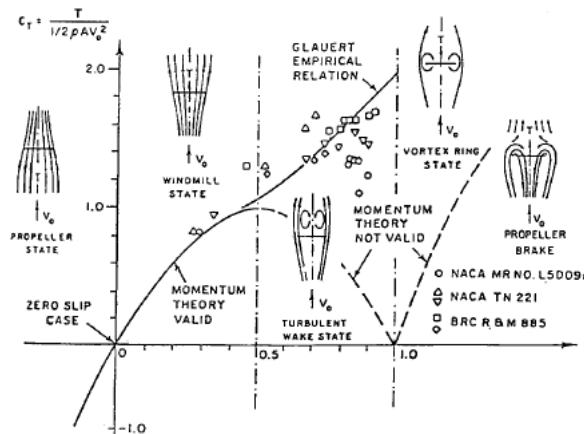


Figure 1.11: Wind turbine thrust coefficient ( $C_T$ ) against induction factor  $a$ . Taken from [47].

### Dynamic Inflow Models

The discussion on BEM models thus far assumes a steady or quasi-steady state of operation, in which the operating state of the rotor is solved for without consideration to the history of the fluid flow. However, unsteady models need to account for the momentum of the flow that exists when inflow changes occur. Models that estimate the effect of the flow momentum are named dynamic inflow models, and have been in use in the helicopter industry since their inception in the 1950s. Examples of models used in wind turbine applications are the Pitt-Peters, Øye, Larsen-Madsen, and ECN models. These models all retain the independent annular nature of the BEM module, and are summarized shortly as follows.

The **Pitt-Peters model** [34] requires an inflow distribution to be established, and calculates the annular thrust coefficient. This model is the most commonly used dynamic inflow model and takes the form of Equation 1.40.

$$\frac{1}{0.5\rho A_j V_0^2} \left[ \frac{8}{3\pi} \rho A_j r_j \frac{dv_j}{dt} + 2\rho A_j v_j (V_0 + v_j) \right] = C_{t,j} \quad (1.40)$$

This equation calculates the thrust coefficient acting on the  $j^{th}$  annular ring,  $C_{t,j}$ , given the area of the annular ring  $A_j$  and the average induced velocity  $v_j$  over the azimuth. The first term is dependent on the fluid acceleration, and represents the effect of its inertia. The second term stems from classic BEM theory, and represents the flow due to the pressure difference across the rotor (when modelled as an actuator disc).

The **Øye model** (cited in [58]) estimates the induced velocity by filtering the quasi-steady values through two first-order differential equations:

$$v_{int} + \tau_1 \frac{dv_{int}}{dt} = v_{qs} + b\tau_1 \frac{dv_{qs}}{dt} \quad (1.41)$$

$$v_z + \tau_2 \frac{dv_z}{dt} = v_{int} \quad (1.42)$$

Where  $v_{qs}$  is the quasi-steady value predicted by classic BEM theory,  $v_{int}$  is an intermediate velocity, and  $v_z$  is the final induced velocity. The two time constants are recommended (cited as Snel et al. in [58]) to be

$$\tau_1 = \frac{1.1}{1 - 1.3a} \frac{R}{V_0} \quad (1.43)$$

$$\tau_2 = \left( 0.39 - 0.26 \left( \frac{r_j}{R} \right)^2 \right) \tau_1 \quad (1.44)$$

Where  $a$  is the axial induction factor,  $R$  is the rotor radius, and  $r_j$  is the radius of the  $j^{th}$  annulus. The constant  $b$  is taken to be 0.6.

The **Larsen-Madsen model** performs a low-pass filtering of the steady-state induced velocities, similarly to the Øye model [25]:

$$a_{t_{i+1}} = a_{t_i} \exp\left(-\frac{\Delta t}{\tau}\right) + a_{qs} \left(1 - \exp\left(-\frac{\Delta t}{\tau}\right)\right) \quad (1.45)$$

$$\tau = 0.5 \frac{R}{U_{wake}} \approx 0.5 \frac{R}{aU_\infty} \quad (1.46)$$

The **ECN model** developed by Schepers calculates the annular thrust coefficient  $C_{t,j}$  as

$$\frac{R}{V_w} f_a \frac{da}{dt} + a(1 - a) = \frac{C_{t,j}}{4} f_a = 2\pi / \int_0^{2\pi} \frac{[1 - (r/R) \cos(\Phi_r)]}{[1 + (r/R)^2 - 2(r/R) \cos(\Phi_r)]} d\Phi_r \quad (1.47)$$

This model was derived with an integral approach, and full details can be found in [39].

### Dynamic Stall Models

Dynamic stall is a phenomena prominent for blades in viscous flow experiencing angle of attack variations at a time scale comparable to that which characterizes the onset of stall. This happens when the fluctuations are centered around the static stall angle of attack, and leads to the delay of stall beyond it. Oscillations in angle of attack lead to loading hysteresis, as shown in the left part of Figure 1.12.

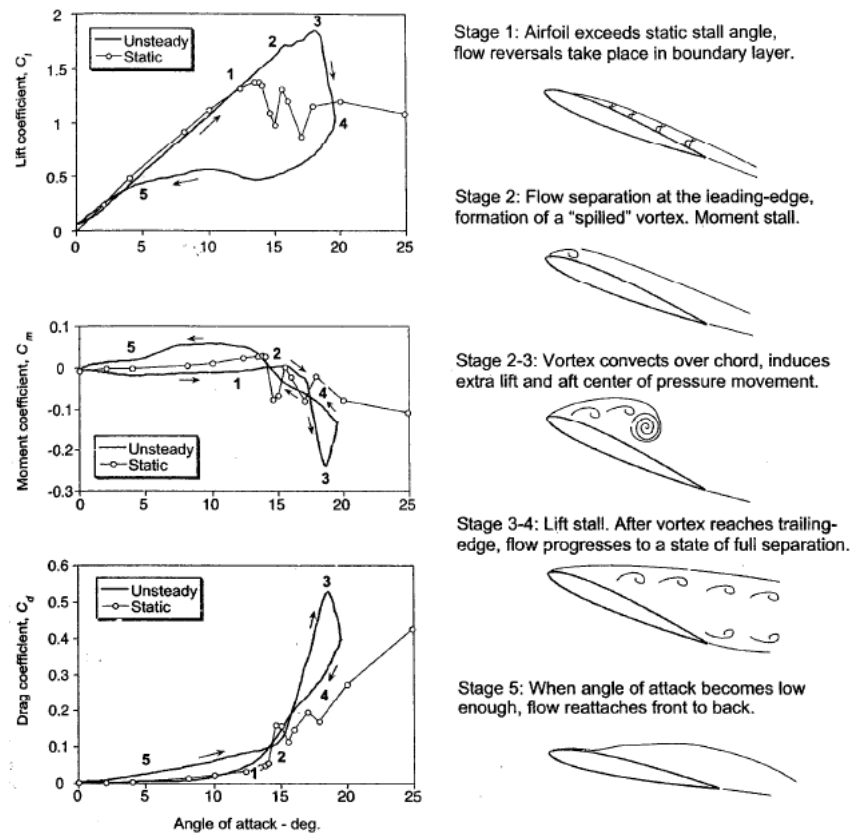


Figure 1.12: The lift/drag/moment hysteresis effects of dynamic stall on an oscillating 2D airfoil (left), along with a schematic of the associated flow morphology. Taken from [26].

Dynamic stall can be understood as a series of physical phenomena, in this case beginning with the airfoil exceeding the static stall angle of attack. Referred to as stage 1 in Figure 1.12, low-pressure re-circulation begins to occur in the boundary layer, increasing lift while keeping the drag and moment relatively constant. At stage 2, the flow separation results in a leading edge vortex which begins to convect along the chord. As this vortex is convected (stage 2  $\rightarrow$  3), the vortex grows in size and increases lift even further, while at the same time causing a large increase in drag and nose-down moment. Upon reaching the trailing edge, the vortex breaks down (stage 3  $\rightarrow$  4), along with its contribution to lift. The flow is completely separated at stage 4, and this state is known as lift stall. As the angle of attack decreases, flow reattachment eventually begins from the leading edge, and moves towards the back (stage 4  $\rightarrow$  5).

Dynamic BEM stall models were first developed for helicopter applications, such as the ONERA model [49] and the most commonly used Beddoes-Leishman model (cited by [33]). However, these were adapted to wind turbine applications by accounting for thicker airfoils and eliminating compressibility effects. The Beddoes-Leishman model, which was adapted to wind turbine applications by Gupta and Leishman [14], consists of four modules that each represent an aspect of dynamic stall.

The first module, the **attached flow module**, calculates the delay in lift due to a step change in angle of attack, using Theodorsen's theory [48] of potential (attached) flow over a flat plate. The circulatory contribution to normal force  $C_{N,n}^C$  stems from the wake emitted just prior to the step change, which is momentarily close enough to influence the loading on the blade. The non-circulatory contribution  $C_{N,n}^{NC}$  to the normal force is an 'added mass' effect, which stems from the inertia of the displaced air. Using

the subscript  $n$  to refer to the current time step, the total normal force is calculated as

$$C_{N,n}^p = C_{N,n}^c + C_{N,n}^{NC} \quad (1.48)$$

$$C_{N,n}^c = C_{N\alpha}(\alpha_{E,n} - \alpha_0) = C_{N\alpha}(\alpha_n - X_n - Y_n - \alpha_0) \quad (1.49)$$

$$X_n = X_{n-1} \exp(-b_1 \Delta S) + A_1 \Delta \alpha_n \exp(-b_1 \Delta S/2) \quad (1.50)$$

$$Y_n = Y_{n-1} \exp(-b_2 \Delta S) + A_2 \Delta \alpha_n \exp(-b_2 \Delta S/2) \quad (1.51)$$

$$C_{N,n}^{NC} = \frac{4K_\alpha c}{U_\infty} \left( \frac{\delta \alpha_n}{\Delta t} - D_n \right) \quad (1.52)$$

$$D_n = D_{n-1} \exp\left(\frac{-\Delta t}{K_\alpha T_l}\right) + \left(\frac{\Delta \alpha_n - \Delta \alpha_{n-1}}{\Delta t}\right) \exp\left(\frac{-\Delta t}{2K_\alpha T_l}\right) \quad (1.53)$$

where  $C_{N\alpha}$  is the inviscid lift slope,  $\alpha_E$  is the effective angle of attack at the airfoil section (subtracting the lag terms  $X_n$  and  $Y_n$  from the angle of attack  $\alpha_n$ ),  $\alpha_0$  is the quasi-steady angle of attack at zero lift,  $1/b_{1,2}$  and  $A_{1,2}$  are the time constants and coefficients of the lag terms,  $\Delta S = 2U_\infty \Delta t/c$  is the non-dimensional time increment,  $K_\alpha$  is a factor relating to the Mach number of the flow (constant for wind turbine applications), and  $T_l$  is a time factor relating to the lag term of the non-circulatory component  $D_n$ . The total normal force  $C_{N,n}^p$  is finally calculated as the linear sum of the circulatory and non-circulatory contributions.

The second module, the **trailing edge separation module**, calculates the non-linear effect of the separation at the trailing edge, using a parameter  $f$  that describes the location of the separation point. With the extra term modelled from Kirchhoff's theory, the total unsteady normal force is rewritten from the previous formula as

$$C_{N,n}^f = C_{N\alpha} \left( \frac{1 + \sqrt{f''_n}}{2} \right)^2 (\alpha_{E,n} - \alpha_0) + C_{N,n}^{NC} \quad (1.54)$$

$$f''_n = f'_n - D_{f,n} \quad (1.55)$$

$$D_{f,n} = D_{f,n-1} \exp\left(\frac{-\Delta S}{T_f}\right) + (f'_n - f'_{n-1}) \exp\left(\frac{-\Delta S}{2T_f}\right) \quad (1.56)$$

where values of  $f'$  were interpolated from the relation given in Equation 1.60 for steady flow, at the effective angle of attack  $\alpha_f$ , calculated as

$$\alpha_{f,n} = \frac{C'_{N,n}}{C_{N\alpha}} + \alpha_0 \quad (1.57)$$

$$C'_{N,n} = C_{N,n}^p - D_{p,n} \quad (1.58)$$

$$D_{p,n} = D_{p,n-1} \exp\left(\frac{-\Delta S}{T_p}\right) + (C_{N,n}^p - C_{N,n-1}^p) \exp\left(\frac{-\Delta S}{2T_p}\right) \quad (1.59)$$

$$C_N = C_{N\alpha} \left( \frac{1 + \sqrt{f}}{2} \right)^2 (\alpha - \alpha_0) \quad (1.60)$$

where  $T_p$  and  $T_f$  are time constants related to the pressure and boundary layer lag terms  $D_{p,n}$  and  $D_{p,f}$ , respectively.

The third module, the **leading edge separation module**, calculates a vortex time parameter  $\tau_v$  which is used to track the location of the leading edge vortex. The condition that begins the time marching of this parameter is given by the unsteady leading edge pressure, modelled as  $C'_N$ , reaching a critical value  $C_{N_1}$ . The position of the vortex at the leading edge is reset to  $\tau_v = 0$  as the angle of attack increases at the beginning of the cycle, until  $\tau_v = T_{vl}$  once the vortex reaches the trailing edge. The vortex is assumed to convect at a rate of 45% of the free-stream velocity.

$$\tau_{v,n} = \begin{cases} \tau_{v,n-1}, & C'_N > C_{N_1} \\ 0, & C'_N < C_{N_1} \text{ \& } \Delta \alpha_N > 0 \end{cases} \quad (1.61)$$

The fourth module, the **vortex lift module**, calculates the contribution to normal force of the leading edge vortex as it traverses over the chord. The leading edge vortex contribution to normal force  $C_{N,n}^v$  is calculated as

$$C_{N,n}^v = \begin{cases} C_{N,n-1}^v \exp\left(\frac{-\Delta s}{T_v}\right) + (C_{v,n} - C_{v,n-1}) \exp\left(\frac{-\Delta s}{2T_v}\right), & 0 < \tau_{v,n} < T_{vl} \\ C_{N,n-1}^v \exp\left(\frac{-\Delta s}{T_v}\right), & \text{else} \end{cases} \quad (1.62)$$

$$C_{v,n} = C_{N,n}^c \left[ 1 - \left( 1 + \frac{1 + \sqrt{f''_n}}{2} \right)^2 \right] \quad (1.63)$$

Where  $T_v$  is a vortex decay constant. The total unsteady normal force adds the vortex lift contribution to the normal force calculated by the first two modules:

$$C_{N,n} = C_{N,n}^f + C_{N,n}^v \quad (1.64)$$

### Use of BEM Codes in Modelling FOWT Systems

In fixed-base systems, the reference frame of the stream-tube and rotor are the same, meaning that assumption of steady flow hold still. However, as soon as the rotor begins to accelerate, this assumption is violated. In cases of mild surge, this assumption is relaxed, with a dynamic inflow model estimating the effects of the accelerated motion. However, the possibility of re-circulation around the edge of the rotor was described by Sebastian and Lackner [45] as VRS, leading to the invalidation of 1D actuator disc theory and BEM models. Tran et al. [52] found a difference of 30% in the maximum power coefficient between a BEM model and CFD results for these conditions (shown in Table 1.6), suggesting that improvements needed to be implemented for BEM models to be able to accurately predict the loads in severe surge. More recently, Ferreira [13] challenged the hypothesis that actuator disc theory is invalid by explaining that VRS are defined in the inertial reference frame of the stream-tube. As such, the application of momentum theory in the reference frame of the actuator disc would require further apparent forces. Thus, even when the surge motion is severe enough to result in blade-wake interactions, these do not constitute VRS and may be handled by a dynamic inflow model. Propeller case is also defined in the inertial reference frame of the stream-tube, meaning that even if the rotor may undergo sufficient loading to cause an overall direction change of thrust, the stream-tube remains in normal operating condition, albeit with a rapidly oscillating rotor moving along its axis. Ferreira stipulated and showed that a modified Larsen-Madsen dynamic inflow model is able to handle the effects of a surging actuator disc, even in cases of severe surge ( $v_{max} \leq 2.0$ ).

### 1.2.3. Computational Fluid Dynamics Models

Computational Fluid Dynamics (CFD) methods seek to characterize a fluid flowing within a defined volume, by discretizing that volume and solving for flow parameters (mass, momentum, energy) either at points (finite difference methods) or over cell volumes (finite volume methods). The latter of these is the most common CFD method, as it conserves these parameters by design. This technique is applicable for general flow situations, and has been adapted for wind turbine applications. This section will provide a short summary of the work that has been conducted to predict the unsteady aerodynamics of FOWT systems in surge motion using CFD methods, including key results.

Reynolds-Averaged Navier Stokes (RANS) models are the simplest form of CFD models, which attempt to solve for time-averaged flow parameters using specific models to predict turbulent fluctuations. Table 1.4 gives an overview of the studies which study FOWT systems under surge motion, along with their respective explored conditions.

Study	Amplitude $\frac{A_s}{D}$	Frequency $k$	Maximum Velocity $v_{max}$
de Vaal [7]	0.032 - 0.127	1.429 - 5.625	0.045 - 0.714
Kyle et al. [24]	0.075	8.753-14.004	0.653 - 1.045
Micallef & Sant [32]	0.008	7.714	0.062
Tran & Kim [52]	0.032 - 0.127	1.429 - 2.625	0.045 - 1.081
Chen et al. [6]	0.008 - 0.016	6.941 - 13.893	0.055 - 0.221
Liu et al. [30]	0.016	5.792	0.092

Table 1.4: CFD studies on FOWT systems in surge

Tran et al. used a RANS model and a moving mesh to calculate the unsteady loads of a FOWT system undergoing yaw and pitch motion [50][51][54]. They were able to capture and visualize the variation in tip vortex creation at different moments of the pitching motion, as well as unsteady effects such as dynamic stall and vortex shedding. Comparisons suggested over-estimation of thrust and power during pitching motion when using unsteady BEM models, compared with the unsteady CFD models. Tran et al. also investigated the unsteady loads of a FOWT undergoing surge motion [52] with the same CFD technique. Among the results found in this study are the changes (over a surge period) in the span-wise pressure coefficient distribution, the gap distance between shed tip vortices, the wake strength behind the blades, and the rotor power and thrust values over time. Figure 1.14 shows vorticity contours given a surge amplitude and frequency of  $A_s = 16m$  &  $\omega_s = 0.5rad/s$ , displaying clearly the changing gap between tip vortices. Figure 1.13 illustrates the direction of motion of the rotor at the labelled  $T_i$  points for reference. Figure 1.15 shows the variation in pressure coefficient at  $r/R = 0.75, 0.9$  for  $A_s = 4, 8, 16m$  &  $\omega_s = 0.5rad/s$ . While these conditions aren't sufficient to induce negative effective wind speed, they do show a stark decrease in the gap between vortices as the rotor moves downwind, compared to its upwind motion.

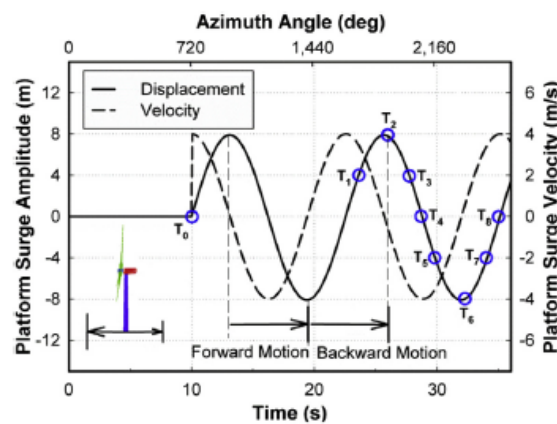


Figure 1.13: Relative position of the rotor used by Tran et al. for  $A_s = 8m$ ,  $\omega_s = 0.5rad/s$ . Taken from [52].

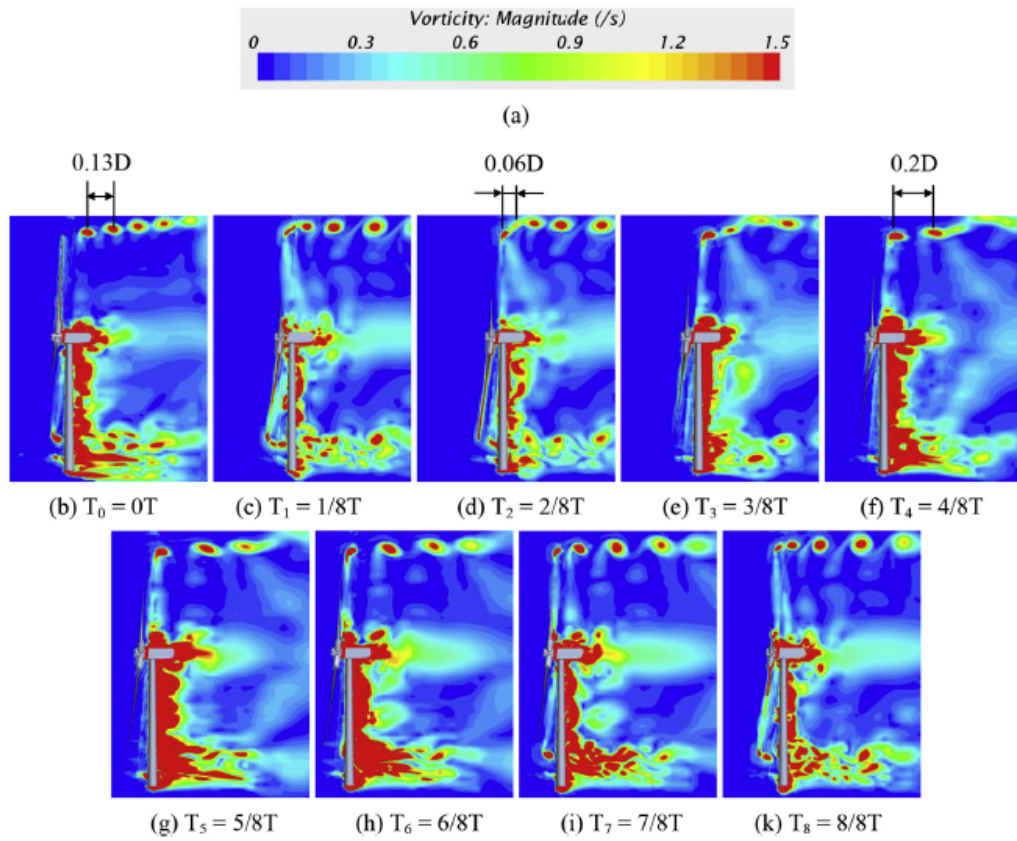


Figure 1.14: Vorticity contours due to platform surge motion for  $A_s = 16m$ ,  $\omega_s = 0.5rad/s$ . Taken from [52].

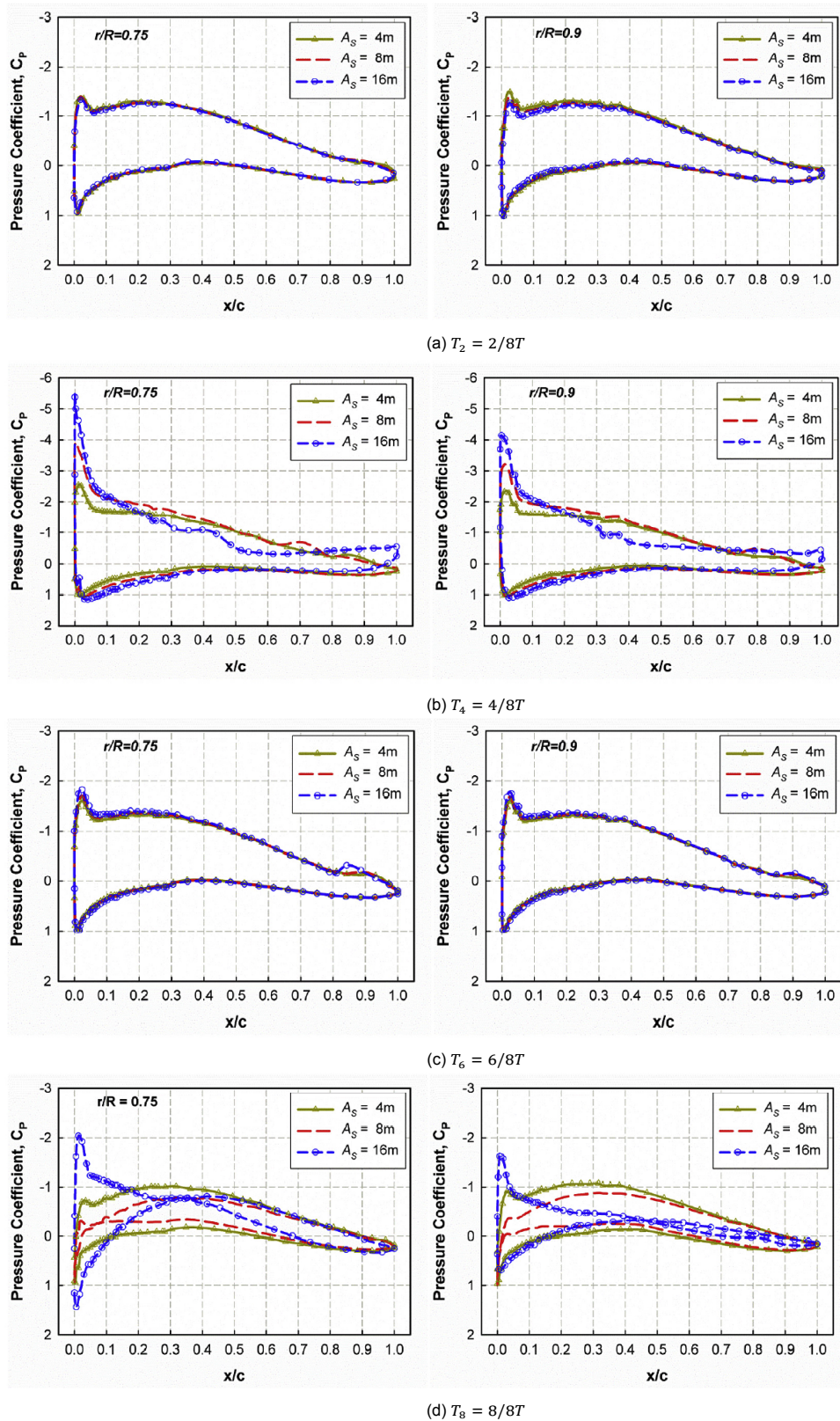


Figure 1.15: Pressure coefficients at selected span-wise locations for  $A_s = 4, 8, 16m$ ,  $\omega_s = 0.5rad/s$ , at selected points in the surge cycle. Taken from [52].

Liu et al. [30] performed an aeroelastic analysis using an FSI solver, coupling the pimpleDyMFOam CFD solver in the open-source OpenFOAM package, with the open-source MBDyn dynamics package.

They once again showed an overestimation of thrust and power when using a BEM code (FAST v8), and were also able to visualize the unsteady tip vortex shedding variations along the surge period, for surge motion given  $A_s = 2m$  &  $\omega_s = 0.5rad/s$ .

Several examples of methods that couple CFD methods with hydrodynamic solvers exist as well. Tran et al. [53] presented a methodology for an aero-hydrodynamic FOWT solver that models all 6 DOFs using STAR-CCM+, and Liu et al. [29] presented a methodology coupling OpenFOAM. Both required coupled FSI solvers that would solve for the kinematics of the FOWT system in conjunction with the aerodynamic loads.

Kyle et al. [24] used a CFD method to explore the dynamic response of a wind turbine to surge conditions wherein the effective wind velocity at the rotor becomes briefly negative. The cases explored by Kyle can be found in Table 1.5.

The following were the cases studied:

Label	Rotation Rate [rpm]	$U_\infty$ [m/s]	$A_s$ [m]	Surge Period [s]
RF	12.10	11.4	-	-
RS	12.10	11.4	9.4	8.1
BF	8.47	7.0	-	-
BS	8.47	7.0	9.4	8.1

Table 1.5: Load cases investigated by Kyle et al. [24]

They identified negative thrust, corresponding to propeller state, at moments when the effective wind speed was negative. This negative thrust coefficient is shown for the BS case (compared to the BF case) in Figure 1.16, between  $t \approx 11s \rightarrow 13s$ . Vorticity iso-volumes were captured during this period, with the cases of  $t = 11.5s, 12.0s, 12.5s, 13.0s$  shown in Figure 1.17. The close-ups for the latter two cases highlight the blade-vortex interaction at the root, which occurs when the blade moves into the position of the previous blade's wake faster than that wake can convect downstream. The thickness of the root vortices, combined with its slow convection rate, is why this interaction happens at the root. Kyle et al. point to these interactions as evidence of VRS, and support that argument by pointing to the heavily loaded nature of the rotor (a low reference wind speed directly implies a high thrust coefficient).

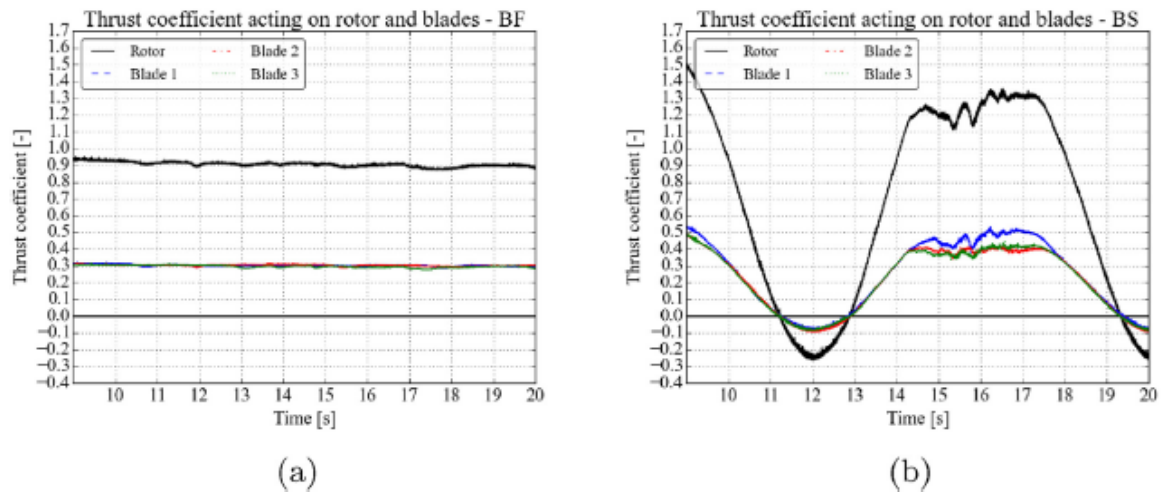


Figure 1.16: Thrust coefficient acting on the total rotor and individual blades for (a) the BF case and (b) the BS case. Taken from [24].

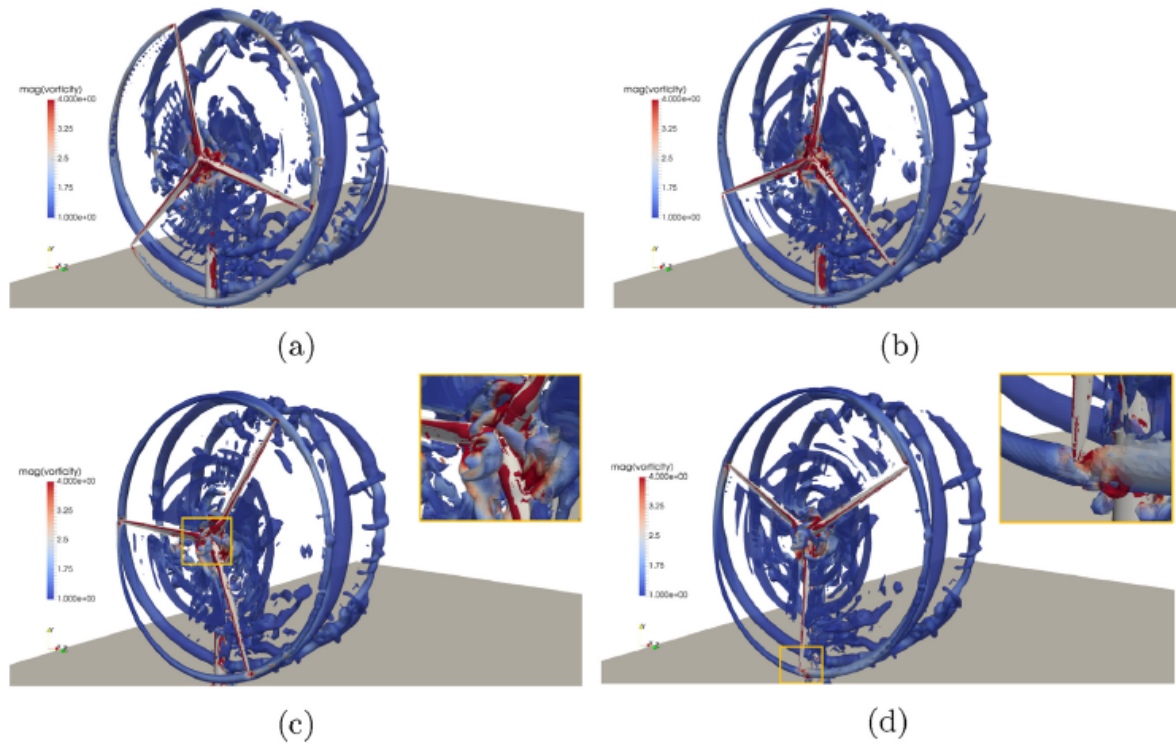


Figure 1.17: Vorticity iso-volumes for the BS case for (a)  $t = 11.5s$ , (b)  $t = 12.0s$ , (c)  $t = 12.5s$ , and (d)  $t = 13.0s$ . Taken from [24].

The conditions of CFD studies conducted on FOWT methods undergoing surge motion are summarized in Table 1.6. As can be seen from the summary of results conducted with CFD, limited literature exists on the dynamic response of FOWT systems under severe surge conditions. Of the two studies, only that by Kyle et al. focuses on the unsteady aerodynamic phenomena that occur, namely propeller state and the blade-vortex interactions. This study will serve as a good basis for replication with an FVM.

Study	$A_s$ [m]	$\omega_s$ [rad/s]	$\lambda$	Lowest Effective Wind Speed $V_{eff}$ [m/s]
Tran et al. [52]	4,8,16	0.127	7.26	8.97
	4,8,16	0.246	7.26	7.06
	4,8,16	0.500	7.26	3.00
	4,8,16	0.770	7.26	-1.32
Liu et al. [30]	2	0.52	7.00	10.35
Kyle et al. [24]	9.4	0.78	7.00, 7.98	-0.29

Table 1.6: Conditions of CFD studies on FOWT surge motion

### 1.2.4. Free Vortex Methods

#### Introduction to Potential Flow Theory

As with CFD methods, the Free Vortex Method (FVM) begins with the differential form of the Navier-Stokes equations, which represent the conservation of mass (Equation 1.65), momentum (Equation 1.66), and energy (Equation 1.67) of a fluid flow, given initial and boundary conditions:

$$\frac{D\rho}{Dt} + \rho \nabla \cdot \vec{v} = 0 \quad (1.65)$$

$$\rho \frac{Dq_i}{Dt} = \rho f_i + \frac{\partial t_{ij}}{\partial x_j} \quad (1.66)$$

$$\frac{D\left(e + \frac{1}{2}V^2\right)}{Dt} = \dot{q}_{flux} + \frac{1}{\rho} \left[ \nabla(k\nabla T) - \nabla(p\vec{v}) + \frac{\partial q_j \tau_{ij}}{\partial x_i} \right] \quad (1.67)$$

Which, after applying the assumptions of incompressible, adiabatic and inviscid flow, reduce to the following mass and momentum conservation equations.

$$\nabla \cdot \vec{v} = 0 \quad (1.68)$$

$$\frac{\partial \vec{v}}{\partial t} + (\vec{v} \cdot \nabla) \vec{v} + \nabla \frac{p}{\rho} = \vec{0} \quad (1.69)$$

Potential flow further assumes the flow is irrotational, giving rise to a scalar parameter known as the potential function  $\Phi$ . For scalar quantities, the following vector identity exists:

$$\nabla \times \nabla \phi = 0 \quad (1.70)$$

Irrotational flow, which is characterized by  $\nabla \times \vec{v} = 0$ , thus allows the potential function to be defined as the scalar field whose gradient provides the velocity of the flow:

$$\nabla \Phi = \vec{v} \quad (1.71)$$

Substitution of the potential function into Equation 1.68 gives the Laplace equation  $\nabla^2 \Phi = 0$ , which can be solved if given the flow boundary condition at the surface of the body. To calculate pressure, the unsteady Bernoulli equation is first derived from the substitution of  $\Phi$  into Equation 1.69, along with some manipulation. Non-dimensionalizing this equation provides a means of directly obtaining the pressure coefficient  $C_p$ .

$$\frac{p_{ref} - p}{\rho} = \frac{Q^2}{2} - \frac{v_{ref}^2}{2} + \frac{\partial \Phi}{\partial t} \quad (1.72)$$

$$C_p := \frac{p - p_{ref}}{\frac{1}{2}\rho v_{ref}^2} = 1 - \frac{Q^2}{v_{ref}^2} - \frac{2}{v_{ref}^2} \frac{\partial \Phi}{\partial t} \quad (1.73)$$

Where  $Q$  is the local velocity, and  $v_{ref}$  is the reference velocity, which for rotor cases can be taken as either the free-stream velocity, the tip rotational velocity, or the local rotational velocity of the blade, depending on the application. These equations, by themselves, do not allow for direct numerical computation of the flow around a body. Panel methods must therefore act upon a discretized form of these equations, which thus form the basis of panel methods.

#### Panel Methods

The Laplace equation can be solved by any of a number of elementary solutions, and due to its linearity, a superposition of them as well. For airfoil/wake applications, source and doublet solutions are most useful, and will be used in this study. The source solution assumes a singular point source of flow which emanates equally in all directions with a strength  $\sigma$ , inducing a velocity (in spherical coordinates) and potential of

$$\vec{v} = \left( \frac{\sigma}{4\pi r^2}, 0, 0 \right) \quad (1.74)$$

$$\Phi = \frac{-\sigma}{4\pi r} \quad (1.75)$$

A source of negative strength  $-\sigma$  is known as a sink, and has the opposite behaviour of a source. This means that it attracts flow towards its singularity, inducing a velocity and potential negative to that of a source. When a source and sink of equal (but opposite) strengths are located infinitesimally close to each other, the solution is known as a doublet. A doublet of strength  $\mu$  induces a velocity (in spherical coordinates) and potential of

$$\vec{v} = \left( \frac{\mu \cos \theta}{2\pi r^3}, \frac{\mu \sin \theta}{4\pi r^3}, 0 \right) \quad (1.76)$$

$$\Phi = \frac{-\vec{\mu} \cdot \vec{r}}{4\pi r^3} \quad (1.77)$$

Where  $\vec{\mu}$  is the doublet strength vector pointing in the direction of the source, as shown in Figure 1.18.

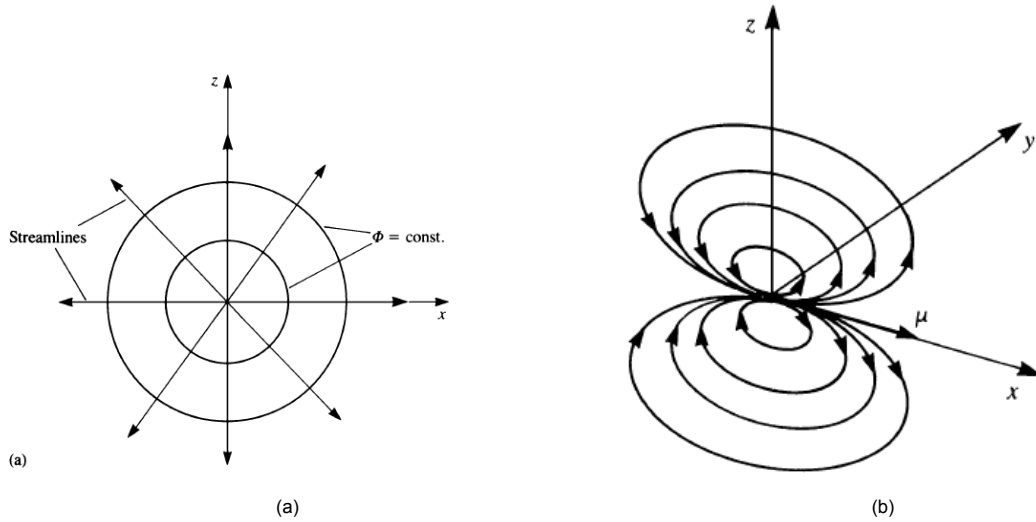


Figure 1.18: Sketch of the streamlines of (a) source and (b) doublet distributions. Taken from [21].

In the case of panel methods, these solutions are extended from point singularities to surface distributions, where the surface is either that of the airfoil or the wake. The most common methodology, and that which will be explored here, is the source-doublet distribution wherein the airfoil surface has both an associated source distribution (to model thickness), as well as an associated doublet distribution (to model surface vorticity). The wake surface is correspondingly associated with a doublet distribution to model wake vorticity.

Given a potential distribution along a surface, the potential at any point in the domain can be calculated as

$$\Phi(\vec{x}) = \frac{1}{4\pi} \int_S \left( \frac{1}{r} \nabla \Phi - \Phi \nabla \frac{1}{r} \right) \cdot \vec{n} dS \quad (1.78)$$

Where  $\vec{n}$  is the normal vector to the surface at that location. Upon calculating the potential in the domain, the velocity and pressure at any point in the domain can also be calculated, meaning that the unsteady convection of the wake is purely a result of the potential distribution along the surfaces. For the source-doublet distribution, this is given as

$$\Phi(\vec{x}) = \frac{1}{4\pi} \int_{S_B} \left[ \sigma \frac{1}{r} - \mu \frac{\partial}{\partial n} \left( \frac{1}{r} \right) \right] dS + \frac{1}{4\pi} \int_{S_W} \left[ \mu \frac{\partial}{\partial n} \left( \frac{1}{r} \right) \right] dS \quad (1.79)$$

Where  $S_B$  and  $S_W$  denote the body and wake surfaces, respectively. This formulation requires the source strength to be equal to the difference in normal velocity at the surface, and the doublet distribution to be equal to the difference in potential at the surface:

$$\sigma = \frac{\partial \Phi_i}{\partial n} - \frac{\partial \Phi}{\partial n} \quad (1.80)$$

$$\mu = \Phi_i - \Phi \quad (1.81)$$

Where the subscript  $i$  denotes internal quantities. While theoretically the domain can remain a geometrically curved geometry with arbitrarily high-order source and doublet distributions, panel methods discretize the geometry into flat panels to allow for the domain to be solved simply with existing formulae. The distributions are also usually limited to constant values for each of the panels, to provide a linear basis to the solution. Thus, the airfoil is split into (often quadrilateral) panels, each with a source strength  $\sigma_j$  and doublet strength  $\mu_j$ . The wake is similarly split into panels with doublet strengths  $\mu_K$ . Figure 1.19 shows an example discretization of a 3D wing with this distribution. However, it is common to represent the doublet distributions along the surface of a panel as a constant strength vortex sheet (with strength equal to the derivative of the doublet distribution), along with a vortex ring at the boundary of the panel (with strength equal to the doublet strength at that location). This equivalence was proved by Hess [16]) and allows for faster computational speed.

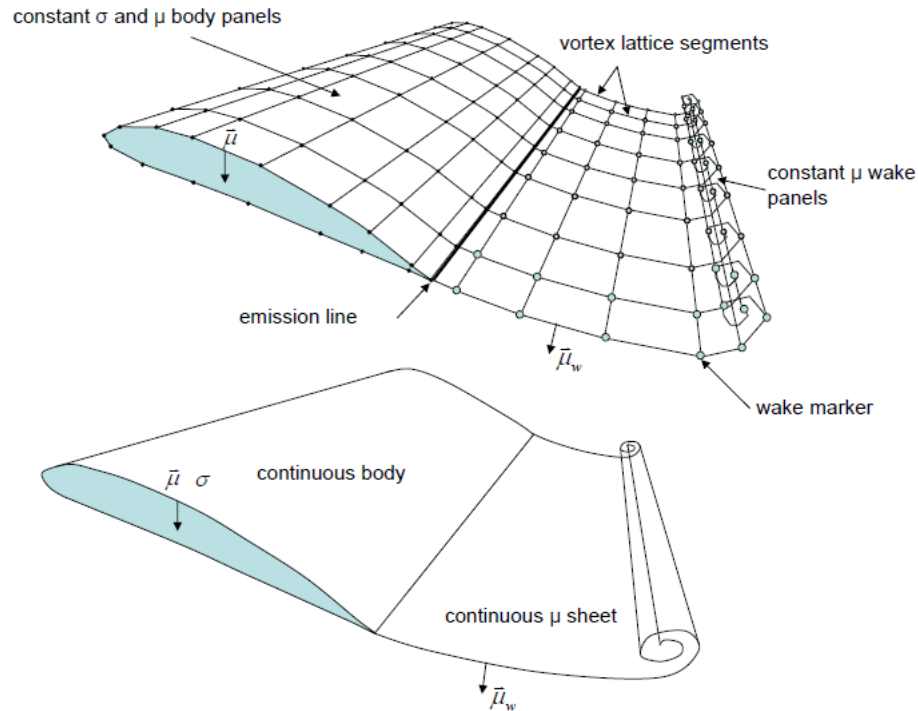


Figure 1.19: Panel discretization of a 3D wing with a source-doublet distribution. Taken from [10].

At the surface, the boundary condition of the solid airfoil surface (zero normal flow) can be implemented through either a Dirichlet formulation or a Neumann formulation. The Dirichlet formulation imposes the potential inside the body to be constant, meaning that its gradient (and thus the velocity) is zero. This can be implemented directly through Equation 1.79. The Neumann condition imposes a normal velocity of zero at the surface, and thus needs to be implemented through the derivative of Equation 1.79 in the normal direction. The bulk of panel method computations is finding the combination of source and doublet values associated with each of the panels such that this boundary condition is satisfied. Given that the change of potential in the normal direction is zero, the form of the Dirichlet formulation allows the source strength to be reduced to the local kinematic surface velocity in the normal direction:

$$\sigma = -\frac{\partial \Phi}{\partial n} \quad (1.82)$$

The Kutta Condition, which requires that the flow leave the trailing edge in a smooth fashion, is derived from physical limits. Given a finite-angled edge, the flow cannot turn around the angle without approaching an infinite turning velocity. This implies the need to have no pressure difference across wake panels at the trailing edge, which is represented by source-doublet formulation as a zero doublet strength at the trailing edge. Thus, the strength of the wake panels attached to the trailing edge can

be calculated as the difference in strengths of the attached upper and lower body panels:

$$\mu_{W,attached} = \mu_{B,upper} - \mu_{B,lower} \quad (1.83)$$

The governing equation to be solved can be obtained by expressing the overall surface integrals as the sum of their parts. In this equation, the cumulative effect of the  $N_{body}$  body panels and  $N_{wake}$  wake panels at the collocation point  $i$  is calculated such that the Dirichlet boundary condition is satisfied:

$$\sum_{j=1}^{N_{body\ panels}} \frac{-1}{4\pi} \int_{S_{body\ panel\ j}} \mu_j \frac{\partial}{\partial n_j} \left( \frac{1}{r_{ij}} \right) dS_j + \sum_{j=1}^{N_{body\ panels}} \int_{S_{body\ panel\ j}} \sigma_j \frac{1}{r_{ij}} dS_j \quad (1.84)$$

$$+ \sum_{k=1}^{N_{wake\ panels}} \frac{1}{4\pi} \int_{S_{wake\ panel\ k}} \mu_k \frac{\partial}{\partial n_k} \left( \frac{1}{r_{ik}} \right) dS_k = 0 \quad (1.85)$$

This can be solved as a linear system of equations:

$$A_{ij}\mu_j + B_{ij}\sigma_j + C_{ik}\mu_k = 0; \quad (1.86)$$

$$A_{ij} = \frac{-1}{4\pi} \int_{S_j} \frac{\partial}{\partial n_j} \left( \frac{1}{r_{ij}} \right) dS_j$$

$$B_{ij} = \int_{S_j} \frac{1}{r_{ij}} dS_j$$

$$C_{ik} = \frac{1}{4\pi} \int_{S_k} \frac{\partial}{\partial n_k} \left( \frac{1}{r_{ik}} \right) dS_k$$

$$i, j = 1 \dots N_{body\ panels}$$

$$k = 1 \dots N_{wake\ panels}$$

Where the coefficient matrices  $A_{ij}$  and  $B_{ij}$  represent the influence coefficients of the body source and doublet strengths, respectively, on the body panel collocation points. These therefore need to be determined once from the problem geometry. In the unsteady formulation, the coefficient matrix  $C_{ij}$ , which represents the influence coefficients of the wake doublet strengths on the body panel collocation points, needs to be re-calculated at every time step.

### Source-Doublet Panel Method Algorithm

The following example of an algorithm given by Katz and Plotkin [21] is as follows:

1. Input of following information:
  - Mesh geometry, including the spatial coordinates of each panel vertex and a discretization guide that details how the vertices form panels
  - Number of rotor revolutions to be performed
  - Azimuthal angle increment per time step
  - Free-stream conditions including incoming wind velocity, air density
  - Operating conditions including rotor speed
  - Vortex parameters that describe core velocity, core growth, vortex deformation, and initial core size
2. Initial estimate of the source and doublet distributions on the bodies
3. Kinematic rotation of the blades according to the rotational velocity  $\Omega$
4. Calculation of the latest wake strength using the Kutta condition at the trailing edge (Equation 1.83).

5. Calculation of the doublet strengths  $\mu_j$  for the body panels as per Equation 1.86. The body source strengths  $\sigma_j$  are determined from the normal component of the kinematic velocity experienced at the panels, and the wake doublet strengths  $\mu_k$  are held constant through time, meaning that ultimately they were all calculated by the Kutta condition.
6. Calculate the total induced velocity at the location of every wake point using the induction laws of the individual panels, and use this to update the wake vertex for the next azimuthal time increment. A first-order scheme can be used for this purpose.
7. Calculate the surface pressures on the body panels (Equation 1.73).
8. Perform the kinematic rotation (step 3) and repeat the steps until the desired number of rotor revolutions have been passed.

### Panel Edge Singularities

Because the wake lattice segments contain singularities at their edges, additional models to represent physical reality should be implemented. These seek to replicate the effect of real viscous vortices with the following features:

- A finite core which puts a limit on the singularity approaching the center
- Growth of the core due to viscous diffusion, accelerated in the case of turbulence
- Deformation of the core due to the self-induction of the wake
- An initial core size at the trailing edge

These models provide an estimation for the swirl velocity inside the vortex core, and range in simplicity and fidelity. The Ramasamy-Leishman (RL) model attempts to model the effect of interacting vortex core layers, and to show dependence on the vortex Reynolds number  $Re_v = \Gamma/\nu$ . Ramasamy et al. give the swirl velocity explicitly as a function of exponential coefficients (cited in [10]):

$$V_\theta = \frac{\Gamma}{2\pi r} \left[ 1 - \sum_{n=1}^3 a_n e^{-b_n \bar{r}^2} \right] \quad (1.87)$$

Where  $\Gamma$  is the vortex circulation,  $V_\theta$  is the swirl velocity field, and  $\bar{r}$  is the normalized core radius with the vortex core size. The RL model further gives the core growth model implementation as the following approximation:

$$r_c = \sqrt{r_0^2 + 4\alpha_L(1 + Re_v a')vt}; \quad a' = 6.5 \cdot 10^{-5}; \quad \alpha_L = 1.25643 \quad (1.88)$$

Where  $r_0$  is the initial vortex core size,  $t$  is the time, and  $Re_v$  is the vortex  $Re$  number. The deformation of the core follows from conservation of mass wherein positive strain causes radius reduction, and vice versa. A constant circulation (as per the Helmholtz laws) causes higher swirl velocities and vorticities:

$$\Delta r_c = r_{c,0} \left[ 1 - \frac{1}{\sqrt{1 + \epsilon}} \right]; \quad \epsilon = \frac{\Delta l}{l} \quad (1.89)$$

Where  $r_{c,0}$  is the core size without straining,  $\Delta r_c$  is the change in core size with straining, and  $l$  and  $\Delta l$  are the length of the vortex filament and change thereof. The initial core size can be calculated by a number of models.

### Assumptions

FVM methods hold the following assumptions, which must be corrected for, depending on the situation:

1. The flow is assumed to be **incompressible**, which is reasonable at the Mach numbers wind turbines typically operate at, which are less than 0.3.

2. The flow is assumed to be **inviscid**, which is reasonable for the domain outside the boundary layer. This means that vortex models do not model a viscous boundary layer and are thus unable to model effects such as skin friction drag or dynamic stall. Dynamic inflow, however, is inherently modelled through the unsteady formulation (as a changing near-wake doublet strength). Boundary layer models can be applied to panel methods by adding a displacement thickness and injection velocity. This assumption is also not applicable at the location of the wake, meaning that inter-panel interaction (when the wake comes into contact with itself or the body), needs to be accounted for.
3. The flow is assumed to be **irrotational**. This effect stems from the inviscid assumption, as local fluid rotation occurs due to viscous forces that provide a shear effect on the fluid. This assumption is again only valid away from the boundary layer and away from the wake.
4. The flow close to the panels themselves are governed by a **vortex core model**, meaning that the solution to the flow is sensitive to the type and parameters of the vortex core model used.

### Use of Panel Methods in Literature

The Wake Induced Dynamic Simulator (WInDS), produced by Sebastian and Lackner [43][44], is an open-source free-wake lifting line code that aims to investigate the wake aerodynamics of a floating off-shore wind turbine. It was validated extensively by Sebastian against Stereo Particle-Image Velocimetry (SPIV) measurements. The first validation was conducted against the Model Rotor Experiments under Controlled conditions (MEXICO) project, which used a 3-bladed rotor of blade length 4.5m. The second validation was conducted against a project at the Delft University of Technology, which used a 2-bladed rotor of blade length 2m [8] [9] [31]. The difference in tip vortex locations for both validations was under 7% [44]. These validations, however, were conducted on a fixed-base turbine, so a validation against a model FOWT was required. A model at the University of Malta was used for this validation, which was conducted by Sant [38] and Farrugia [11].

Upon this validation, a study on the performance of a baseline NREL 5MW FOWT (details in [20]) was conducted by Farrugia et al. [12], subject to realistic and extreme wave conditions. In this study, an uncoupled solution was produced wherein the surge motion of the platform was prescribed sinusoidally and the effects at the rotor investigated. The aerodynamic loading response amplitude was found to increase with tip speed ratio, and have a linear relationship with surge velocity amplitude. Operating conditions were also found to have an effect on the power production of the FOWT, relative to the power production of its fixed-base counterpart. Results from the simulation confirmed increasing mean FOWT power production (relative to its fixed-base counterpart) with increasing tip-speed ratio  $\lambda$ . The model further showed a relation between mean power production and thrust with surge frequency, although it depended on the operating condition. Above-rated  $\lambda$  conditions resulted in increasing power production with increasing frequency, while below-rated  $\lambda$  conditions resulted in decreasing power production. High tip speed ratios were suggested to explain the high aerodynamic torque and thrust fluctuations, due to the onset of blade-vortex interactions of adjacent blades.

Wen et al. [57] investigated the influence of platform surge motion on the NREL 5MW baseline wind turbine, mounted on the OC3 Hywind Spar-Buoy platform [18]. This study attempts to address what was identified as two shortcomings in previous literature: the lack of work done in a high range of tip-speed ratios and surge motions, and the lack of correlation between surge amplitude and frequency (which is physically present in wind-wave correlations). To address the latter, Wen et al. proposed a reduced frequency  $k = 2\pi f_s A_s / U_\infty$ , where  $2\pi f_s$  and  $A_s$  are the surge frequency and amplitude, respectively. They subsequently calculated the mean and variations in thrust and power coefficients, for a range of tip-speed ratios and reduced frequencies. Figure 1.20 and Figure 1.21 show the variations in power and thrust from changing the tip-speed ratio  $\lambda$  and reduced frequency  $k$ .

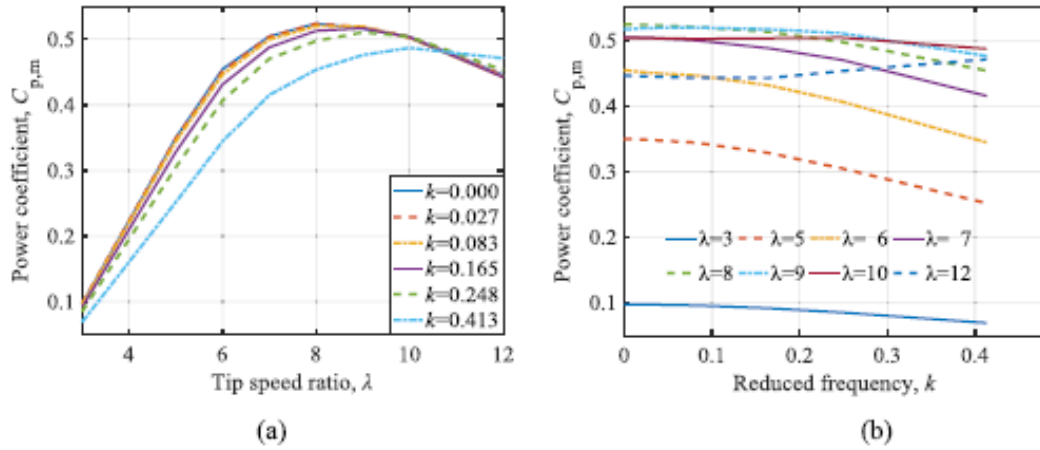


Figure 1.20: Mean power coefficient against (a) tip-speed ratio and (b) reduced frequency. Taken from [57].

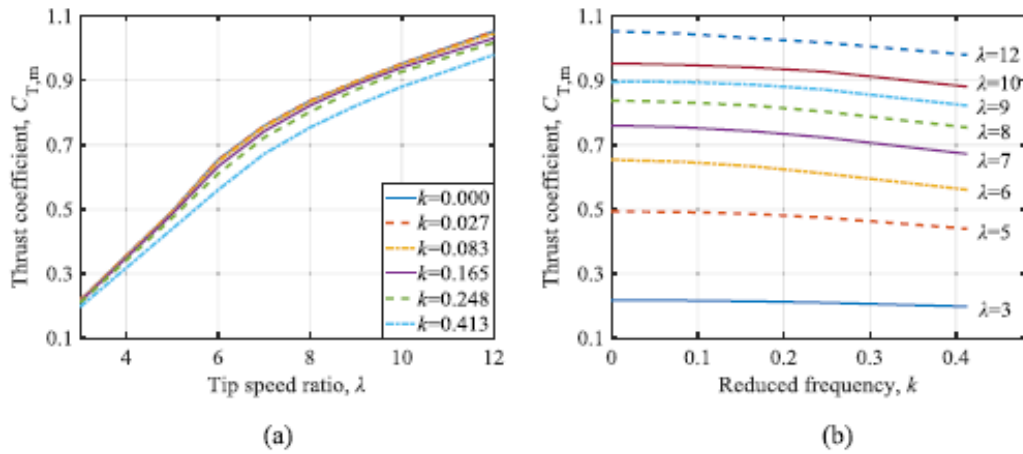


Figure 1.21: Mean thrust coefficient against (a) tip-speed ratio and (b) reduced frequency. Taken from [57].

Shen et al. [46] used an unsteady vortex lattice method with a free wake model for the unsteady aerodynamic performance analysis of a FOWT under platform surge motion. The unsteady aerodynamic performance, stability of the released vortex and the aerodynamic stability of the FOWT were studied in detail. They simulated the NREL 5MW turbine undergoing a surge amplitude of  $A_s = 8m$  and frequency of  $\omega_s = 0.5rad/s$  at rated conditions, which led to relative rotor velocities ranging between  $7.4m/s$  and  $15.4m/s$ . They showed that the turbine under surge conditions experienced an average thrust of 94.71% of its fixed-base counterpart, while extracting an average of 103.31% of the power. However, the oscillation of thrust and power varied according to Figure 1.22. While the average thrust of the turbine studied was predicted to be higher than its fixed-base counterpart, its amplitude and frequency would present a significant fatigue load on the major wind turbine components, and the associated fluctuating moment (see Figure 1.22d) would apply fatigue loads at the platform base.

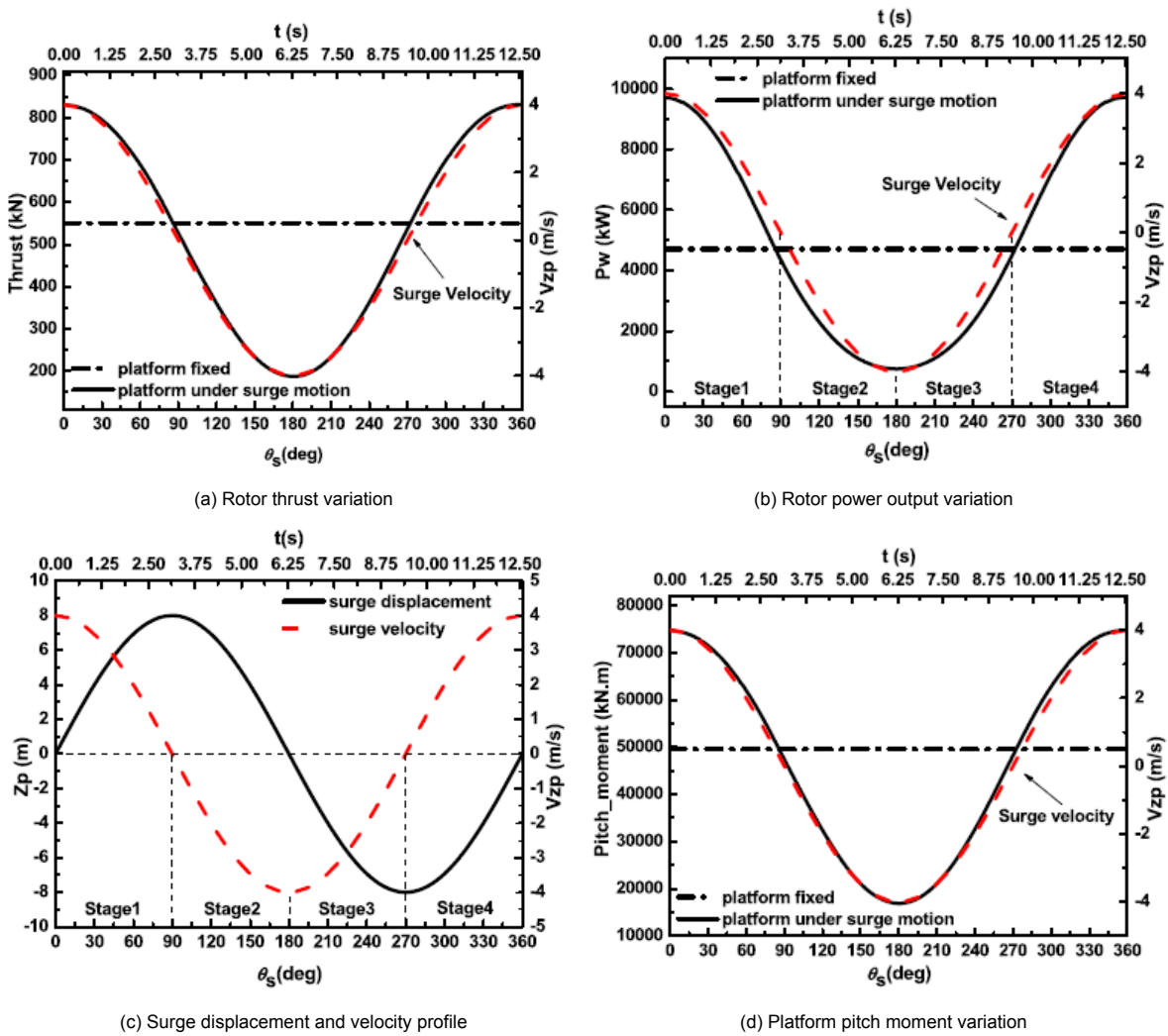


Figure 1.22: Rotor power, thrust and platform moment over time given surge displacement profile of NREL 5MW rotor [46]

The only literature found on using panel methods to model the behaviour of a FOWT at conditions with negative effective wind speed was a study on FOWT pitch motion from Jeon et al. [17]. This study featured a FOWT undergoing pitch ( $A_s = 3deg$  &  $\omega_s = 0.5rad/s$ ) in low wind speeds ( $U_\infty = 4.5m/s$ ) and at a high tip-speed ratio ( $\lambda = 11.1$ ). The turbine position is shown for reference in Figure 1.23. The induction factor contours (defined as the induced velocity divided by the inflow velocity) were produced, and showed that the highest induction factors were at position 3, as the rotor moved downwind. The highest thrust values were found, however, at position 7, as the rotor moved back upwind. Figure 1.24 shows the normal vorticity, and highlights a re-circulation region near the top of the blade during its upward motion. The authors attribute this to the high tip-speed ratio experienced at this moment, which reduces the convection rate of the wake.

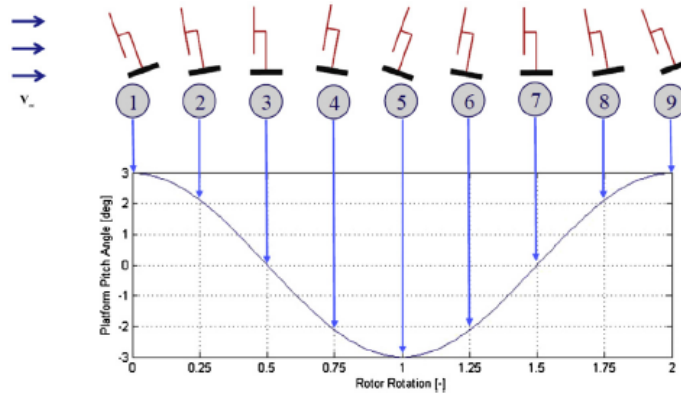


Figure 1.23: Rotor position throughout pitching motion. Taken from [17].

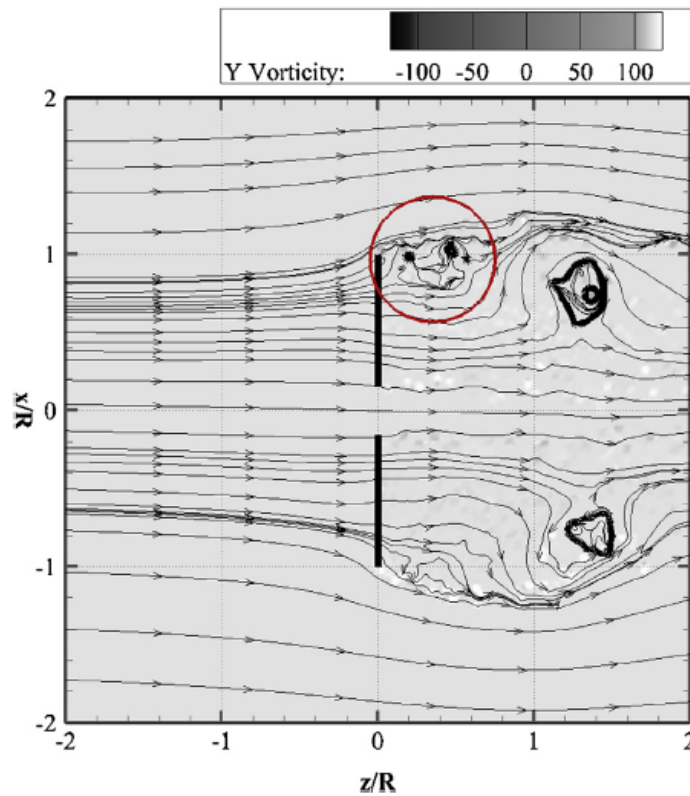


Figure 1.24: Normal vorticity fields and streamlines at location 7. Taken from [17]. Note that the orientation of the rotor is the same as the reference sketch in Figure 1.23

The conditions of FVM studies conducted on FOWT methods undergoing surge motion are summarized in Table 1.7. An overview of the studies performed with FVMs shows a lack of literature investigating the dynamic response of a FOWT undergoing negative effective wind speed. This inspired the first research question of this study, which is to perform these calculations, validating similar studies performed by CFD methods and to further analyze the resulting flow patterns.

Study	$A_s$ [m]	$\omega_s$ [rad/s]	$\lambda$	Lowest Effective Wind Speed $V_{eff}$ [m/s]
Micallef & Sant [32]	1.020	0.698	4,7,11	10.69
Farrugia et al. [12]	0.916	0.496	9.63	10.95
	1.348	0.471	7.00	10.77
	2.560	0.408	4.43	10.36
Wen et al. [57]	$k : 0.000 \rightarrow 0.413$	-	3 $\rightarrow$ 12	6.70
Shen et al. [46]	8	0.5	7.197	7.40

Table 1.7: Conditions of FVM studies on FOWT surge motion

### 1.3. Research Question, Aim/Objectives and Sub-Goals

The previous section provided a description of the extensive literature that exists with modelling FOWT systems undergoing platform motion, and the subset thereof on FOWT systems in unsteady conditions. These provided guidance to produce the research questions to be explored in this thesis.

#### 1.3.1. Research Question

Can the dynamic response of a FOWT in surge motion be estimated using a 3D panel method?

**Sub-questions:**

1. How well does a 3D panel method estimate the loading oscillations of a FOWT in low to moderate surge motion, compared with other numerical results?
2. For high-severity surge, how do the span-wise distributions of loading and circulation change over time?
3. For high-severity surge, what does the unsteady induction field over the domain suggest about the loading present on the blade?
4. For high-severity surge, can VRS be identified as an operating condition with an induction factor  $a \geq 1$ ?
5. For high-severity surge, can propeller state be quantitatively confirmed as an overall negative force acting on the rotor?

# 2

## Simulation Setup & Methodology

### 2.1. Simulation Set-up

This thesis work will be conducted in collaboration with the Energy Transition unit of TNO, under the guidance of the wind energy research group. While the work conducted is through a TNO-provided laptop machine, simulations will be run on an in-house high-performance computing cluster with the laptop machine acting as an interface.

Vortexje is an open-source 3D panel method created by Jorn Baayen [1], and will be the panel method used in this study. This code is intended to contrast with the other open-source panel method code, XFLR5 (cited in [1]), which tightly integrates the implementation and user interface. Vortexje features a C++ implementation which can be adapted for any user interface. It is based on a source-doublet formulation with a Dirichlet boundary condition. Surface velocities are computed following the method outlined by Marcov (cited in [1]), and blade-wake interaction effects are accounted for as suggested by Dixon [10]. The code features several test cases ready to simulate, including a Horizontal Axis Wind Turbine (HAWT). Modifications were performed earlier on the HAWT example such that it could take in as input an arbitrary mesh in Gmsh format, and perform the simulation. Separately, TNO has an in-house mesh generation tool written in FORTRAN, named *bladeMesh*, that creates blade meshes in Gmsh format given defined span-wise characteristics. Blade winglet capabilities are already incorporated into *bladeMesh*, through modification of the input files.

### 2.2. Methodology

The work in this thesis will consist of simulating FOWT systems undergoing platform surge motion. The simulations will be done through an open-source 3D panel method code called Vortexje. As this code is untested for FOWT applications, the first step will be to validate it for fixed-base HAWT conditions. The validation will begin with literature wherein the results of fixed-base HAWT simulations using panel methods are reported, along with experimental data. In doing so, the results of Vortexje will be compared with both panel methods to understand its differences from other panel methods, as well as with experimental data to determine its predictive capabilities. An overview of the test conditions can be found in Table 2.1.

Test	Free-stream Velocity $U_\infty$ [m/s]	Tip Speed Ratio $\lambda$ [-]
1	10.0	10.0
2 (Design Conditions)	14.7	6.7
3	24.1	4.2

Table 2.1: MEXICO Test Conditions

Afterwards, an analysis of loading and power oscillations will be done by use of the UNAFLOW test campaign. A background to the UNAFLOW rotor can be found in Appendix B. Three sets of test conditions were used, the first of which were also tested experimentally. These can be found in

Table 2.2. A constant-frequency and constant-amplitude set of tests were also run numerically with Aero-Module, and can be found in Table 2.3 and Table 2.4, respectively.

No.	Amplitude [m]	Frequency [Hz]
1	0.0000	0.0000
2	0.0350	1.0000
3	0.0080	2.0000
4	0.1250	0.1250

Table 2.2: UNAFLOW Cases - Experimental

No.	Amplitude [m]	Frequency [Hz]
1	0.0325	0.5000
2	0.0650	0.5000
3	0.1300	0.5000
4	0.2600	0.5000
5	0.5200	0.5000

Table 2.3: UNAFLOW Cases - Constant Frequency

No.	Amplitude [m]	Frequency [Hz]
1	0.1300	0.2500
2	0.1300	0.5000
3	0.1300	1.0000
4	0.1300	2.0000
5	0.1300	4.0000

Table 2.4: UNAFLOW Cases - Constant Amplitude

Afterwards, the research questions will be answered by simulating the NREL 5MW rotor under moderate to severe surge conditions. Details about the NREL 5MW rotor can be found in Appendix C. The effects of severe surge ( $v_{max}$  close to or above 1) will be explored. The simulation conditions repeat those of Kyle et al. [24], which are shown in Table 2.5. The effect of severe surge is investigated in case 'BS', where the low incoming velocity leads to the possibility of a velocity experienced by the rotor as less than the inflow velocity.

Label	Description	Reduced Surge Amplitude $A_s/D$ [-]	Reduced Frequency $k$ [-]	Reduced Maximum Surge Velocity $v_{max}$ [-]
RF	Rated, Fixed	0	0	0
RS	Rated, Surge	0.075	8.753	0.653
BF	Below-Rated, Fixed	0	0	0
BS	Below-Rated, Surge	0.075	14.004	1.045

Table 2.5: Load cases investigated by Kyle et al. [24]

### 2.3. Loading Calculation

Vortexje directly calculates and produces the following panel method outputs:

- A source strength  $\sigma_i$  for each body surface panel
- A doublet strength  $\mu_i$  for each body and wake surface panel
- A surface velocity vector  $\vec{v}_{surface,i}$  for each body surface panel
- A pressure coefficient  $C_{p,i}$  for each body surface panel

Given these output values, the following rotor-specific parameters can be obtained:

- **Pressure Coefficient Distributions** at a selected location along the span of the blade can be directly extracted from the pressure coefficient values. This assumes the calculated pressure acts at a point in the geometric center of the appropriate panel
- The **Axial and Tangential Force Distributions** can be calculated by converting the pressure coefficients values into pressure values, calculating the total panel force acting upon the geometric center of the panel at that location, and summing them in the axial and tangential directions at each span-wise location.

$$F'_{axial}(z) = \sum_i \delta F'_{i,axial} \quad (2.1)$$

$$F'_{tangential}(z) = \sum_i \delta F'_{i,tangential} \quad (2.2)$$

$$\delta \vec{F}'_i = \frac{\delta P_i A_i}{\delta r_i}; \quad \delta P_i = \frac{1}{2} C_p \rho v_{ref}^2 + p_{ref} \quad (2.3)$$

with  $d\vec{F}'_i$  the force per unit span,  $dP_i$  the pressure,  $A_i$  the area,  $\vec{n}_i$  the unit normal vector, and  $\delta r_i$  the span-wise length of the  $i^{th}$  panel

- The **Thrust**  $T$  and **Thrust Coefficient**  $C_T$  of the rotor can be calculated by integrating the axial force distribution along the span.

$$T = \sum_i F'_{i,axial} \delta r_i \quad C_T = \frac{T * N_{blades}}{0.5 \rho v_{ref}^2 \pi R^2} \quad (2.4)$$

- The **torque**  $Q$  and **power**  $P$ , along with their coefficients, can be calculated by integrating the tangential force distribution:

$$Q = \sum_i (F'_{i,tangential} \delta r_i) r_i \quad C_Q = \frac{Q}{0.5 \rho v_{ref}^2 \pi R^3} \quad (2.5)$$

$$P = Q \Omega N_{blades} \quad C_P = \frac{P}{0.5 \rho v_{ref}^3 \pi R^2} \quad (2.6)$$

- The **Circulation**  $\Gamma$  at a given time step can be calculated as the doublet strengths of the wake panels attached to the blade surface.
- The **Lift** (per unit span) distribution  $L'$  can be estimated through the circulation distribution, using the Kutta-Joukowski Theorem:

$$L' = \rho U_{ref} \Gamma \quad (2.7)$$

Where  $\rho$  and  $U_{ref}$  are the density and incoming velocity of the flow, respectively, as experienced by the blade. For the lift at a given span-wise location  $r$ , the incoming velocity of the flow can be calculated through the free-stream and the rotational components, respectively.

$$U_{ref} = \sqrt{(U_\infty(1-a))^2 + (\Omega r(1+a'))^2} \quad (2.8)$$

If the thrust coefficient were to be estimated through the lift coefficient, then the following relation would need to be used:

$$F'_{axial} = L' \cos \phi + D' \sin \phi \quad (2.9)$$

Where  $\phi$  is the inflow angle and  $D'$  is the drag per unit span. The thrust and thrust coefficient could then be calculated through Equation 2.4. Neither  $U_{ref}$  nor  $\phi$  are directly obtainable from Vortexje or a direct processing of its output, meaning it would need to be through other means. In section 2.4 are several methods to calculate that.

## 2.4. Velocity Field Calculation

While the above rotor parameters can be either directly obtained or calculated from the output that Vortexje produces, the angle of attack and axial induction factor depend on velocities away from the

domain of the blade and wake surfaces, and must therefore be calculated through the potential velocity field. Rahimi et al. [37] summarizes the methods in which the angle of attack and induction factor can be extracted from CFD results. These methods range in computational cost and fidelity, and three are listed below:

- With the **Inverse BEM Method**, the axial and tangential load distributions are used in an iterative process, similarly to the classic BEM formulation. This method thus doesn't require the calculation of velocity values away from the surface of the blade, instead using the force distributions to estimate the induction factors that exist. This method is the least computationally expensive, although it is limited by the one-dimensionality of momentum-based models. In highly three-dimensional flow, such as under flow separation and yawed conditions, the reliability of the inverse BEM is questionable [36][35]. This method would be unsuitable to validate BEM results using panel method techniques due to the theoretical cross-over, but that will not be explored in this thesis. Schneider et al. describe a variation of the algorithm as follows [41]:

1. Initialize the induction factors:  $a = 0$ ,  $a' = 0$
2. Calculate the inflow angle and inflow velocity:

$$\phi = \arctan \frac{(1-a)U_\infty}{(1+a')\Omega r} \quad (2.10)$$

$$W = \sqrt{((1-a)U_\infty)^2 + ((1+a')\Omega r)^2} \quad (2.11)$$

3. Calculate the normal and tangential force coefficients,  $C_n$  and  $C_t$  respectively:

$$C_n = \frac{F'_{axial}}{0.5\rho W^2 c} \quad (2.12)$$

$$C_t = \frac{F'_{tangential}}{0.5\rho W^2 c} \quad (2.13)$$

4. Calculate the axial and tangential induction factors,  $a$  and  $a'$  respectively, using the normal and tangential force coefficients:

$$a = \frac{1}{\frac{4F \sin^2 \phi}{\sigma C_n} + 1} \quad a' = \frac{1}{\frac{4F \sin \phi \cos \phi}{\sigma C_n} + 1} \quad (2.14)$$

Where  $F$  is the Prandtl correction factor, and  $\sigma$  is the blade solidity, defined by

$$\sigma = \frac{N_{blades} c}{2\pi r R} \quad (2.15)$$

The Glauert correction factor can be applied at this step; Hansen [15] offers the following correction for  $a > a_c = 0.2$ :

$$a = \frac{1}{2} \left[ 2 + K(1 - 2a_c) - \sqrt{(K(1 - 2a_c) + 2)^2 + 4(Ka_c^2 - 1)} \right] \quad (2.16)$$

$$K = \frac{4F \sin^2 \phi}{\sigma C_n} \quad (2.17)$$

5. Repeat steps 2 to 4 until the induction factors have converged within a pre-defined tolerance.
6. Calculate the angle of attack through the inflow angle and twist:

$$\alpha = \phi - \theta \quad (2.18)$$

7. Calculate the lift and drag coefficient through the inflow angle and the normal and tangential force coefficients:

$$C_l = C_n \cos \phi + C_t \sin \phi \quad (2.19)$$

$$C_d = C_n \sin \phi - C_t \cos \phi \quad (2.20)$$

- The **Azimuthally Averaged Technique (AAT)** is a method that estimates the average induction factor in an annulus through the velocity values at select points upstream and downstream of the rotor, at that annulus. Figure 2.1a shows an example schematic of this technique, where the blue and green dots are the upstream and downstream points, which are averaged independently. The induction factor is obtained by interpolating for the velocity at the rotor location. The angle of attack is then calculated directly from the interpolated axial velocity ( $f$ ) and tangential velocity:

$$\alpha = \tan^{-1} \left( \frac{V_{interp,axial}}{r\Omega(1+a')} \right) - \theta \quad (2.21)$$

Due to the fact that the values are sampled axially upstream and downstream of the rotor, this method is inapplicable to yawed flow. In addition, the induction factor is calculated as an azimuthal average, which differs from the local induction factor at the blade significantly, especially at the tip. Unlike the inverse BEM model, which corrects for this with the Prandtl finite blade correction factor, the AAT method does not account for this discrepancy. The high number of sampling points for this method (on the order of 100) also means this method can be very computationally expensive.

- The **3-Point method** introduced by Rahimi et al. [36] uses a similar system as the AAT, but removes the influence of bound circulation and upwash/downwash effects by averaging the velocity at three points on each side of the airfoil section (six total). This which drastically reduces the computational cost compared to the AAT method, and allows it to predict local effects at the tip, including 3-dimensional effects (e.g. yawed flow, dynamic effects). Figure 2.1b shows an example schematic, where the velocity is (similarly with the AAT) averaged for the upstream and downstream points separately, before interpolating at the rotor location. The angle of attack is found in the same way.

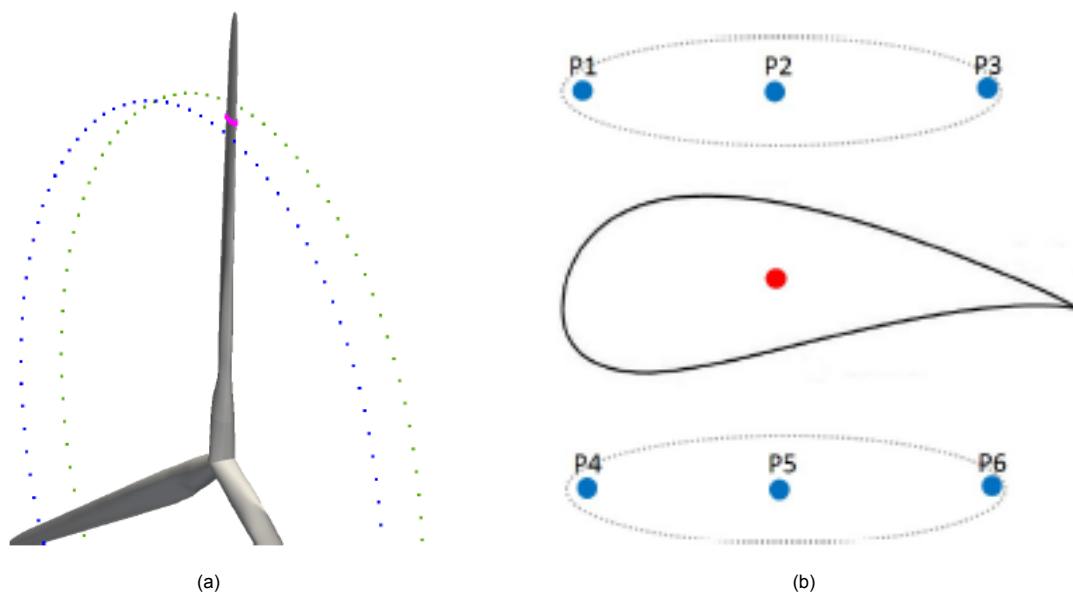


Figure 2.1: Sampling schematics of the (a) AAT and (b) 3-Point methods, which are used to estimate the angle of attack and induction factor at the rotor. Taken from [37].

## 2.5. Implementation of Surge Motion

To implement surge motion into a panel method such as Vortexje, two possible methods exist. The first consists of directly translating the points in space, giving rise to an experienced velocity from the point of view of the rotor. The second method consists of changing the free-stream velocity by the amount experienced at the rotor, effectively simulating the axial surge of the rotor. While theoretically these implementations should result in the same flow, there are differences in implementation that can lead

to a discrepancy in results. Four test cases were run to test the implementation of surge motion for a simpler geometry: a lifting surface with the characteristics shown in Table 2.6. In these test cases, the surface oscillated horizontally and vertically each with surge implemented as both direct displacement and dynamic inflow.

Geometric Properties	
Profile	NACA0012
Span	4.5 m
Number of span-wise nodes	21
Chord	1.0 m
Number of chord-wise nodes	64
Angle of attack	10.0 deg
Simulation conditions	
Free-stream velocity	4.0 m/s
Surge amplitude (horizontal)	0.25 m
Surge amplitude (vertical)	1.00 m
Surge frequency	0.5 Hz
Simulation time-step	0.01 s

Table 2.6: Geometric and simulation conditions of the surge-implemented lifting surface test cases

## 2.6. Investigation of Research Questions

The first question, which seeks to produce an understanding of the applicability of panel methods to surge motion, will be investigated through the simulation of two FOWT test cases. The first will investigate low-severity surge motion with the UNAFLOW case, for which other numerical and, for some conditions, experimental results exist. The focus of the study will be the ability of Vortexje to accurately capture the thrust coefficient mean and amplitude, given varying severity of surge. The severity of surge will be represented through  $v_{max}$ , the ratio between maximum rotor surge motion and free-stream velocity. The second test case will replicate the conditions of Kyle et al. [24], which simulates the thrust coefficient of the NREL 5MW reference turbine undergoing severe moderate and surge. The thrust coefficient will be compared with the CFD results given by Kyle et al. and potential rotor propeller mode will be identified a negative thrust coefficient over part of the surge period. The study will be expanded to loading and circulation distributions, and the possibility of VRS will also be discussed in the context of the loading and wake re-circulation.

# 3

## Results

### 3.1. Steady Validation: MEXICO Test Campaign

#### 3.1.1. Pressure Profiles

In this section, the experimental MEXICO pressure data is compared to the solution predicted by Vortexje for the tests at  $\lambda = 10.0$ , 6.7, and 4.2, respectively.

A further comparison to results predicted by ENSOLV, a high order finite volume CFD method that uses multi-block structured grids [22]. This method uses a fully turbulent boundary layer represented with a modified  $k - \omega$  turbulence model. The blade was represented with 164 radial cells and 128 cross-sectional cells. This tool was validated by Ten Pas (cited in [55]) with experimental MEXICO data, which is included in the following figures.

A comparison between inviscid panel methods is also done in this validation study, with panel method developed by Van Garrel [55], which makes use of a fast multilevel integral transform method. This method was also validated with experimental MEXICO data, and makes use of one fine blade (92 radial panels and 120 cross-sectional panels) and two coarser blades (46 radial panels and 30 cross-sectional panels).

#### 3.1.2. High Tip Speed Ratio

Figure 3.1 shows the pressure distributions along the span for  $\lambda = 10.0$  and  $U_\infty = 10.0$  m/s. The high tip-speed ratio implies lower inflow angles at the tip, and thus lower chances at boundary layer separation, even towards the root. Despite the high experimental errors for the 25% and 35% DU-91-W2-250 profiles, the suction profile predicted by ENSOLV suggests no such separation, and the results from each of the methods are in overall good agreement. While the suction side shows an over-prediction towards the leading edge, the shape conforms closer to the viscous ENSOLV solution than the multi-level panel method, which has a higher suction peak than the other two cases. The pressure side shows good agreement between all numerical methods, with much lower differences than for the suction side. With the exception of one experimental data point on the suction side, all methods are within experimental error.

The mid-span (60%) RISØ profile shows consistent over-prediction of the numerical methods compared to experimental data, with the viscous ENSOLV solution coming closest. Up until  $\sim 50\%$  of the chord, these differences are largely outside experimental error, although they still capture the shape of the profile and are in agreement with themselves. This can be attributed to the inability of the numerical solutions to capture the viscous effects of the boundary layer.

The outboard 82% and 92% profiles are in much better agreement, although the profile at 82% still has some differences in the suction side profiles towards the leading edge. Vortexje provides a better estimation than the multi-level panel method on the suction side towards the leading edge, although both methods over predict the suction-side pressure in the first 10% of the airfoil, measured from the leading edge. This over-prediction, which again stems from the boundary layer, has a significant effect on the axial and tangential force distributions, and thus ultimately the overall rotor power and thrust.

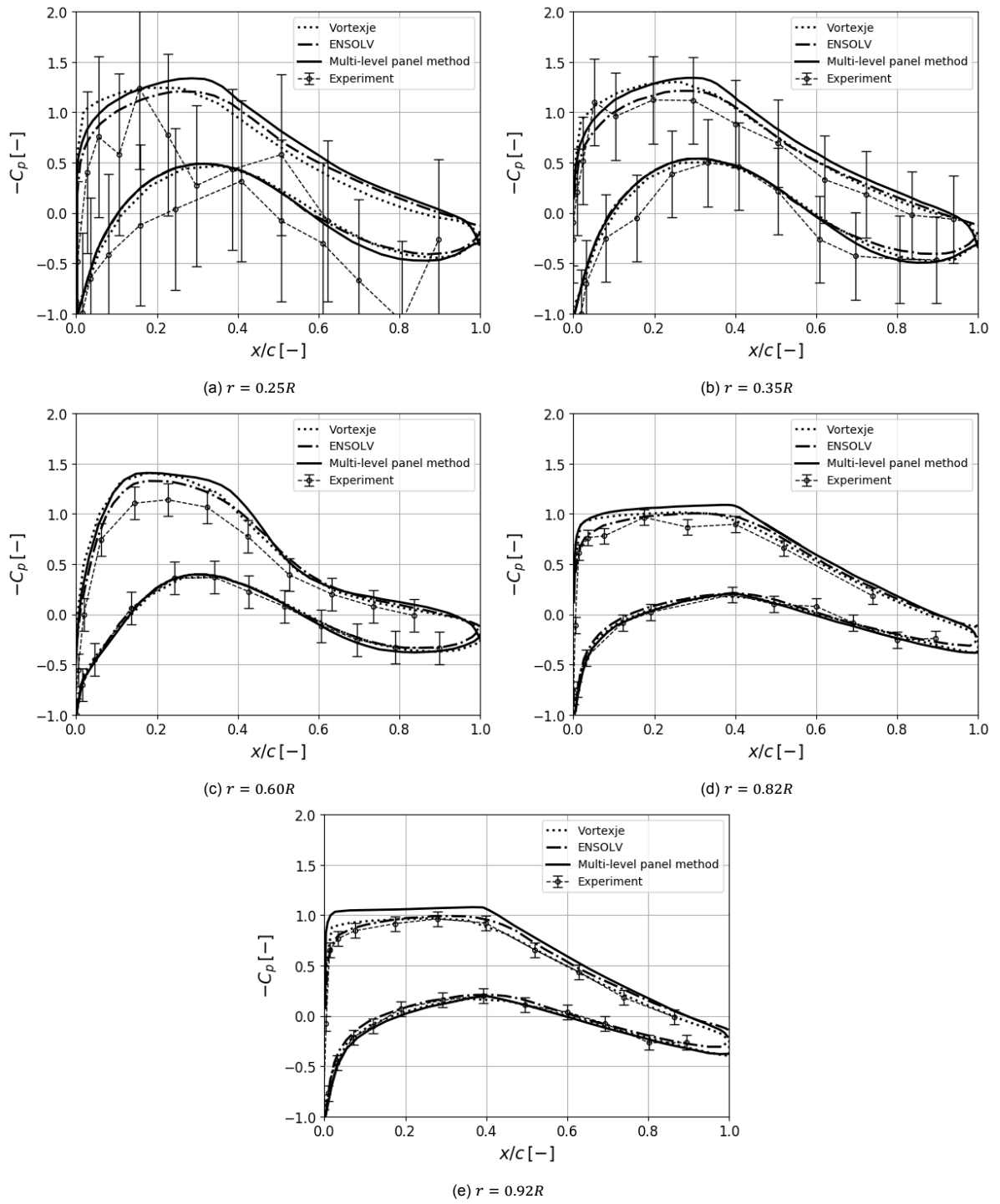


Figure 3.1: Experimentally and numerically obtained pressure coefficients of the MEXICO rotor in a free-stream velocity of  $10.0\text{ m/s}$  and tip speed ratio  $\lambda = 10.0$ . Taken from [55].

### 3.1.3. Design Tip Speed Ratio

Figure 3.2 shows the pressure contours along the span for  $\lambda = 6.7$  and  $U_\infty = 14.7$  m/s. Similar to the high tip-speed ratio case, the numerical methods consistently over-predict the suction-side results but show relatively good agreement for pressure-side results. These differences can again be attributed to the effects of the viscous boundary layer which the numerical methods are unable to capture. The pressure-side results again show far better agreement between solutions due to the lack of boundary layer effects.

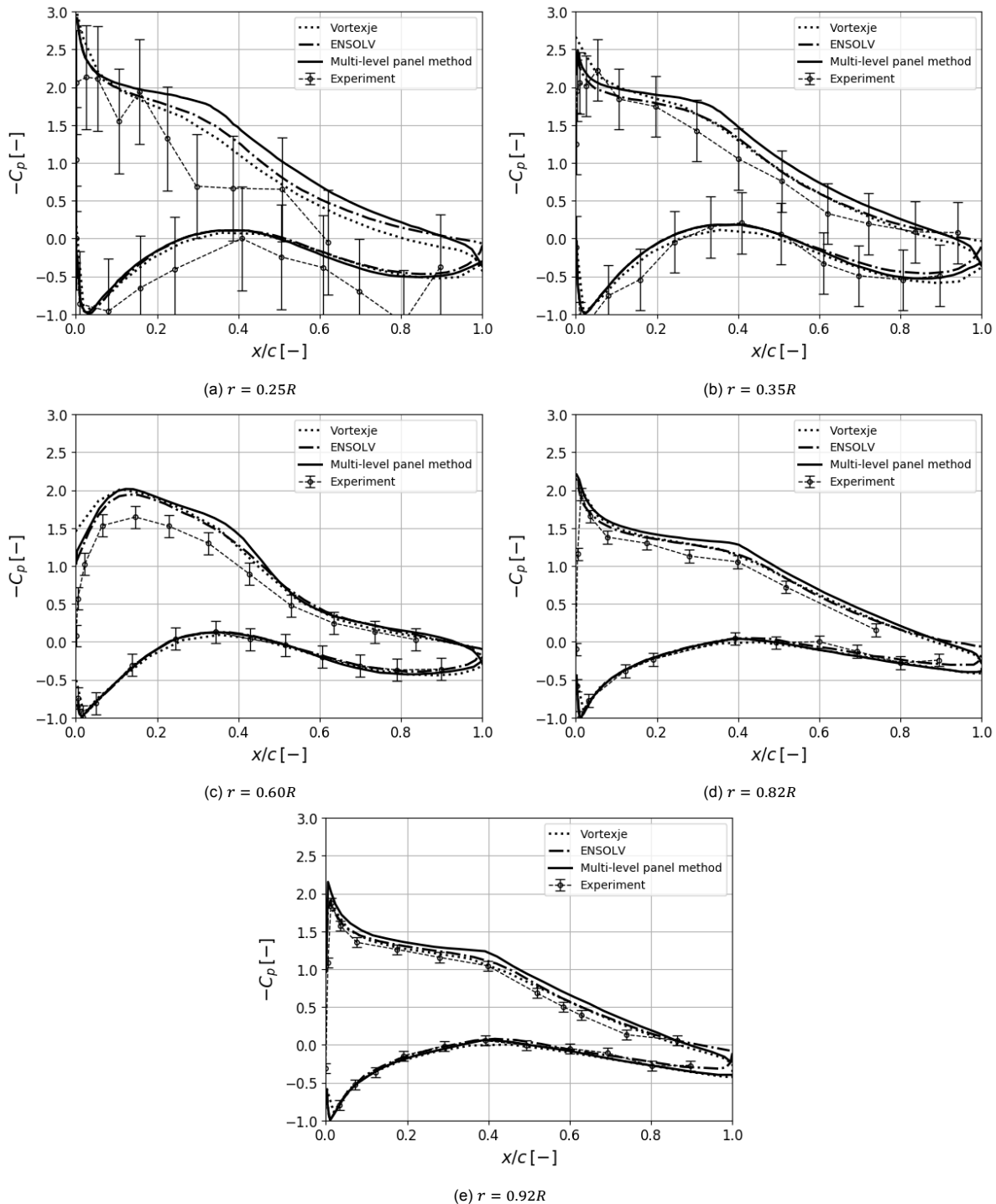


Figure 3.2: Experimentally and numerically obtained pressure coefficients of the MEXICO rotor in a free-stream velocity of 14.7 m/s and tip speed ratio  $\lambda = 6.7$ . Taken from [55].

### 3.1.4. Low Tip Speed Ratio

Figure 3.3 shows the pressure contours along the span for  $\lambda = 4.2$  and  $U_\infty = 24.1$  m/s. The relatively low tip speed ratio led to a high inflow angle, which induces boundary layer separation on the inboard part of the span. This separation is visible as a sudden drop in pressure at 30% of the chord, followed by an immediate low-pressure region until the trailing edge, and is not captured by either of the panel methods.

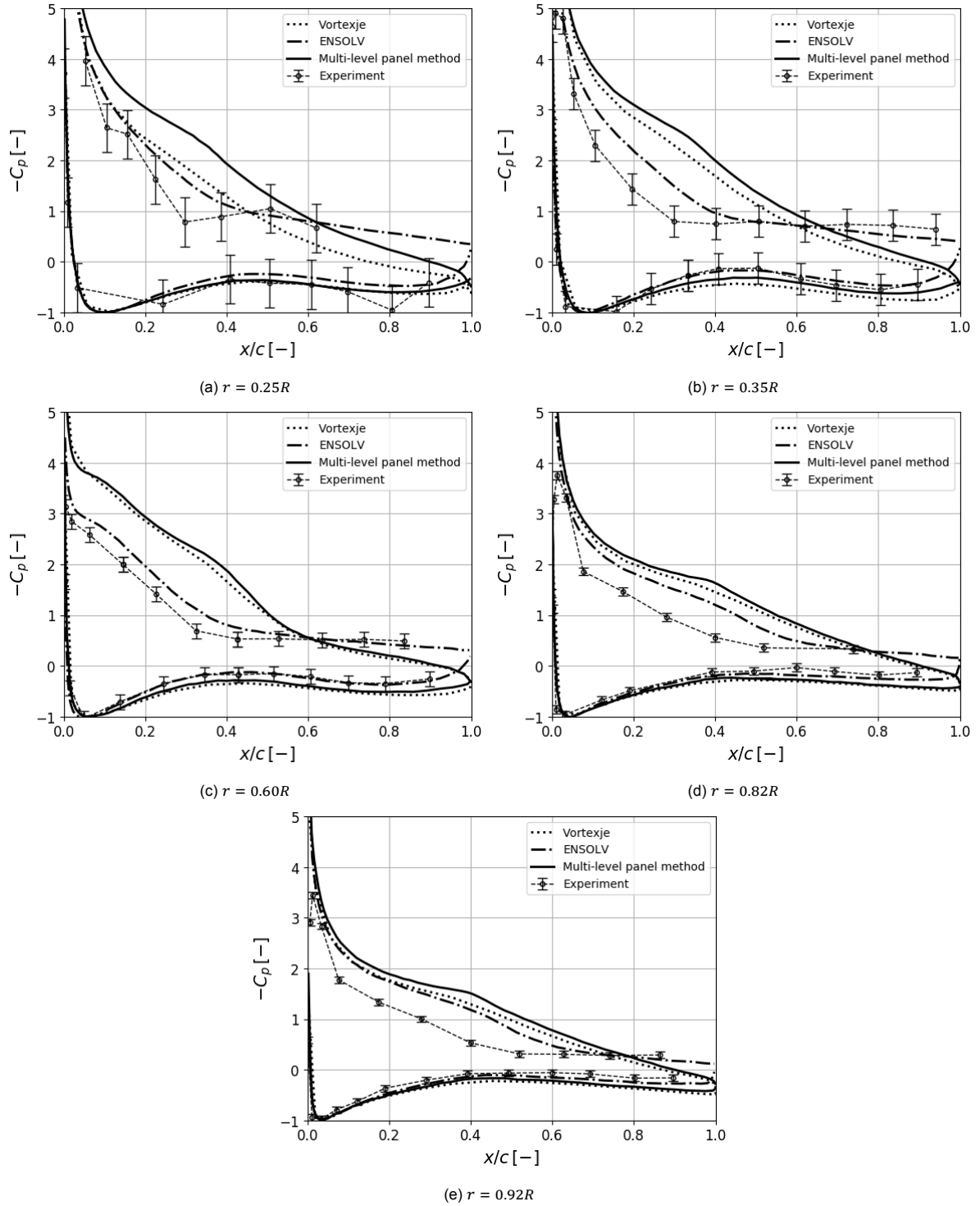


Figure 3.3: Experimentally and numerically obtained pressure coefficients of the MEXICO rotor in a free-stream velocity of 24.1 m/s and tip speed ratio  $\lambda = 4.2$ . Taken from [55].

### 3.2. Test Case: Lifting Surface Oscillation

To test the difference in surge implementations, a lifting surface was simulated moving in horizontal and vertical surge motion. The conditions of the tests are given in Table 2.6. The results of the horizontal displacement test case is shown in Figure 3.4 at  $t = 2.00s$  (1 revolution). The most significant difference between the two cases is in the non-physical flow behaviour resulting from the surface being directly displaced, shown in Figure 3.4. In contrast, the surface that experiences equivalent dynamic inflow has no such disturbances, suggesting a more physical flow solution. The effect of the discrepancy would also be seen in the pressure coefficient solution of the surface itself, ultimately resulting in a difference in predicted loading. This can already be seen in the strengths of the wakes; along time, the directly displaced solution features a lower variation in bound circulation. This is seen in the time-varying doublet strengths of the wake in Figure 3.4b, where the strength changes oscillates to lower values compared to when the surface experiences dynamic inflow.

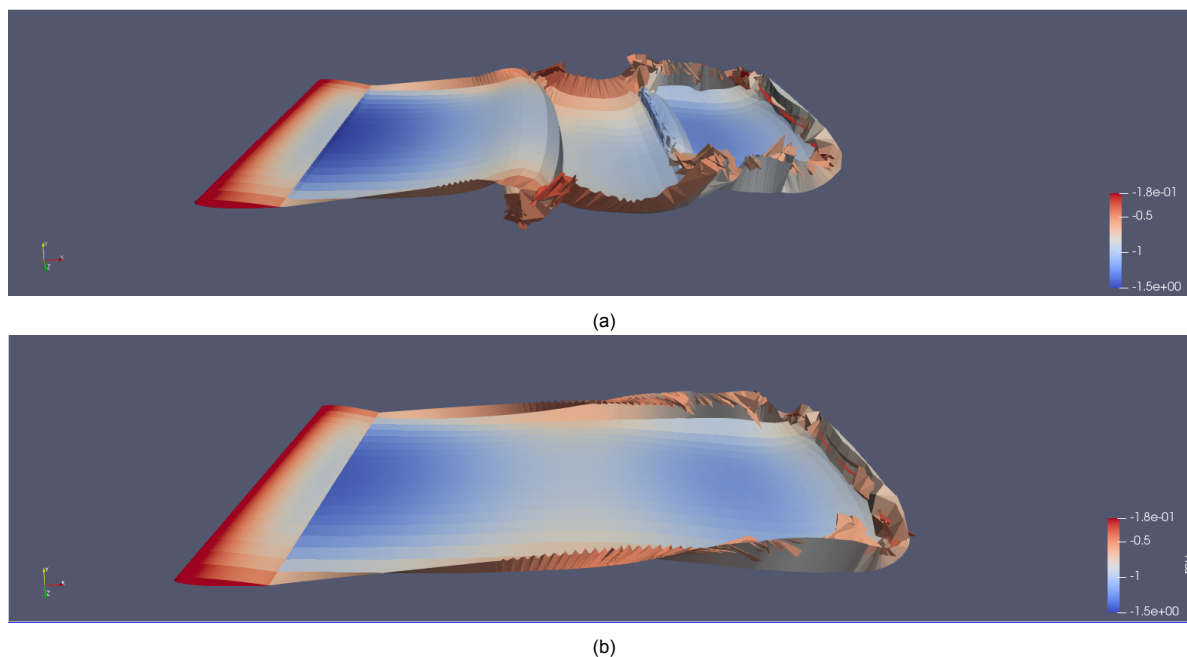


Figure 3.4: Wake characteristics of a lifting surface with horizontal surge motion imposed through (a) direct displacement and (b) dynamic inflow conditions

The disturbances in the wake occur at the apex of the surge motion, both at the maximum upstream and downstream positions. The first disturbance, which happens at the maximum upstream position of the body, is analyzed in further detail in Figure 3.5. This sequence of figures illustrates the mechanism with which the wake is emitted from the lifting surface shortly after it reaches the maximum upstream location ( $t = 0.50s$ ), when the surface begins to move in the same direction as the wind. The figures show how the angle between the trailing edge wake panels and the airfoil chord change drastically, performing a non-physical oscillation at the maximum upstream, with a similar opposite oscillation at the maximum downstream location. This can be attributed to the particular method in which Vortexje locates the attached wake panel at every time step. Vortexje calculates the apparent velocity of the surface in question (taking into account the free-stream velocity), projects it onto the bisector of the trailing edge angle, unless specified otherwise, and multiplies that by the time-step and a multiplicative factor (0.25 by default). It follows that this approach, while able to handle the steady rotation of a fixed-base rotor, is less robust for surface in oscillatory motion.

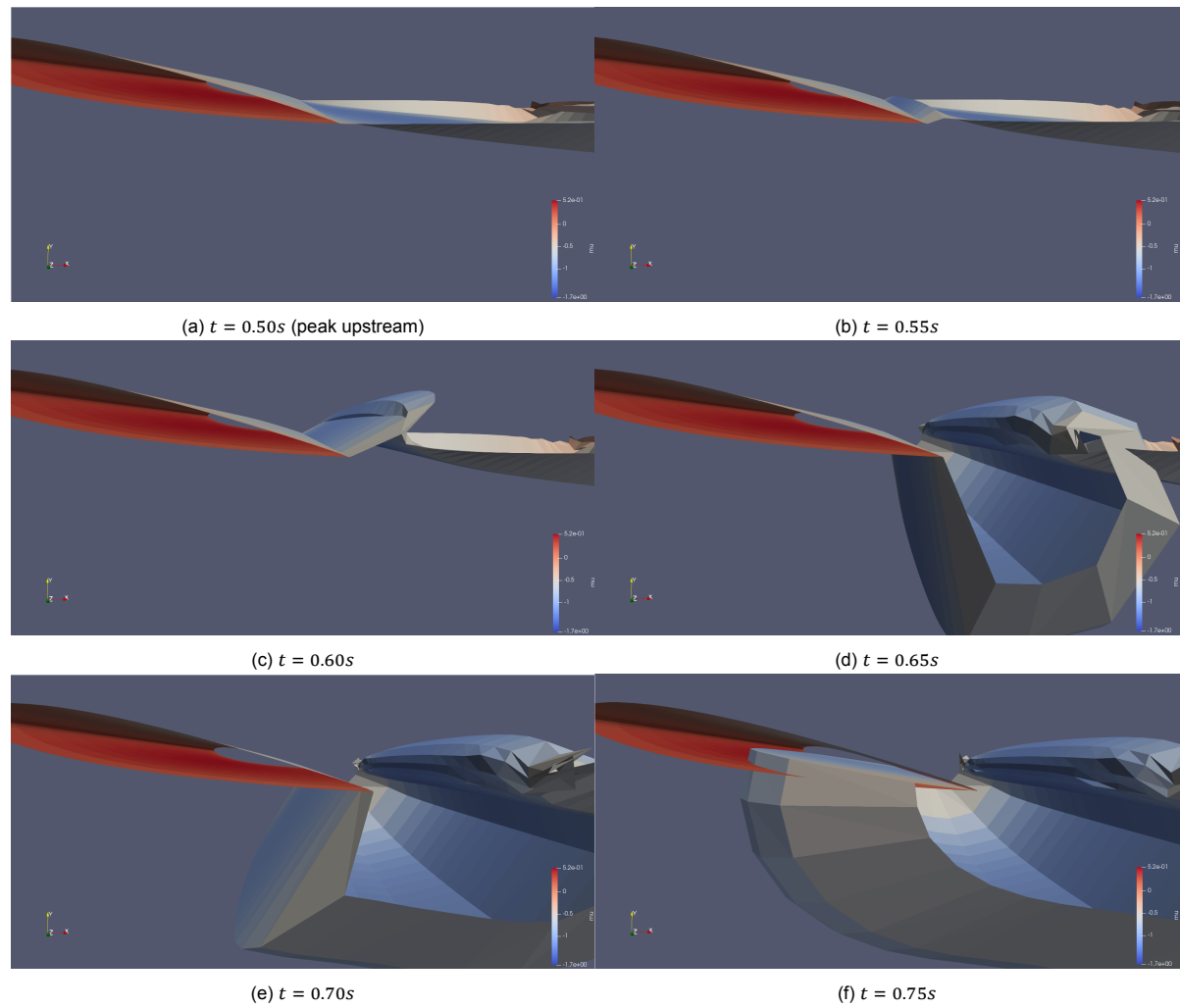


Figure 3.5: Wake disturbance generation at the maximum upstream position of a lifting surface with horizontal surge motion imposed

The results of the vertical displacement test case, which more accurately represents the motion experienced by a FOWT rotor blade, is shown in Figure 3.6 at  $t = 2.75s$  (shortly after 1 revolution). Similar to the horizontal test case, the loading changes are far more extreme when the surface experienced dynamic inflow, showed by the higher wake panel doublet strengths. Upon further investigation with FOWT simulations, it will be seen whether this effect is replicated for these two surge implementation types. There will also be an investigation into the ability of both these techniques in simulating actual FOWT motion. For the low-surge test case, using the UNAFLOW rotor, the dynamic inflow method will be used due to its lack of non-physical wake panel placement.

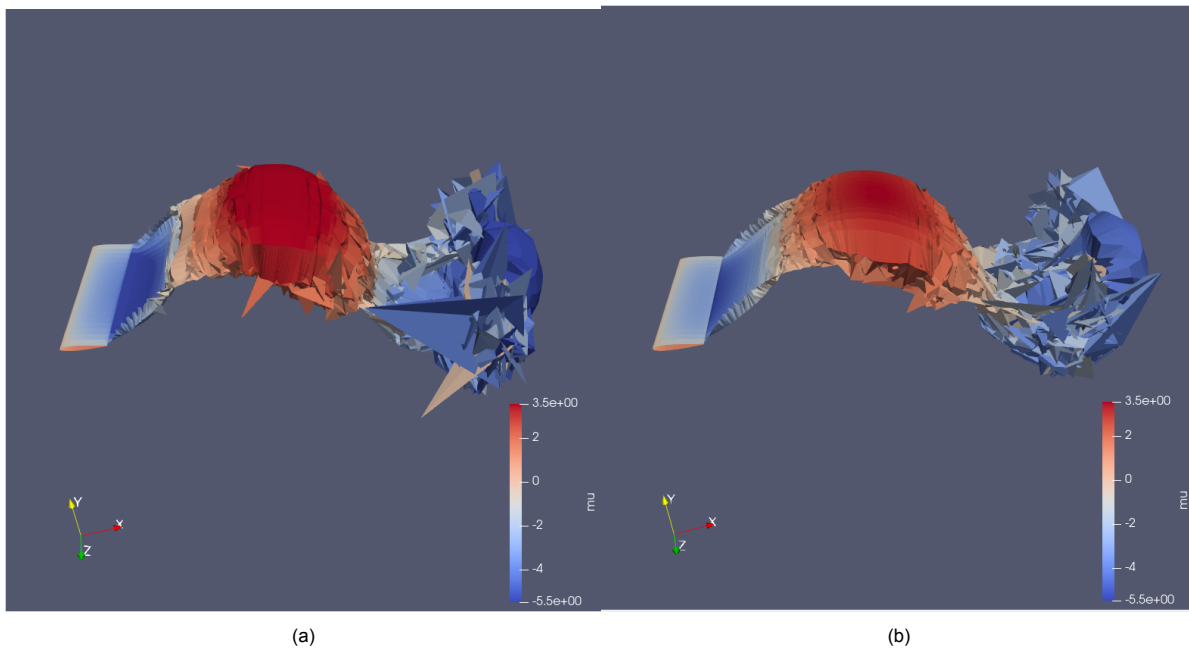


Figure 3.6: Wake characteristics of a lifting surface with vertical surge motion imposed through (a) direct displacement and (b) dynamic inflow conditions

### 3.3. Test Case: UNAFLOW

To verify the fixed-base dynamics of the UNAFLOW rotor, a comparison was done between Vortexje and existing numerical solutions (BEM, Lifting-line (AWSM), CFD). This corresponds to case No. 0 in Table 2.2, and the loading distributions are shown in Figure 3.7. It can be seen that while the axial force is reproduced by Vortexje with reasonably high agreement, the tangential forces are over-predicted by Vortexje. This is likely due to the fact that the inviscid nature of Vortexje leads to a lack of viscous drag modelling, which results in undamped (and thus higher) tangential forces.

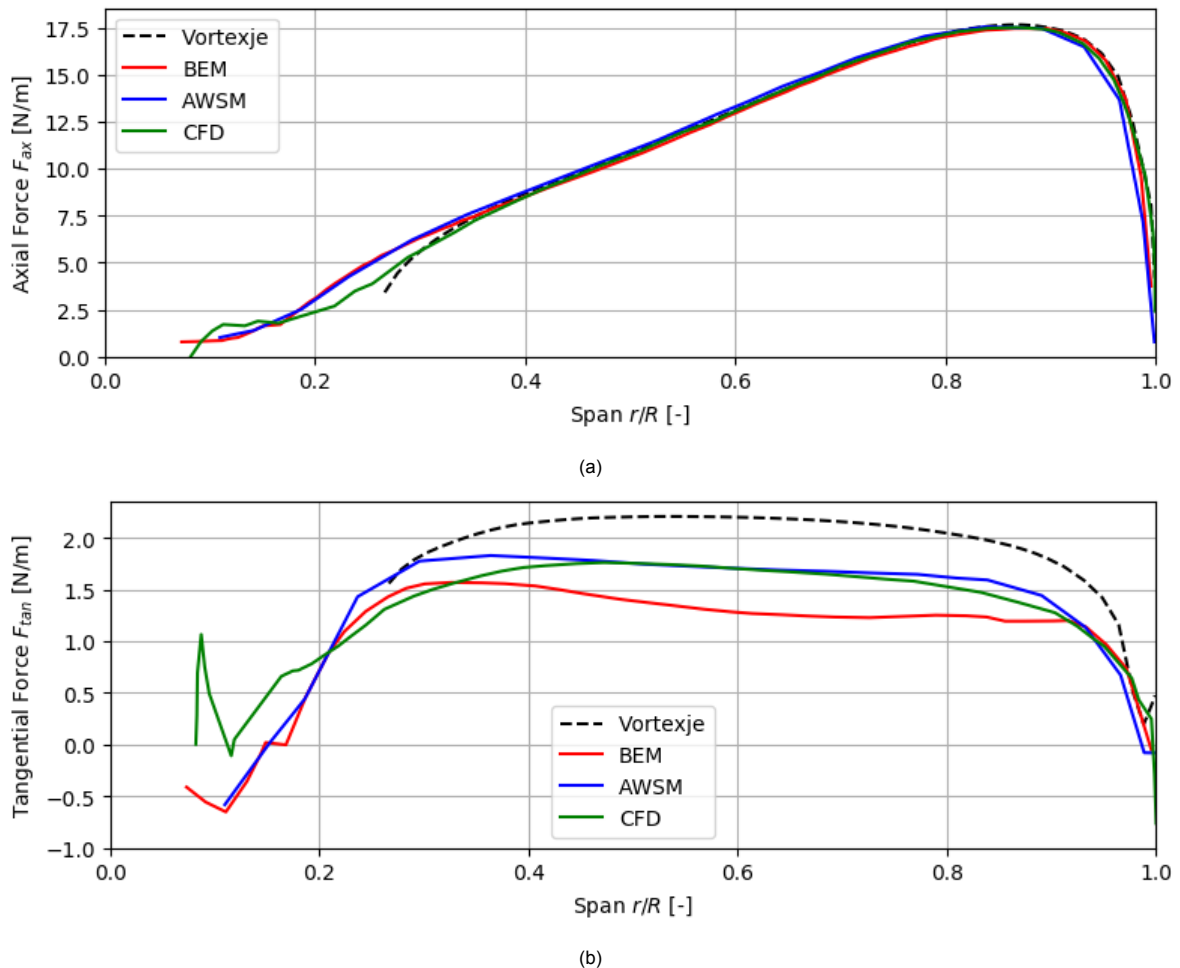


Figure 3.7: Numerical (a) axial and (b) tangential force distributions of the steady UNAFLOW experiment, as calculated by Aero-Module (BEM & AWSM), FLOWer, and Vortexje

#### 3.3.1. Experimental Results

Surge conditions for further simulations run for the UNAFLOW campaign were replicated by Vortexje. Figure 3.8 shows the spread of conditions that were run - the vertical set of points referring to the constant frequency cases and the horizontal set of points referring to the constant amplitude cases. The remaining points were those explored experimentally. The Vortexje cases were run through modifying dynamic inflow, as this was judged (as shown in the previous section) to be less prone to numerical errors induced by the wake panel placement.

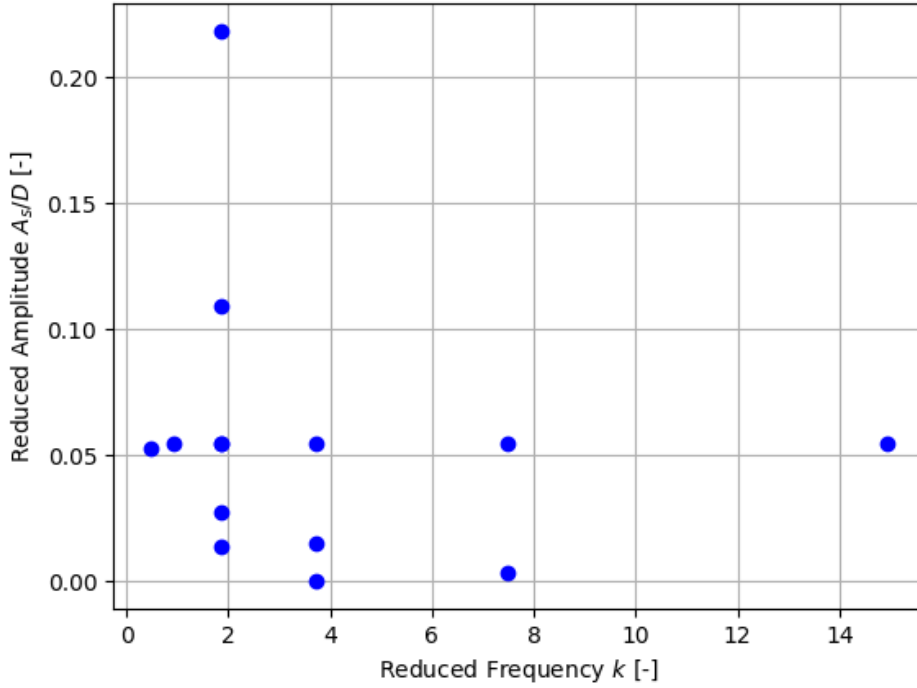
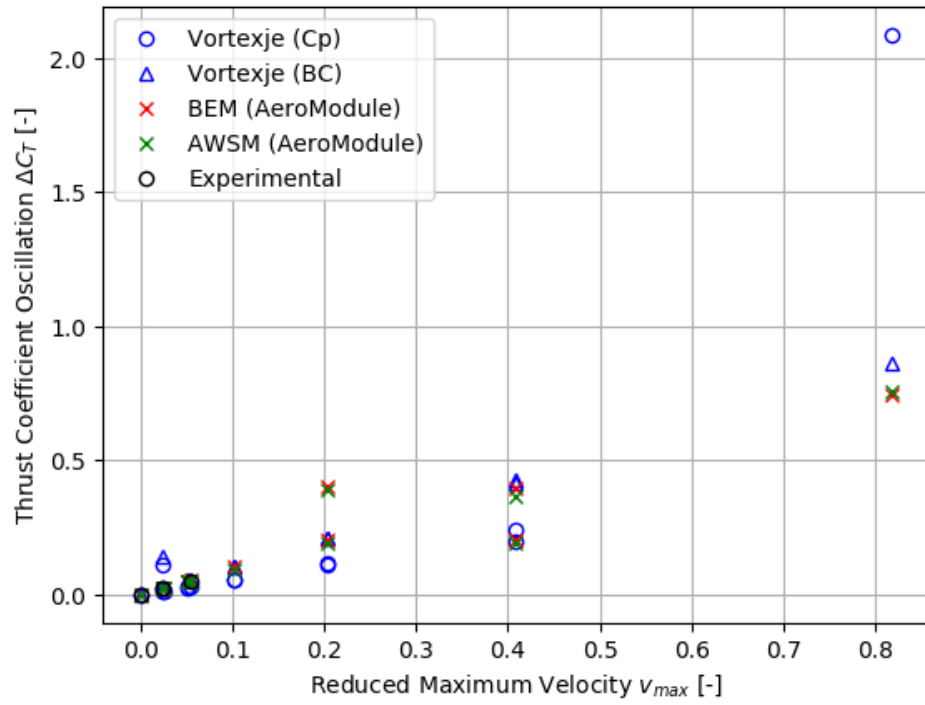
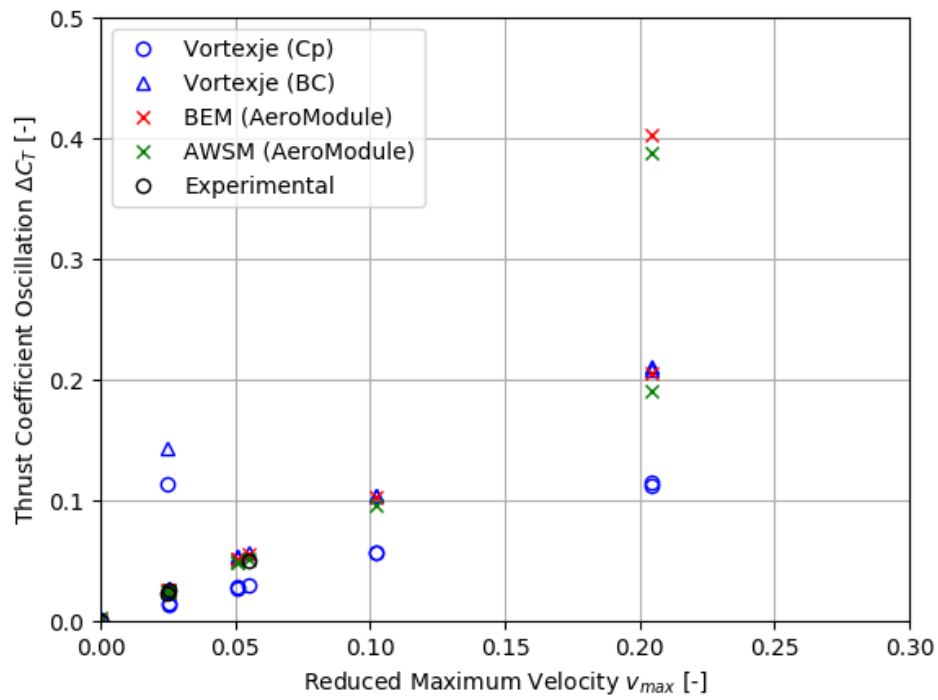


Figure 3.8: Reduced amplitude  $\frac{A_s}{D}$  against reduced frequency  $k$

To estimate the thrust coefficient of the FOWT, two methods were explored. The first was through the integration of the panel pressures as described in section 2.3, and the second was estimated through the bound circulation. These are denoted in Figure 3.9 and Figure 3.11 as *Vortexje (Cp)* and *Vortexje (BC)*, respectively. The second estimated the thrust coefficient as  $F'_{axial} \approx L' \approx \rho \sqrt{(U_\infty)^2 + (\Omega r)^2} \Gamma$ . The approximation of  $U_{ref} \approx \sqrt{(U_\infty)^2 + (\Omega r)^2}$  assumes that the incoming velocity is constant, which is not the case in surge motion. Additionally, the incoming velocity is not reduced by the induction factor. In total, however, the error introduced by this assumption is small (< 5% for all cases), as the rotational component of the velocity greatly outweighs the free-stream component. The approximation of  $F'_{axial} = L' \cos \phi + D' \sin \phi \approx L'$  neglects the effects of drag, which would result in an underestimated thrust, and the effect of inflow angle, which would lead to an overestimated thrust. These errors both reduce with inflow angle, so the error would be dependent on them. This therefore does not give a direct calculation of thrust, but is investigated in this case to compare numerical stability.

Figure 3.9a shows the effect of surge severity, represented by the reduced maximum surge velocity  $v_{max}$ , on the thrust oscillations. For each method of estimating thrust, the trend of increasing amplitude is shown to hold for increasing severity, although integrating the panel pressure coefficients is shown to result in a consistently lower amplitude, most recognizably with  $v_{max} < 0.3$  (Figure 3.9b). However, the lift coefficient provides amplitudes in better agreement with the thrust coefficients predicted by both other numerical results, as well as experimental results. A comparison can be made with Figure 3.10 from Ferreira et al. [13], which shows an approximately linear relationship with an approximate slope of unity, given the same quantities, for a range of numerical and experimental studies. The values predicted by AeroModule BEM, AWSM, and Vortexje through the bound circulation, are in agreement with this trend found in literature. For higher surge, where significant blade-wake interaction is to be expected, the trends differ significantly. For  $v_{max} \approx 0.8$ , where some level of blade-wake interaction is to be expected, the amplitude predicted by pressure coefficient integration is drastically overestimated. This will be explored more in depth in the next section, but the lift coefficient is still in reasonable agreement, suggesting that this method of estimating thrust is more robust.

(a)  $v_{max} < 0.8$ (b)  $v_{max} < 0.3$ Figure 3.9: Thrust coefficient amplitude  $\Delta C_T$  against reduced maximum surge velocity  $v_{max}$

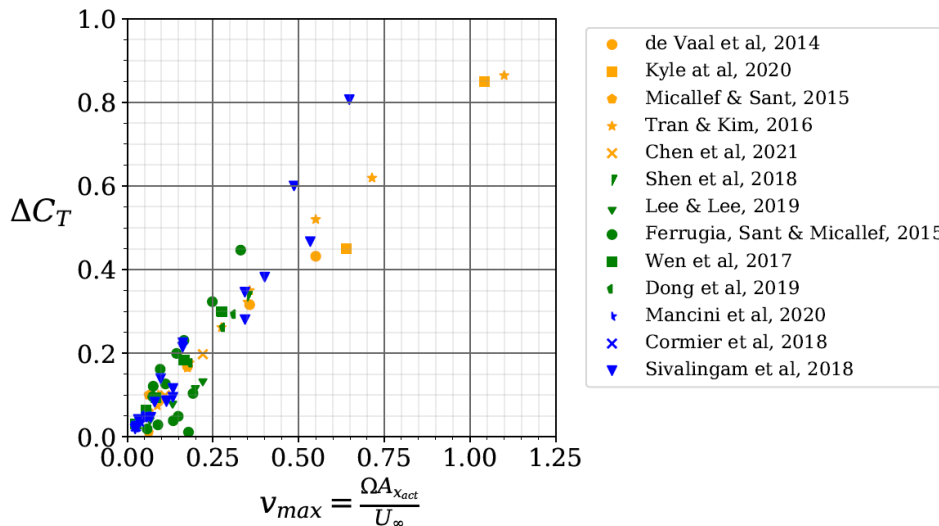


Figure 3.10: Review of thrust coefficient amplitude  $\Delta C_T$  (from literature) against reduced maximum surge velocity  $v_{max}$ . Taken from [13].

Figure 3.11 shows the calculated mean thrust coefficient values against their predicted amplitudes. The mean value of the thrust for each method (inviscid 3D panel, BEM, AWSM) differs for low-severity surge from the experimental results by a small but consistent amount, with AWSM having the best agreement, followed by BEM and Vortexje. However, the results still show reasonable agreement. For higher-severity surge, the mean thrust varies much more significantly, with the high-severity surge case under-estimating the mean thrust coefficient by about 50%. The demarcation line separates the conditions under which rotor propeller state may occur, with values above the line indicating thrusts reaching a negative value at some point in the surge cycle. In this case, high-severity surge is shown to be the case in which the thrust may, depending on the prediction method used, reach negative values- indicating that the propeller may operate briefly as a propeller.

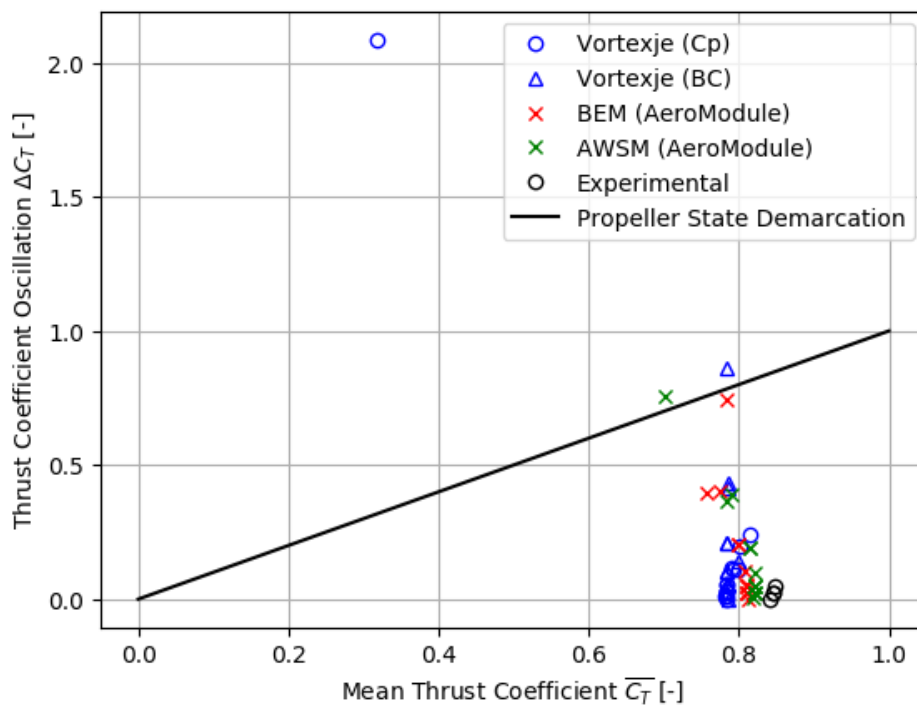


Figure 3.11: Thrust coefficient amplitude  $\Delta C_T$  against mean thrust coefficient  $k$

### 3.4. Analysis: Severe Surge with the NREL 5MW Reference Turbine

To investigate the effects of severe surge, as predicted by the inviscid Vortexje solution, span-wise distributions will be compared at the points indicated in Figure 3.12. For the simulations run, point 1 refers to a rotor state at its maximum displacement upstream. The rotor downwind to its equilibrium position (pt. 2), before continuing onwards to its point of maximum downwind displacement (pt. 3) and back to its equilibrium (pt. 4). Thus, its motion from point 1 to point 2 increasingly condenses the wake as the rotor's velocity increases and is pointed in the direction of the wake convection. To investigate the ability of this panel method in capturing the power and thrust fluctuations induced by high-severity surge, two levels of severity (modified by changing the wind speed) will be investigated, as per Table 2.5. The surge motion will be implemented both through dynamic inflow, and through direct displacement.

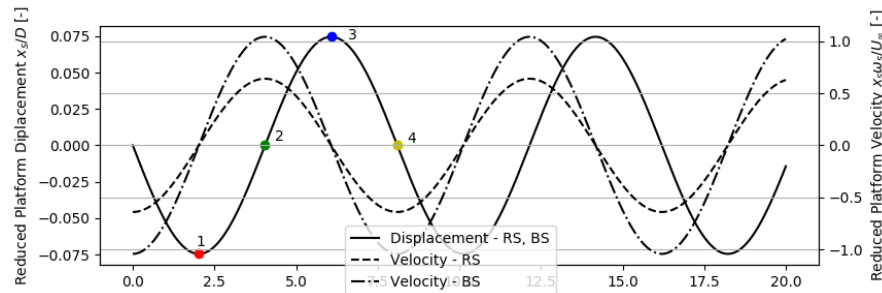


Figure 3.12: Surge displacement and velocity conditions for moderate and severe surge, according to Kyle et al. [24].

#### 3.4.1. Surge through Dynamic Inflow

##### Loading Distributions

Figure 3.13 shows the axial force distributions given moderate and severe surge, as estimated through the integration of the panel pressure coefficients. The point at which the helical wake sheets are closest to each other, as well as to the rotor, is when the rotor's downwind velocity is highest, which is at point 2 (green) of the motion. The observed effect for rated conditions and below-rated conditions is similar; the axial force increases in the tip region and decreases, becoming significantly negative, for the inboard region. This behaviour resembles what was found with Kyle et al. [24], wherein it was predicted that from an airfoil perspective, a low relative velocity would lead to low or negative angles of attack, and subsequently low thrust (which is roughly proportional to lift at low angles of attack). Given that the effect increases at higher pitch values, this effect is expected to be more pronounced in the inboard region, which was in Figure 3.13. However, the effect should be present in some capacity along the entire blade. Contrary to this expectation, the axial force surpasses the equilibrium values in the outboard part of the blade, giving rise to overall positive rotor thrust. This highlights an error in the ability of Vortexje, in its current state, to capture the thrust oscillations present in high-severity surge motion. The combination of the highly negative inboard and (non-physically) highly positive outboard axial force leads to non-sinusoidal behaviour of the total thrust coefficient, as seen in Figure 3.14. This is in contrast to CFD results from Kyle et al., which shows mostly sinusoidal behaviour of the thrust coefficient over time, as theoretically expected. The CFD results indicate unsteady behaviour of the flow at  $t \approx 16s$ , a result of a high inflow angle leading to separated flow. This is not expected to be captured by Vortexje, as this is largely a viscous effect that can't be modelled through inviscid techniques.

For the less extreme surge case of  $v_{max} = 0.653$ , the behaviour is better bounded, with the minimum reaching close to the value predicted by CFD. However, the results of the high-severity surge case,  $v_{max} = 1.045$ , indicate that the effect of the wake as the rotor moves downwind lead to numerical instabilities (the thrust coefficient moves to negative infinity). Conversely, as the rotor moves upwind, it experiences a high incoming velocity and the expectation is that it would experience a high thrust (confirmed with CFD). However, this part of the motion is also inaccurately estimated by Vortexje, with a predicted drop in thrust where one would predict an increase. While this may be an inability of the code to properly model blade-wake interaction, the circulation behaves closer to the expected sinusoidal fashion, meaning that the problem may lie either in the way that Vortexje calculates the

pressure coefficient, or in the post-processing of the pressure coefficient values.

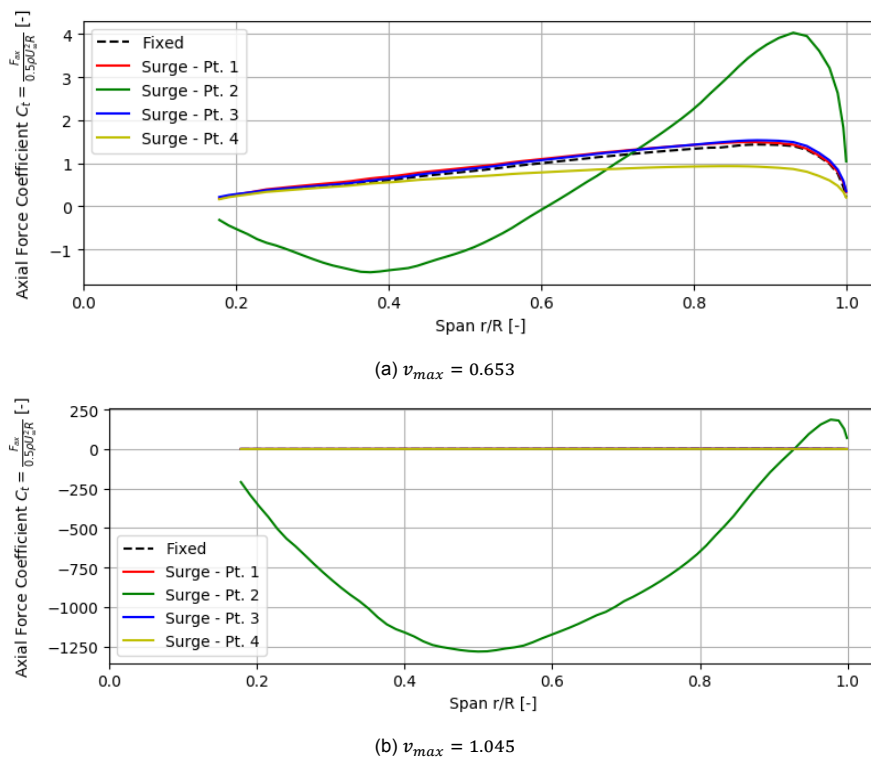


Figure 3.13: Axial loading distribution for (a) moderate and (b) severe surge conditions

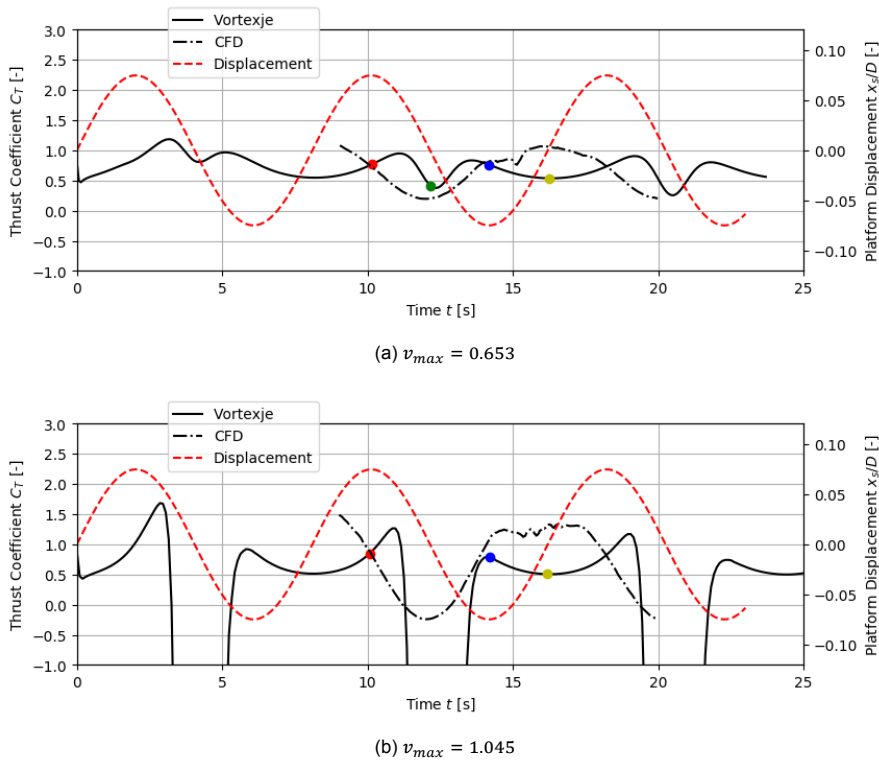


Figure 3.14: Thrust coefficient for (a) moderate and (b) severe surge conditions

The distributions shown in Figure 3.15 indicate similar numerical instability in the calculation of tangential loading. These then translate to instabilities in the power coefficient (Figure 3.16), where values reach extremely low and high values over the course of the cycle. Similar to the thrust coefficient, the solution exhibits maximum instability as the rotor moves downwind and experiences low incoming velocities. Despite the lack of CFD values to compare to, it is expected that the pressure coefficient as the rotor moves upwind are still inaccurate.

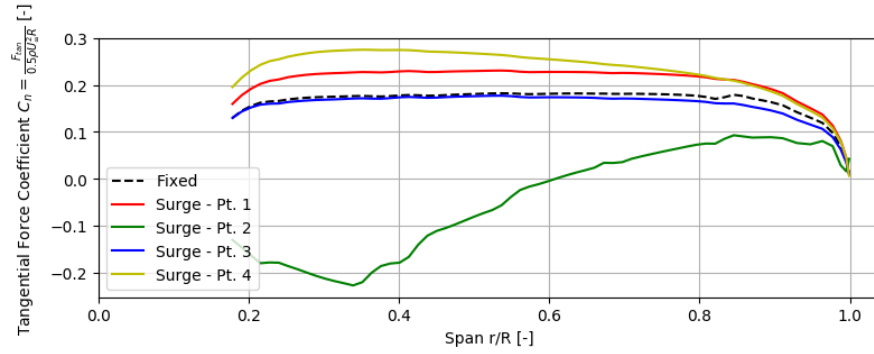
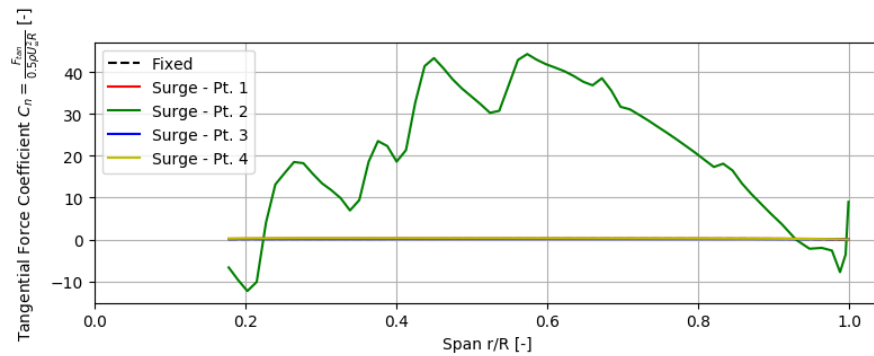
(a)  $v_{max} = 0.653$ (b)  $v_{max} = 1.045$ 

Figure 3.15: Tangential loading distribution for (a) moderate and (b) severe surge conditions

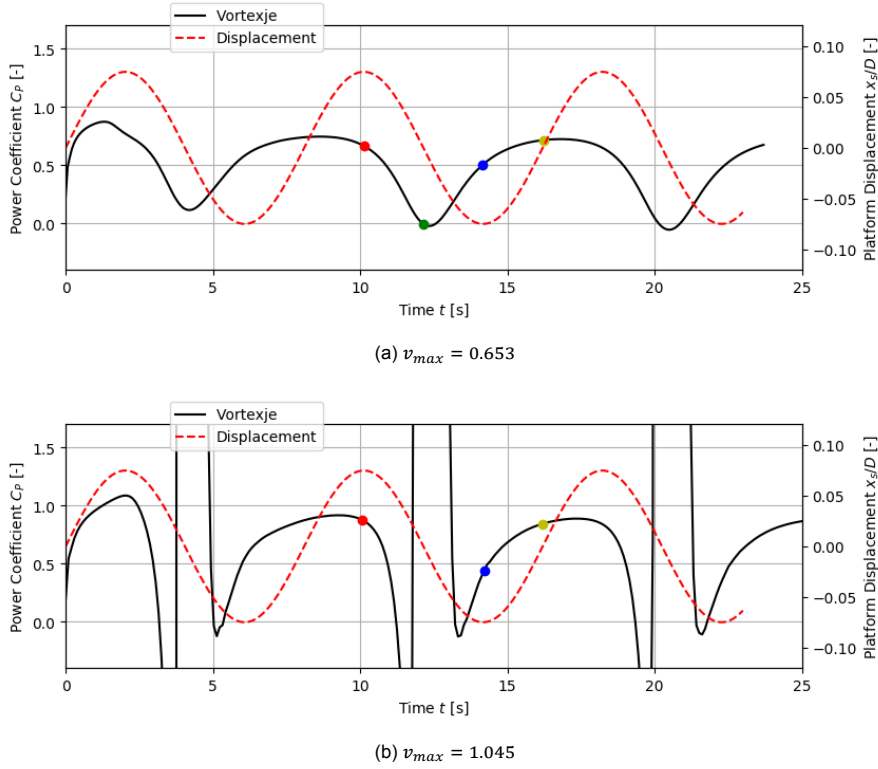


Figure 3.16: Power coefficient for (a) moderate and (b) severe surge conditions

A closer look at the pressure distribution at  $r/R = 0.3, 0.5, \& 0.9$  (Figure 3.17 to Figure 3.19) confirms that instead of a numerical abnormality at any one location along the chord of the airfoil (e.g. leading edge), the issue exists all along the chord of the airfoil. This implies that the error is likely due to the pressure coefficient calculation, which is given through Equation 3.1.

$$C_p := \frac{p - p_{ref}}{\frac{1}{2}\rho v_{ref}^2} = 1 - \frac{Q^2}{v_{ref}^2} - \frac{2}{v_{ref}^2} \frac{\partial \phi}{\partial t} \quad (3.1)$$

This would be due to an incorrect calculation of the two parameters responsible for calculating the pressure coefficient:  $Q$  and  $\frac{\partial \phi}{\partial t}$ . The latter, in the cases run, was consistently shown to be orders of magnitude smaller than the former, implying that at least the tangential surface velocity is calculated improperly. The tangential surface velocity is calculated through the spatial gradient of the doublet strength of the body panels. In Vortexje, a linear model is fitted to the doublet strengths of a given panel and its immediate neighbors to solve for this, and a deeper investigation into its mechanics is the best way to find the source of the errors.

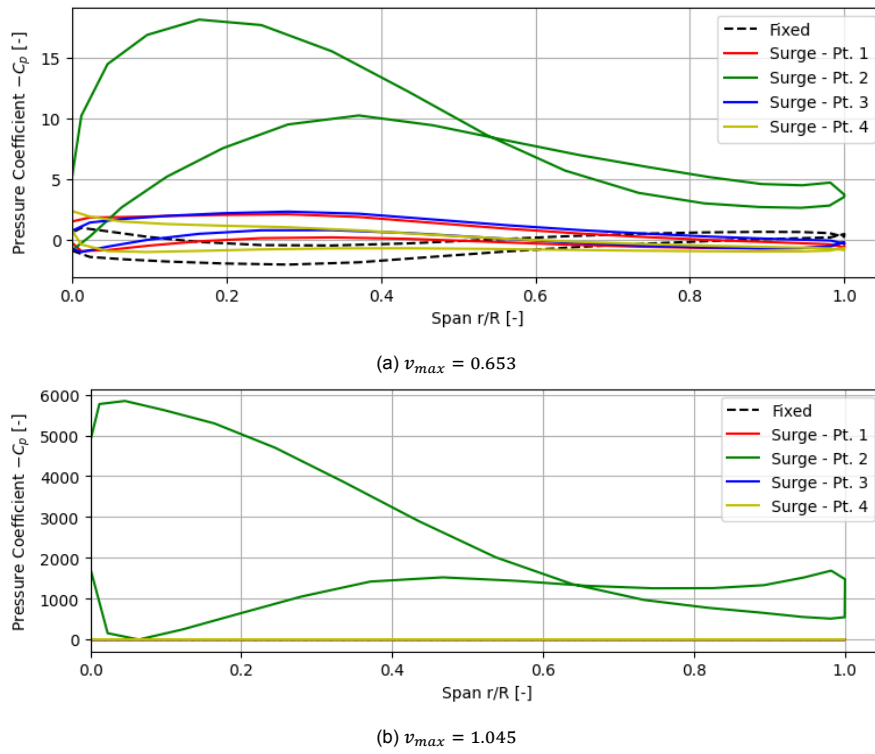


Figure 3.17: Pressure coefficient at  $r/R = 0.3$  for (a) moderate and (b) severe surge conditions

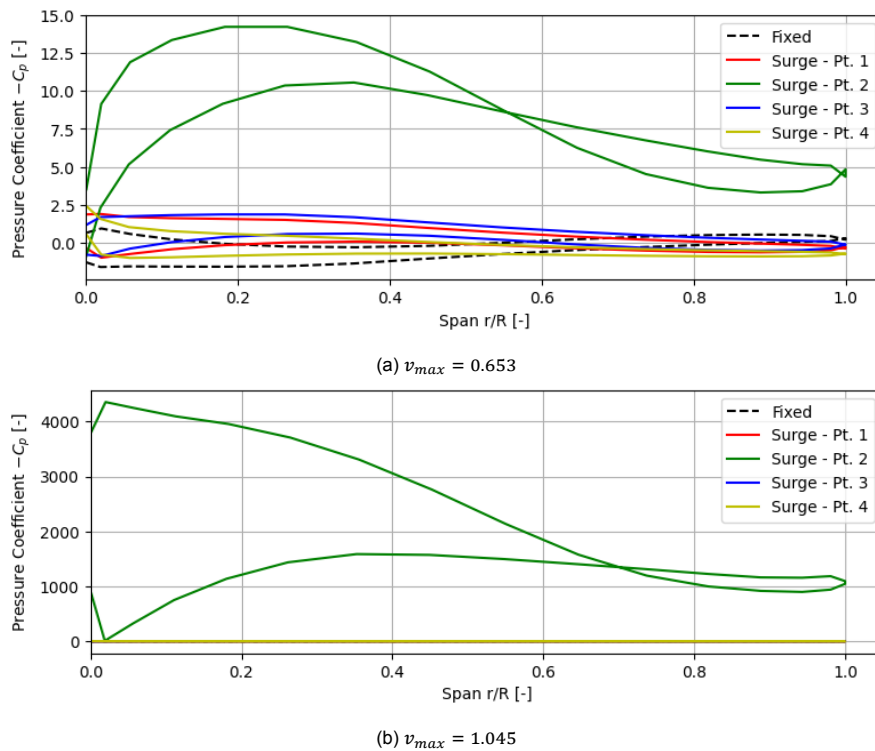


Figure 3.18: Pressure coefficient at  $r/R = 0.5$  for (a) moderate and (b) severe surge conditions

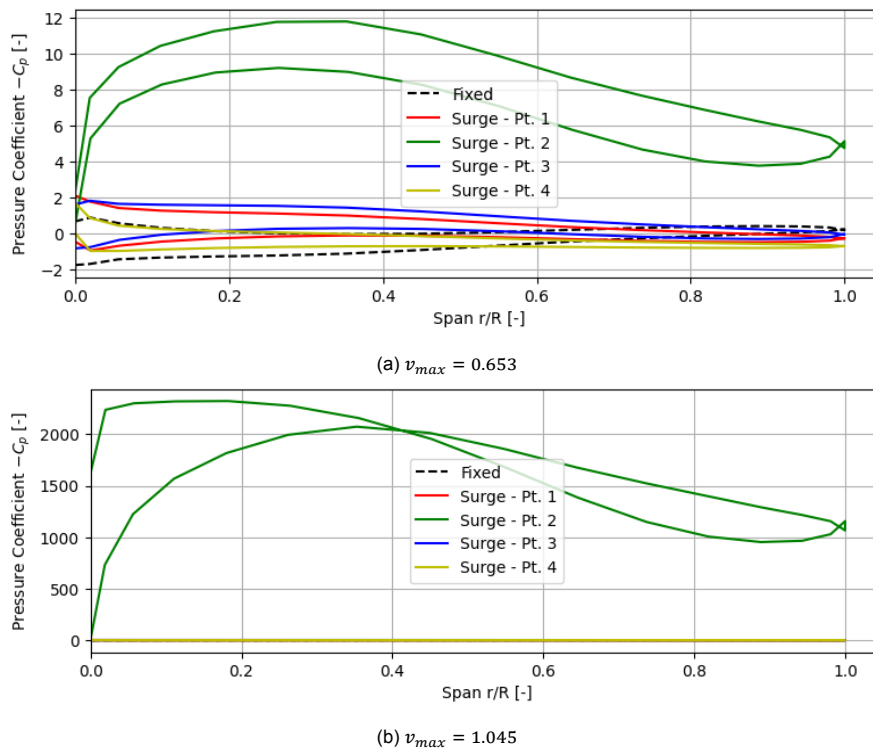
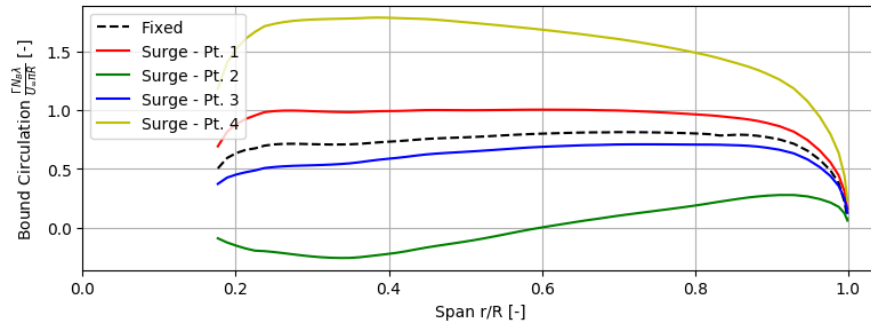


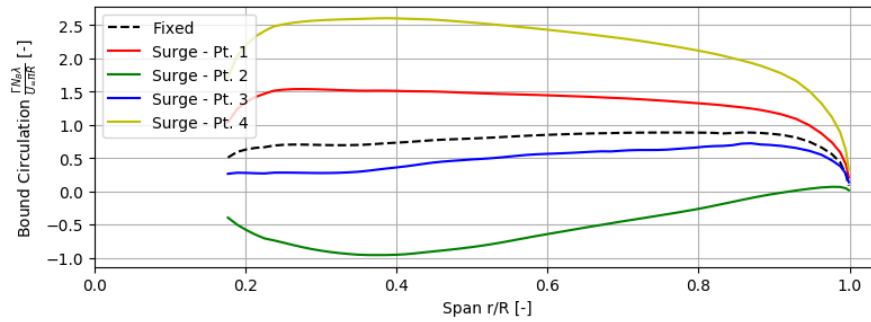
Figure 3.19: Pressure coefficient at  $r/R = 0.9$  for (a) moderate and (b) severe surge conditions

### Circulation Distributions

To better understand the underlying problem that led to numerical instabilities when directly integrating panel method pressure coefficients, the circulation distribution over the surge cycle was produced and analyzed. Figure 3.20 shows the circulation distribution of the moderate and severe surge cases. In both cases, the numerical instabilities are no longer present, and the values seem to be bounded within a reasonable range. To confirm that the expected sinusoidal behaviour exists for circulation, its value at  $r/R = 0.8$  is displayed in Figure 3.21.



(a)  $v_{max} = 0.653$



(b)  $v_{max} = 1.045$

Figure 3.20: Circulation distribution for (a) moderate and (b) severe surge conditions

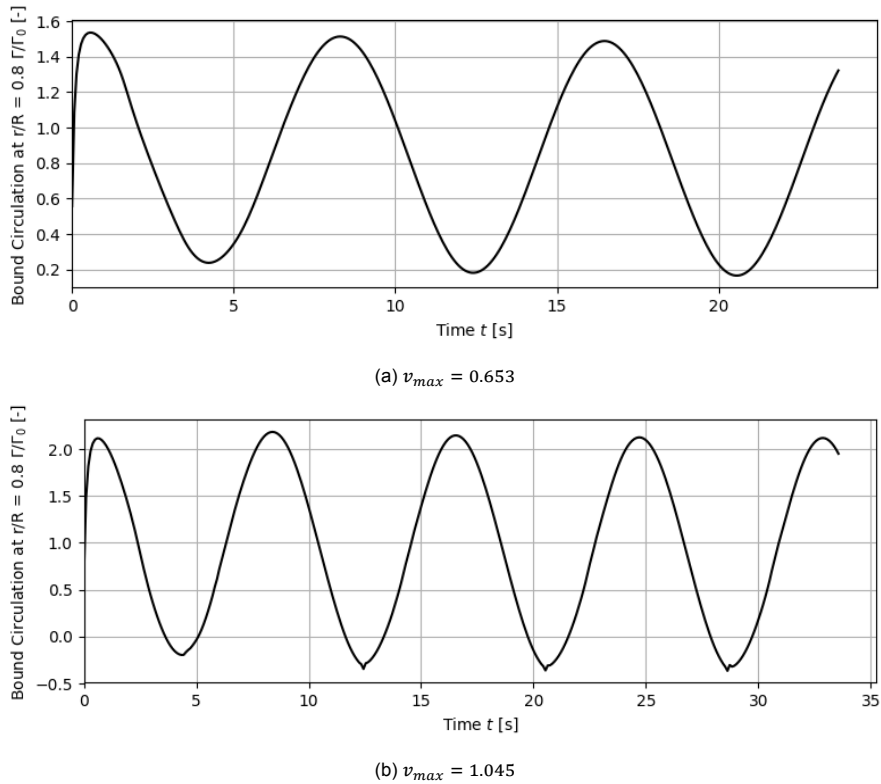


Figure 3.21: Circulation distribution for (a) moderate and (b) severe surge conditions, at  $r/R = 0.8$

The thrust coefficient was estimated through the bound circulation as  $F'_{axial} = L' \cos \phi + D' \sin \phi \approx L' \cos \phi \approx \rho \sqrt{(U_\infty)^2 + (\Omega r)^2} \Gamma \cos \phi$ . The approximation of  $U_{ref} \approx \sqrt{(U_\infty)^2 + (\Omega r)^2}$ , similarly with the UNAFLOW case, led to low errors. The approximation of  $F'_{axial} \approx L' \cos \phi$  neglects a drag term which would otherwise increase the axial force. This would result in an underestimated thrust coefficient, although the amount would depend on the inflow angle. The inflow angle was calculated using the 3-pt method suggested by Rahimi et al. [37], which is described in further detail in chapter 2. A detailed look at the inflow angle, along with other velocity-related parameters, will be shown in the next section.

The value of non-dimensional  $L'$ , shown in Figure 3.22, exhibits the behaviour expected in surge motion - that when the rotor moves downwind, the entire blade should experience a lower angle of attack and thus lower sectional forces.

Overall, the thrust coefficient is far better-bounded than when predicted by integrating panel pressure coefficients. The sinusoidal behaviour of thrust is reproduced, with reasonable comparison. Several effects can be noticed from both Figure 3.23a and Figure 3.23b. First, there exists a phase delay between the CFD results and the numerical results. This may be a result of the implementation of the surge motion in the code, although this needs to be further investigated. Another difference is at  $t \approx 16s$ , when the rotor is moving upwind. The lower thrust is due to highly unsteady flow separation at the airfoil, which is a viscous boundary layer effect not reproducible by Vortexje. However, upon reattachment as the rotor approaches its upwind maximum, the results again resemble those predicted by Vortexje. The third difference is in the magnitude of the thrust. The minimum is lower than that predicted by CFD, and the maximum is likewise higher. This can be also explained by the viscosity of the CFD model, which can act to dampen the oscillations in thrust, leading to the results shown.

There are a number of potential explanations for the discrepancy between thrust coefficient estimation methods. In contrast to the method in which the panel pressure coefficients are integrated, using the bound circulation requires the use of trailing edge wake panel doublet strengths, which ultimately stem from the difference in upper and lower trailing edge blade surface panels. This means that the gradient is not required to calculate it. The pressure coefficient, however, requires the gradient in space of the doublet strengths to be calculated, to then determine the tangential surface velocity. If an error at this stage of the calculation was made, especially away from the trailing edge, that would then lead

to errors in the pressure calculation and overall force distribution.

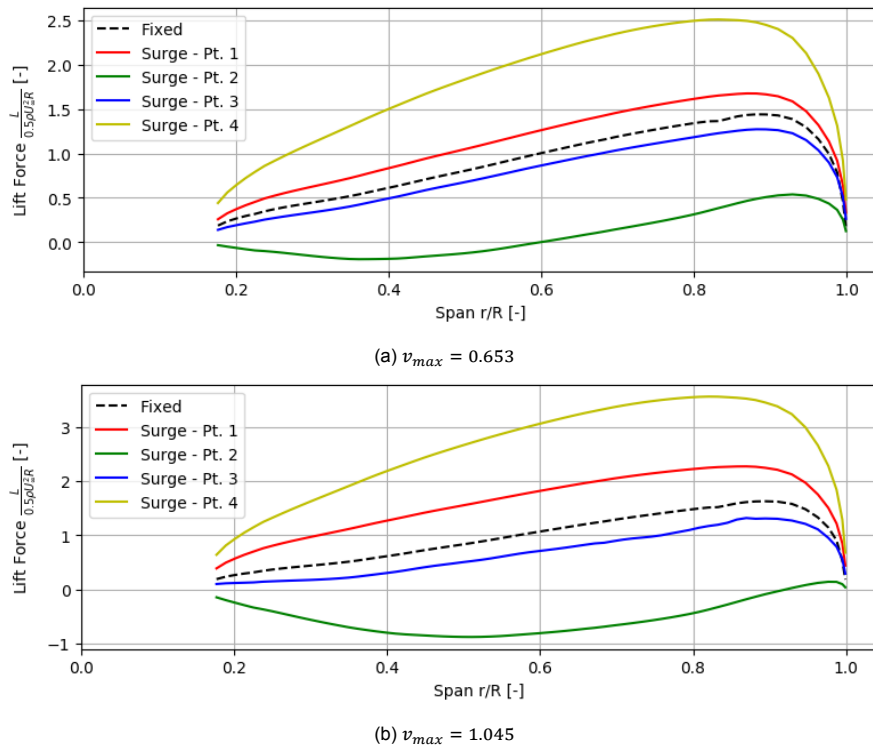


Figure 3.22: Lift distribution for (a) moderate and (b) severe surge conditions

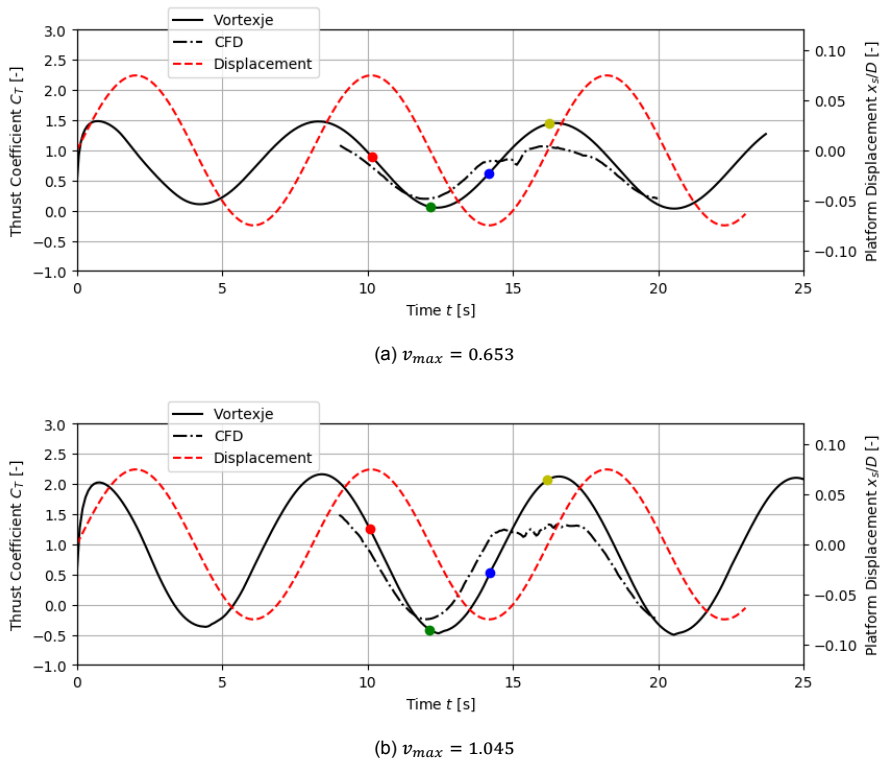


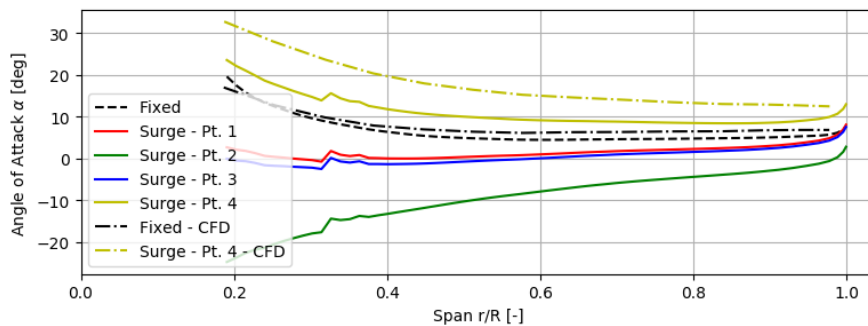
Figure 3.23: Thrust coefficient distribution for (a) moderate and (b) severe surge conditions, assuming  $F'_{axial} \approx L' \cos \phi$

### Angle of Attack Distributions

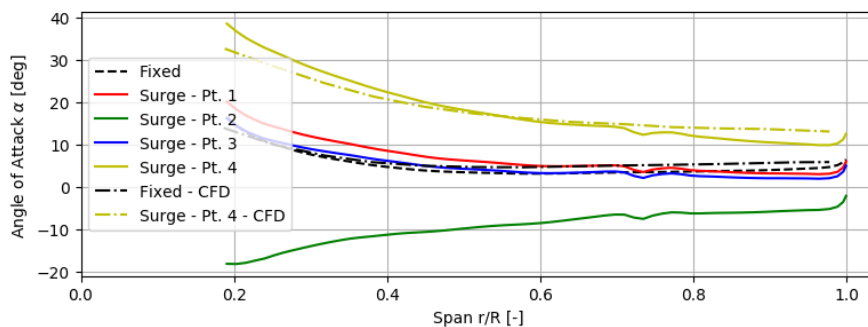
To test the ability of Vortexje in predicting the angle of attack, and thereby the inflow angle, the 3-point method was used. Figure 3.24 and Figure 3.25 show the angle of attack and inflow angle, respectively, for the moderate and severe surge cases. In both cases, the trend along the surge cycle is consistent with expectations; the inflow angle is much higher as the rotor moves upwind, whereas the angle reaches negative values as the rotor moves downwind. For both moderate and severe surge, the angle of attack trend is replicated in both the fixed-base scenario and the surge scenario as the rotor moves downwind (pt. 2). The fixed-base results show a slight underestimation in the angle of attack, compared to CFD results. This could be due to viscous effects that Vortexje can't replicate. However, the agreement in angle of attack, at the moment the rotor moves upwind at maximum velocity, varies significantly between the moderate and severe surge cases. The inconsistency in agreement between moderate and severe surge may be a result of the method in which the angle of attack is calculated. This may also explain the inconsistency between the fixed-base angle of attack and the angle of attack at the maximum upwind and downwind positions, which are expected to be similar. However, the method does predict, for each case, that the angle of attack at the maximum upwind and downwind positions are consistent within themselves, even if they aren't always consistent with the fixed-base prediction.

The reason for this discrepancy may be the method used to predict the angle of attack. The inverse BEM method was not chosen due to its requirement of axial and tangential force distributions - which were shown to be predicted poorly through integrating the panel pressure coefficients. The estimation through bound circulation could also have been chosen, but that estimation in itself requires the use of the inflow angle, thus leading to a circular calculation. The AAT method was not chosen due to its high computational time, and thus the 3-pt. method was chosen due to its lower computational time.

Another reason for the discrepancy may be the calculation method Vortexje uses in calculating the panel source and doublet strengths, which are used directly in calculating the potential velocity away from the surface. If there were inaccuracies in the doublet and source strengths, given surge motion, that would reflect on the angles shown.



(a)  $v_{max} = 0.653$



(b)  $v_{max} = 1.045$

Figure 3.24: Angle of attack distribution for (a) moderate and (b) severe surge conditions

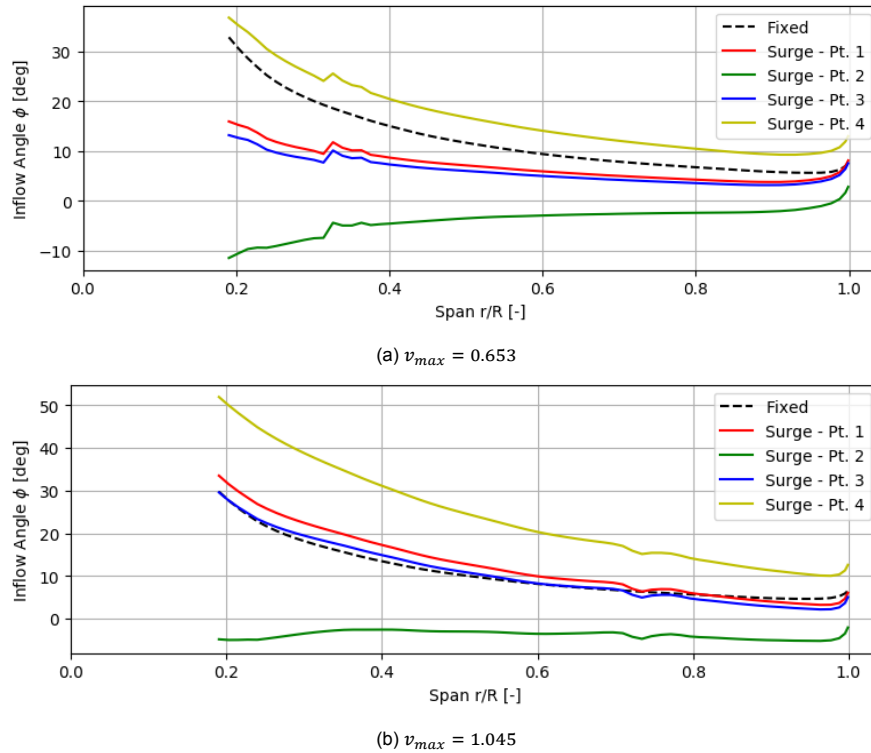


Figure 3.25: Inflow angle distribution for (a) moderate and (b) severe surge conditions

### Induction Factor Distribution

Figure 3.26 shows the predicted axial induction factor distribution for moderate and severe surge cases. While the induction factor could be calculated using the incoming velocity as a reference, it was instead chosen to use the free-stream velocity:

$$a = 1 - \frac{V_{axial}}{U_{\infty}} \quad (3.2)$$

Similar to the inflow angle and angle of attack distributions, the trends are different between moderate and severe surge, with the former having low differences between the phases of surge, and a high difference to the fixed-base case, and the latter having the opposite - higher differences between the surge phase and lower differences. It can be seen in Figure 3.25a that the predicted inflow angle of the fixed-base scenario is double that of the surge scenario at the maximum upstream and downstream positions (Pt. 1 & 3, respectively), even though they are expected to be the same. Given the same free-stream velocity, this explains the difference of the induction factor in Figure 3.26a being double that of the fixed-base turbine. In contrast, the inflow angles for the severe surge case are more consistent with their fixed-base counterpart, leading to values in the same general vicinity.

Over the surge cycle, however, the change in induction factor over the surge can be seen to be modest ( $\sim 0.05$ ) for the case of moderate surge, with a higher change ( $\sim 0.15$ ) for severe surge. This trend is consistent with what is expected for increasing surge severity, although the changes are quite low. Even if assuming the magnitude to be flawed, the magnitude of the change over the surge cycle shown with this method shows that the large changes in induction factor necessary for Vortex Ring State (VRS) are unlikely. To fully investigate the accuracy of this method in calculating these parameters, a comparison with a different method would need to be made.

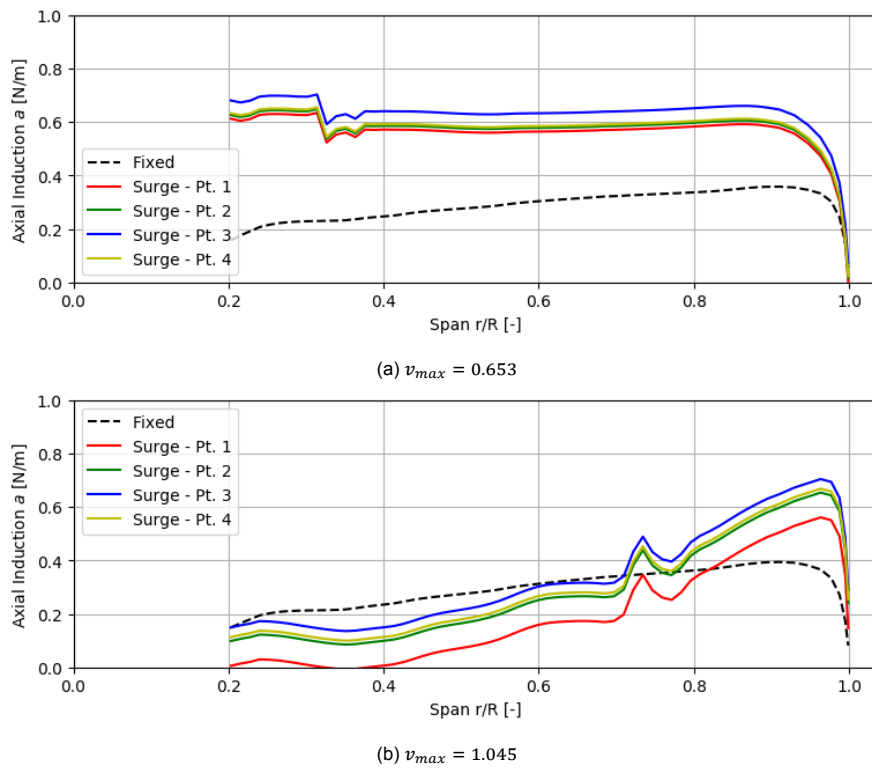
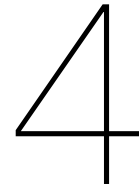


Figure 3.26: Induction factor distribution for (a) moderate and (b) severe surge conditions





# Conclusions and Recommendations

## 4.1. Conclusions

In this study, the application of Vortexje, an open-source inviscid 3D panel method, to floating offshore wind turbine (FOWT) surge motion was investigated. The study began with a validation of the code for a fixed-base rotor using experimental, CFD, and panel method results from the MEXICO test campaign. It was revealed that for low tip-speed ratios, results were within experimental error at 25% and 35% of the blade. Results at 60%, 82% and 92% were within experimental error on the pressure side, but slightly overestimated on the suction side. Results showed a good match with results from CFD and a different inviscid panel method. Similarly, with the design tip speed ratio, suction side results were over-predicted but overall consistent with other numerical results. For the high tip-speed ratio case, suction-side results varied between methods, at all blade locations, with experimental and CFD results predicting viscous boundary-layer separation while the inviscid panel methods were unable to.

Afterwards, a study on the implementation of surge was conducted to test the ability of Vortexje to model translating surfaces. A NACA0012 profile surface with an aspect ratio of 4.5 and angle of attack of 10 degrees was subjected to two types of surge: one that translated the surface directly through space, and one that changed the inflow conditions corresponding with the experienced velocity of the surface. Each test was run with both horizontal and vertical surging motion, for a total of 4 test cases. The vertical surge cases, which more closely resembles the motion of a rotor blade under surge, showed similar wake behaviour and slightly higher circulation oscillations under direct displacement. The horizontal surge case produced abnormalities in the wake when directly translated, especially as the surface experienced its upstream and downstream maximum positions. It was concluded to be a result of the trailing edge wake panel placement method, which projects the experienced velocity vector onto the bisector of the trailing edge. As the surface switched direction, the experienced kinematic velocity resulted in severe and non-physical oscillations of the wake, which weren't present in the changing inflow test case. For following tests with a full FOWT rotor under surge motion, the surfaces were held steady axially while inflow conditions changed to replicate the effect of that surge.

To test the effect of low-severity surge, the UNAFLOW blade was built and modelled with a variety of surge conditions, replicating an earlier study. The thrust mean and oscillation were calculated and compared with experimental, BEM, and lifting-line results. Two methods were chosen to estimate the thrust mean and oscillation: a total integration of the panel pressure coefficients, and an integration of the lift estimated through the bound circulation. Integrating the panel pressure coefficients resulted in expected mean thrust values, compared to other results and previous literature, but lower than expected amplitudes by close to 50%. For the one high-severity surge motion case, the panel drastically both under-predicted the mean, and over-predicted the amplitude of the thrust. The latter method, despite being simply an estimation of the thrust by approximating the axial force as the lift, was much more stable in the investigated surge domain. The results were both more consistent and more accurate, suggesting that at present, it's a more reliable method to calculate the thrust of a rotor.

To test the effect of high-severity surge, two test cases were run, one so-called 'moderate case' with the maximum surge velocity reaching ~ 65% of the inflow velocity, and one 'severe case' with the maximum surge velocity reaching ~ 104% of the inflow velocity. The axial force distributions showed

that for these high surge cases, numerical instabilities presented themselves at the moments of maximum upwind and downwind surge velocities. Contrary to the expectation that downwind motion should lead to lower-than-expected angles of attack and ultimately lower axial forces, the outboard part of the blade predicted higher forces than at the moment of zero rotor velocity. Conversely, the force along the blade was under-predicted at the moment the rotor moved upwind at maximum velocity, even though this stage should have had the highest forces. This inaccuracy led to the overall thrust coefficient oscillating unsteadily; the expected sinusoidal variation failed to appear. For the case of severe surge, the thrust coefficient dropped to large negative values, indicating a lack of numerical stability.

The corresponding tangential force distributions were similarly unsteady, with observed numerical instabilities presenting as an irregular distribution. This suggested that the errors, both axially and tangentially, may have been caused by an inaccurate pressure coefficient calculation, which in turn may have been influenced by an incorrect surface velocity calculation method. The resulting power coefficient experienced similar numerical instabilities.

The estimation of thrust through bound circulation, which was shown earlier to be more stable, was then explored as an option. In an attempt to improve the accuracy of the estimation, the inflow angle was calculated using the 3-pt. method an interpolation method, in which the velocity was sampled at several points above and below the chord line of a given airfoil section. The axial force was then estimated as the component of lift in the axial direction, through that inflow angle, and the axial force estimation was integrated over the blade to predict the overall thrust coefficient, which was then compared with CFD results. The results neglected the effect of drag, which would lower the predictions. A sinusoidal trend was then found, comparable to the viscous CFD results, with several differences. There was a slight phase difference between the results, which may be due to the implementation of the surge, although a proper investigation of that was not conducted in this study. The amplitude of the oscillations was higher (and would be higher still if drag were included) than the CFD, which can be attributed to the fact that viscosity acts to damp these oscillations, something that would be reflected in the CFD results, but not in the inviscid panel method results. The CFD results also predicted a drop in thrust coefficient at the moment the rotor moves upwind with maximum velocity. This was explained by the author as the result of highly unsteady flow leading to boundary layer separation, which is another viscous effect that can't be, and wasn't, captured by Vortexje. The stability that this method of calculating thrust provided, in contrast with the panel pressure coefficient integration, was hypothesized to be a result of the surface velocity calculation method for blade surface panels. The calculation of pressure coefficient requires the gradient of the calculated panel surface tangential velocity, meaning an improper implementation of surge in this calculation may be the reason for the inaccuracy. The exact reason was not investigated in this study, however.

The angles of attack and inflow angles were also estimated using the 3-pt. method, with the distributions plotted over the major points of the surge cycle. The overall trend of low (and in this case, negative) inflow angles at the moment of downwind motion, and high inflow angles at the moment of upwind motion, was replicated with this method. The angles at the maximum upwind and downwind positions were very close, which is expected as the experienced velocity was the same for both. The angle of attack for the fixed-base case was shown to be a reasonable match, although under-predicted by several degrees over the entire span, compared with CFD results. However, the angle of attack at the moment of maximum upwind motion was not consistently well-predicted, with results for moderate surge under-predicted over the entire blade, and results for severe surge partially over-predicted and partially under-predicted. Results were also inconsistent with how well angles at the maximum upstream and downstream positions matched those of the fixed-base case. While expected to be similar, the level of similarity was much higher for the severe case than for the moderate case. The inconsistency in these results was hypothesized to be the result of potential inaccuracies in the source and doublet strengths, or an inaccuracy in using the 3-pt. method, although a comparison with other methods needs to be conducted to properly evaluate that.

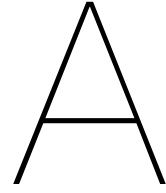
The induction factor distribution was estimated from the same results as the calculated angles, with high values predicted for the moderate surge case and lower values predicted for the severe surge case. The accuracies of the magnitudes are questionable, and need to be compared with CFD results, but the change in induction factor over time suggested low amplitude values ( $\sim 0.05$  and  $\sim 0.15$  for the moderate and severe surge cases, respectively). This suggested that the change in induction factor was not severe enough to cause Vortex Ring State, which is characterized by induction factor values of  $a \geq 1$ .

## 4.2. Recommendations

The following are recommendations for further investigation:

- It was found that when integrating the panel pressure coefficients, the forces were under-predicted for low surge and numerically unstable for higher surge. This should be investigated in more detail to determine if this is an error in the code, and if so, how to correct it. This would allow for a better estimation of thrust coefficient that takes inviscid drag into account, which the bound circulation method does not. This would also provide an estimation of the rotor power coefficient.
- Vortexje currently has a placeholder class that allows for the implementation of a boundary layer. If a boundary layer were tested and implemented, this would allow for an estimation of viscous forces that would improve its accuracy both for fixed-base and surging rotors.
- The 3-pt. method was chosen to calculate inflow angles and induction factors over the blade because the inverse BEM and AAT methods were inaccurate and computationally expensive, respectively. A further look into its accuracy, or an investigation into other methods should be done to improve angle predictions under surge motion.
- At the moment, for moderate and high-severity surge motion, CFD results only exist for the overall thrust, and the span-wise angle of attack at the moment of maximum upwind velocity. Further tests could produce more detailed results, such as the inflow angle at other points of the surge cycle, as well as the induction factor, axial/tangential loading distributions, and the power coefficient over the cycle. This would allow for a more detailed comparison, and the ability to identify the shortcomings of Vortexje as it exists presently.





# Appendix

## A.1. MEXICO Test Campaign

### A.1.1. Background to the MEXICO Test Campaign

The 'Model Experiments in Controlled Conditions', or MEXICO, test campaign was originally run in 2006 as a European Union FP5 project. Prior to this campaign, model validation was mostly conducted with global wind turbine parameters (e.g. power, thrust, root bending moment). However, in the late 80s and 90s, it became clear that detailed span-wise data was necessary to improve model validation, and so the MEXICO test campaign was led by ECN to provide a source of high quality experimental data, with which improved validation of wind turbine simulation tools could be conducted. The results of the MEXICO campaign were analyzed in IEA Wind Task Mexnext-I, and yielded discrepancies between experimental and simulated data for blade loads and induced velocities. To resolve these discrepancies, a 'New MEXICO' campaign was conducted in Mexnext-II, with a corresponding analysis in Mexnext-III [CITE]. This latest analysis featured a more thorough comparison between experimental and simulated data, with a wide range of BEM, Lifting-Line, and CFD models.

### A.1.2. MEXICO Rotor and Experiment Details

The MEXICO rotor is a 4.5m diameter, three-bladed rotor with a 0.42m diameter hub. Table A.1 shows the composition of airfoils used in the design of the blade.

Span Location $r/R[-]$	Profile
0.20 – 0.46	DU91-W2-250
0.54 – 0.66	RISØ A1-21
0.74 – 1.00	NACA 64418

Table A.1: Airfoil sections at various span-wise locations on the MEXICO rotor

This rotor was tested in the Large Scale Low Speed (LLF) facility at the German Dutch Wind tunnel organization (DNW), using a 9.5×9.5m open jet tunnel. Figure A.1 shows the full rotor ready for experimental testing. The rotor was run with three sets of operating conditions: below, above, and at design conditions. Details of the operating conditions can be found in Table A.2. All tests were run with a rotational speed of 424 RPM and blade pitch of -2.3 deg, in air with a density of  $\rho = 1.2 \text{ kg/m}^3$ .



Figure A.1: The MEXICO rotor set up for experimental testing. Taken from [40].

Test	Free-stream Velocity $U_\infty$ [m/s]	Tip Speed Ratio $\lambda$ [-]
1	10.0	10.0
2 (Design Conditions)	14.7	6.7
3	24.1	4.2

Table A.2: MEXICO Test Conditions

Sectional pressure measurements were taken with 25-28 Kulite® sensors at each of 25, 35, 60, 82, and 92% of the span (measured from the hub center). These spanwise locations are illustrated in Figure A.2 .

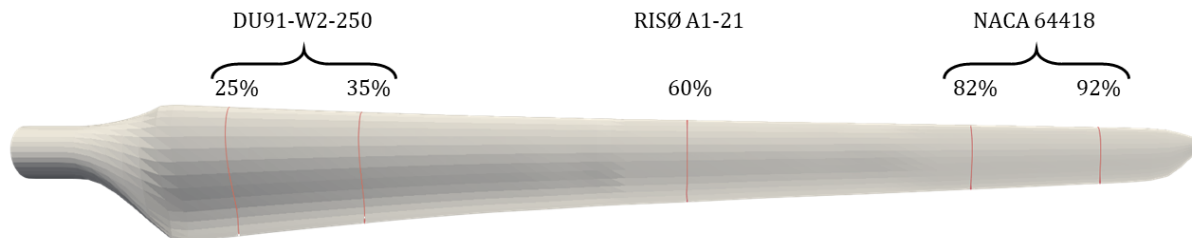


Figure A.2: The MEXICO blade showing locations at which sectional pressure measurements were taken.

## A.2. UNAFLOW Campaign

### A.2.1. Background to the UNAFLOW test campaign

The 'UNsteady Aerodynamics for FLoating Wind', or UNAFLOW project, is a joint EU-IRPWIND experiment that sought to understand the unsteady aerodynamics of FOWT systems using a holistic approach. Similar to the MEXICO campaign, it seeks to act as a benchmark for numerical model validation. It is comprised of a 2D sectional study and a full 3D rotor study upon which harmonic changes in angle of attack and surge displacement, respectively, are imposed.

### A.2.2. UNAFLOW Rotor and Experiment Details

The UNAFLOW turbine is a 2.38m diameter, three-bladed rotor, and was designed by scaling down the DTU10MW RWT [2] by a factor of 75, matching the thrust and power coefficients while changing the

chord, twist, and airfoil distributions. A low-Reynolds SD70322 airfoil was used to create the blade as the Reynold number used in the wind tunnel was 225 times smaller than that of the full-scale turbine. The experiments were run in a 13.84m wide  $\times$  3.84m high section of the PoliMi wind tunnel. The tests that will be compared in this study were run with an inflow velocity of 4 m/s and rotational speed of 241 RPM ( $\lambda = 7$ ). The blade pitch angle was 0 degrees for all tests. The surge amplitudes and frequencies tested were translated from real-life scenarios, and are shown in Table 2.2 . A more detailed description of the set-up can be found in Bayati [3].

### A.2.3. Numerical Models used in Simulating UNAFLOW Experiments

To compare against numerical results, these tests were replicated with Aero-Module, an in-house TNO software. Aero-Module is comprised of a BEM method and an FVM lifting-line model, the latter of which is named Aerodynamic Wind turbine Simulation Model (AWSM). Both of these models provide viscous solutions, by nature of the aerodynamic polars which they extract load data from. Thus, detached boundary layer effects and dynamic stall effects which occur at high inflow angles were able to be modelled accurately. In contrast, the inviscid nature of Vortexje precludes the possibility of modelling these effects, meaning rotor load results will differ. However, the purpose of this part of the study is not to validate Vortexje against these results, but rather to compare its ability to capture the effects of varying surge motion against that of real life.

Further numerical results were calculated by means of a block-structured Unsteady RANS (URANS) CFD solver named FLOWer, which was developed by the German Aerospace Center (DLR), with wind turbine modifications developed by the University of Stuttgart [23][56][42].

## A.3. NREL 5MW Rotor

The afore-mentioned characterization of unsteady FOWT aerodynamics by Sebastian and Lackner [45] was conducted on the NREL 5MW reference turbine, an often-used benchmark for which experimental data is readily available. The high-level details are given in Table A.3, and the blade profile is summarized in Table A.4. Full details of the blade profiles can be found in [18]. This wind turbine will be commonly referred to in the upcoming discussion on FOWT-modelling literature.

Property	Value
Rating	5 MW
Rotor orientation, configuration	Upwind, 3 blades
Control	Variable speed, collective pitch
Rotor, hub diameter	126 m, 3 m
Hub height	90 m
Cut-in, rated, cut-out wind speed	3 m/s, 11.4 m/s, 25 m/s
Cut-in, rated rotor speed	6.9 rpm, 12.1 rpm
Rated tip speed	80 m/s
Overhang, shaft tilt, precone	5 m, 5°, 2.5°
Rotor mass	110,000 kg
Nacelle mass	240,000 kg
Tower mass	347,460 kg

Table A.3: NREL 5MW baseline turbine properties

Radial Location [m]	Twist [deg]	Chord [m]	Airfoil Profile
2.8667	13.308	3.542	Cylinder
5.6000	13.308	3.854	Cylinder
8.3333	13.308	4.167	Transitional Cylinder
11.7500	13.308	4.557	DU W-405
15.8500	11.480	4.652	DU W-350
19.9500	10.162	4.458	DU W-350
24.0500	9.011	4.249	DU 97-W-300
28.1500	7.795	4.007	DU 91-W2-250
32.2500	6.544	3.748	DU 91-W2-250
36.3500	5.361	3.502	DU 91-W-210
40.4500	4.188	3.256	DU 91-W-210
44.5500	3.125	3.010	NACA 64-618
48.6500	2.319	2.764	NACA 64-618
52.7500	1.526	2.518	NACA 64-618
56.1667	0.863	2.313	NACA 64-618
58.9000	0.370	2.086	NACA 64-618
61.6333	0.106	1.419	NACA 64-618

Table A.4: NREL 5MW baseline turbine blade aerodynamic properties

# Bibliography

- [1] Jorn H Baayen. Vortexje-an open-source panel method for co-simulation. *arXiv preprint arXiv:1210.6956*, 2012.
- [2] Christian Bak, Frederik Zahle, Robert Bitsche, Taeseong Kim, Anders Yde, Lars Christian Henriksen, Morten Hartvig Hansen, Jose Pedro Albergaria Amaral Blasques, Mac Gaunaa, and Anand Natarajan. The dtu 10-mw reference wind turbine. In *Danish Wind Power Research 2013*, 2013.
- [3] Ilmas Bayati, Marco Belloli, Luca Bernini, Davide Maria Boldrin, Koen Boorsma, Marco Caboni, Marion Cormier, Robert Mikkelsen, Thorsten Lutz, and Alberto Zasso. UnafLOW project: Unsteady aerodynamics of floating wind turbines. In *Journal of Physics: Conference Series*, volume 1037, page 072037. IOP Publishing, 2018.
- [4] Emmanuel Branlard, Kristian Dixon, and Mac Gaunaa. Vortex methods to answer the need for improved understanding and modelling of tip-loss factors. *IET Renewable Power Generation*, 7(4):311–320, 2013.
- [5] Tony Burton, Nick Jenkins, David Sharpe, and Ervin Bossanyi. *Wind energy handbook*. John Wiley & Sons, 2011.
- [6] Ziwen Chen, Xiaodong Wang, Yize Guo, and Shun Kang. Numerical analysis of unsteady aerodynamic performance of floating offshore wind turbine under platform surge and pitch motions. *Renewable Energy*, 163:1849–1870, 2021.
- [7] Jacobus B De Vaal, Martin Hansen, and Torgeir Moan. Effect of wind turbine surge motion on rotor thrust and induced velocity. *Wind Energy*, 17(1):105–121, 2014.
- [8] Vanessa Del Campo, Daniele Ragni, Daniel Micallef, Busra Akay, Francisco Javier Diez, and C Simão Ferreira. 3d load estimation on a horizontal axis wind turbine using spiv. *Wind Energy*, 17(11):1645–1657, 2014.
- [9] Vanessa del Campo, Daniele Ragni, Daniel Micallef, Francisco Javier Diez, and CJ Simão Ferreira. Estimation of loads on a horizontal axis wind turbine operating in yawed flow conditions. *Wind Energy*, 18(11):1875–1891, 2015.
- [10] Kristian Dixon. The near wake structure of a vertical axis wind turbine: Including the development of a 3d unsteady free-wake panel method for vawts. Master’s thesis, Delft University of Technology, 2008.
- [11] Russell Farrugia, Tonio Sant, and Daniel Micallef. Investigating the aerodynamic performance of a model offshore floating wind turbine. *Renewable Energy*, 70:24–30, 2014.
- [12] Russell Farrugia, Tonio Sant, and Daniel Micallef. A study on the aerodynamics of a floating wind turbine rotor. *Renewable energy*, 86:770–784, 2016.
- [13] Carlos Ferreira, Wei Yu, Arianna Sala, and Axelle Vire. Dynamic inflow model for a floating horizontal axis wind turbine in surge motion. *Wind Energy Science Discussions*, pages 1–22, 2021.
- [14] Sandeep Gupta and J Gordon Leishman. Dynamic stall modelling of the s809 aerofoil and comparison with experiments. *Wind Energy: An International Journal for Progress and Applications in Wind Power Conversion Technology*, 9(6):521–547, 2006.
- [15] Martin Hansen. *Aerodynamics of wind turbines*. Routledge, 2015.
- [16] John L Hess and Apollo MO Smith. Calculation of potential flow about arbitrary bodies. *Progress in Aerospace Sciences*, 8:1–138, 1967.

- [17] Minu Jeon, Seungmin Lee, and Soogab Lee. Unsteady aerodynamics of offshore floating wind turbines in platform pitching motion using vortex lattice method. *Renewable Energy*, 65:207–212, 2014.
- [18] Jason Jonkman. Definition of the floating system for phase iv of oc3. Technical report, National Renewable Energy Lab.(NREL), Golden, CO (United States), 2010.
- [19] Jason Jonkman and Denis Matha. Dynamics of offshore floating wind turbines—analysis of three concepts. *Wind Energy*, 14(4):557–569, 2011.
- [20] Jason Jonkman, T Larsen, A Hansen, T Nygaard, K Maus, M Karimirad, Z Gao, T Moan, and I Fylling. Offshore code comparison collaboration within iea wind task 23: Phase iv results regarding floating wind turbine modeling. Technical report, National Renewable Energy Lab.(NREL), Golden, CO (United States), 2010.
- [21] Joseph Katz and Allen Plotkin. *Low-speed aerodynamics*, volume 13. Cambridge university press, 2001.
- [22] Johan C Kok. Resolving the dependence on freestream values for the k-turbulence model. *AIAA journal*, 38(7):1292–1295, 2000.
- [23] Norbert Kroll and Jens K Fassbender. *MEGAFLOW-Numerical Flow Simulation for Aircraft Design: Results of the Second Phase of the German CFD Initiative MEGAFLOW, Presented During Its Closing Symposium at DLR, Braunschweig, Germany, December 10 and 11, 2002*, volume 89. Springer Science & Business Media, 2005.
- [24] Ryan Kyle, Yeaw Chu Lee, and Wolf-Gerrit Früh. Propeller and vortex ring state for floating offshore wind turbines during surge. *Renewable Energy*, 2020.
- [25] Torben J Larsen and Helge Aagaard Madsen. On the way to reliable aeroelastic load simulation on vawt's. *Proceedings of EWEA*, 2013:9, 2013.
- [26] Gordon J Leishman. *Principles of helicopter aerodynamics with CD extra*. Cambridge university press, 2006.
- [27] J Gordon Leishman. Challenges in modelling the unsteady aerodynamics of wind turbines. *Wind Energy: An International Journal for Progress and Applications in Wind Power Conversion Technology*, 5(2-3):85–132, 2002.
- [28] C Lindenburg. Investigation into rotor blade aerodynamics. *Energy research Centre of the Netherlands (ECN) Wind Energy publication, ECN-C-03-025*, 2003.
- [29] Yuanchuan Liu, Qing Xiao, Atilla Incecik, Christophe Peyrard, and Decheng Wan. Establishing a fully coupled cfd analysis tool for floating offshore wind turbines. *Renewable Energy*, 112:280–301, 2017.
- [30] Yuanchuan Liu, Qing Xiao, Atilla Incecik, and Christophe Peyrard. Aeroelastic analysis of a floating offshore wind turbine in platform-induced surge motion using a fully coupled cfd-mbd method. *Wind Energy*, 22(1):1–20, 2019.
- [31] Daniel Micallef. *3D flows near a HAWT rotor: A dissection of blade and wake contributions*. PhD thesis, Delft University of Technology, 2012.
- [32] Daniel Micallef and Tonio Sant. Loading effects on floating offshore horizontal axis wind turbines in surge motion. *Renewable Energy*, 83:737–748, 2015.
- [33] Ricardo Pereira, Gerard Schepers, and Marilena D Pavel. Validation of the beddoes–leishman dynamic stall model for horizontal axis wind turbines using mexico data. *Wind Energy*, 16(2): 207–219, 2013.
- [34] Dale M Pitt and David A Peters. Theoretical prediction of dynamic-inflow derivatives. 1980.

- [35] Hamid Rahimi, Bastian Dose, Bernhard Stoevesandt, and Joachim Peinke. Investigation of the validity of bem for simulation of wind turbines in complex load cases and comparison with experiment and cfd. 749(1):012015, 2016.
- [36] Hamid Rahimi, M Hartvelt, Joachim Peinke, and Jan Gerhard Schepers. Investigation of the current yaw engineering models for simulation of wind turbines in bem and comparison with cfd and experiment. 753(2):022016, 2016.
- [37] Hamid Rahimi, Gerard Schepers, Wen Zhong Shen, Néstor Ramos García, Marc S Schneider, Daniel Micallef, Carlos Simao Ferreira, Eva Jost, Levin Klein, and Iván Herráez. Evaluation of different methods for determining the angle of attack on wind turbine blades with cfd results under axial inflow conditions. *Renewable Energy*, 125:866–876, 2018.
- [38] Tonio Sant, David Bonnici, Russell Farrugia, and Daniel Micallef. Measurements and modelling of the power performance of a model floating wind turbine under controlled conditions. *Wind Energy*, 18(5):811–834, 2015.
- [39] Jan Gerhard Schepers. Engineering models in wind energy aerodynamics: Development, implementation and analysis using dedicated aerodynamic measurements. 2012.
- [40] Jan Gerhard Schepers and Herman Snel. Model experiments in controlled conditions. *ECN Report: ECN-E-07-042*, 2007.
- [41] Marc S Schneider, Jens Nitzsche, and Holger Hennings. Accurate load prediction by bem with airfoil data from 3d rans simulations. In *Journal of Physics: Conference Series*, volume 753, page 082016. IOP Publishing, 2016.
- [42] Christoph Schulz, Levin Klein, Pascal Weihing, and Thorsten Lutz. Investigations into the interaction of a wind turbine with atmospheric turbulence in complex terrain. In *Journal of Physics: Conference Series*, volume 753, page 032016. IOP Publishing, 2016.
- [43] Thomas Sebastian. The aerodynamics and near wake of an offshore floating horizontal axis wind turbine. 2012.
- [44] Thomas Sebastian and Matthew Lackner. Analysis of the induction and wake evolution of an offshore floating wind turbine. *Energies*, 5(4):968–1000, 2012.
- [45] Thomas Sebastian and Matthew Lackner. Characterization of the unsteady aerodynamics of offshore floating wind turbines. *Wind Energy*, 16(3):339–352, 2013.
- [46] Xin Shen, Jinge Chen, Ping Hu, Xiaocheng Zhu, and Zhaohui Du. Study of the unsteady aerodynamics of floating wind turbines. *Energy*, 145:793–809, 2018.
- [47] Jens Sørensen, Wen Zhong Shen, and Xabier Munduate. Analysis of wake states by a full-field actuator disc model. *Wind Energy: An International Journal for Progress and Applications in Wind Power Conversion Technology*, 1(2):73–88, 1998.
- [48] Theodore Theodorsen. General theory of aerodynamic instability and the mechanism of flutter. 1935.
- [49] CT Tran and D Petot. Semi-empirical model for the dynamic stall of airfoils in view of the application to the calculation of responses of a helicopter blade in forward flight. 1980.
- [50] Thanh Toan Tran and Dong Hyun Kim. The aerodynamic interference effects of a floating offshore wind turbine experiencing platform pitching and yawing motions. *Journal of Mechanical Science and Technology*, 29(2):549–561, 2015.
- [51] Thanh Toan Tran and Dong-Hyun Kim. The platform pitching motion of floating offshore wind turbine: A preliminary unsteady aerodynamic analysis. *Journal of Wind Engineering and Industrial Aerodynamics*, 142:65–81, 2015.
- [52] Thanh Toan Tran and Dong-Hyun Kim. A cfd study into the influence of unsteady aerodynamic interference on wind turbine surge motion. *Renewable Energy*, 90:204–228, 2016.

- [53] Thanh Toan Tran and Dong-Hyun Kim. Fully coupled aero-hydrodynamic analysis of a semi-submersible fowt using a dynamic fluid body interaction approach. *Renewable energy*, 92:244–261, 2016.
- [54] Thanh toan Tran, Donghyun Kim, and Jinseop Song. Computational fluid dynamic analysis of a floating offshore wind turbine experiencing platform pitching motion. *Energies*, 7(8):5011–5026, 2014.
- [55] Arne van Garrel. Multilevel panel method for wind turbine rotor flow simulations. 2016.
- [56] Pascal Weihing, Christoph Schulz, Thorsten Lutz, and Ewald Krämer. Comparison of the actuator line model with fully resolved simulations in complex environmental conditions. In *Journal of Physics: Conference Series*, volume 854, page 012049. IOP Publishing, 2017.
- [57] Binrong Wen, Xinliang Tian, Xingjian Dong, Zhike Peng, and Wenming Zhang. Influences of surge motion on the power and thrust characteristics of an offshore floating wind turbine. *Energy*, 141: 2054–2068, 2017.
- [58] Wei Yu. *The wake of an unsteady actuator disc*. PhD thesis, PhD thesis, Delft University of Technology, Delft, <https://doi.org/10.4233> ..., 2018.